OPTICAL PERFORMANCE OF A SEASONALLY ADAPTIVE ASYMMETRIC COMPOUND PARABOLIC CONCENTRATOR

A THESIS SUBMITTED TO

THE FACULTY OF GRADUATE STUDIES

IN PARTIAL FULFILLMENT OF THE REQUIREMENTS

FOR THE DEGREE OF

MASTER OF APPLIED SCIENCE

GRADUATE PROGRAM IN MECHANICAL ENGINEERING,

YORK UNIVERSITY,

TORONTO, ONTARIO

GIANPAOLO LENARDUZZI

SUPERVISED BY DR. THOMAS COOPER

LASSONDE SCHOOL OF ENGINEERING,

YORK UNIVERSITY

August 2023

Abstract

Stationary concentrators have the capabilities to supply power in residential and commercial applications, where typical required temperatures range between 20° and 400°. To advance the performance and possible applications of these devices, this work presents an innovative asymmetric stationary concentrator, called Seasonally Adaptive ACPC, which maximizes concentration by semi-annual solar pseudo-tracking. The concentrator is described, and its performance is analyzed using theoretical, numerical, and experimental methods. The former includes the adaptation of the source-acceptance map matching method for ACPCs and the theoretical performance of possible designs; and numerical studies used Monte Carlo ray tracing to investigate optical performance parameters. Experimental efforts involved measuring the optical performance of a practically relevant prototype ($\theta_{in,1}$=0°, $\theta_{in,2}$=90°, and a C_g=2×) in Toronto, Canada, using an innovative flux mapping procedure. Through this work, the Seasonally Adaptive ACPC was found to be a low-cost alternative to meet low to medium temperature heating demands at high latitudes.

Dedication

This thesis is dedicated to my beloved wife, Lucia, who has shown me unwavering patience, compassion, and love. I cannot thank her enough for the sacrifices she made throughout this process. Her encouragement and support have been instrumental in making this thesis possible.

I also want to dedicate it to my parents, Ingrid and Stefano and my grandparents Arturo, Nelly, Gianfranco, and Caterina who mean the world to me, even though some of them are no longer among us, their memories and teachings still guide my life to this day.

Acknowledgements

First, I would like to express my deepest gratitude to my supervisor, Prof. Thomas Cooper, for the opportunity to perform my master thesis under his guidance. His unwavering support, vital feedback, and expertise was instrumental in the shaping and completion of this work. His passion and encouragement were a key motivator through my graduate studies.

I'm very thankful to Prof. Roger Kempers, who as part of my supervisory committee, provided valuable suggestions and constructive criticism, which have increased the quality of my research.

I want to express my sincere appreciation to my fellow CooperLab colleagues: Mubariz, Taz, Matteo, Perry, Ana, Ikbal, Rajiv and Niknaz, this achievement wouldn't have been possible without your support, feedback, and motivating discussions. You and the rest of my graduate colleagues made this journey that much more rewarding.

I want to thank the Natural Sciences and Engineering Research Council of Canada (NSERC) and York University for providing the necessary financial support, which made all this possible. I would also like to acknowledge the Mechanical Engineering Department at Lassonde, and those who make it work daily.

On a more personal note, I would like to thank God, for giving me the strength, wisdom, guidance and understanding I needed through this project. I also want to express my deepest and heartfelt gratitude to my family and friends for their constant belief in me, and for encouraging me during the difficult times; your unconditional love has been the force driving me forwards.

Even more so is my gratitude to my parents, Ingrid, and Stefano Lenarduzzi, who have always loved me unconditionally and taught me the value of hard work in achieving my goals. To my dear sister, Cristina I am grateful for your presence in my life as a loving sister. Lastly, I would like to thank my wife and my dog, for they are my reason to push harder every day.

Table of Contents

Table of Figures

Table of Equations

List of Tables

Nomenclature

Latin Characters

A_i	Inlet/entry aperture area	m^2
A_o	Outlet/exit aperture area	m^2
C_f	Flux concentration ratio	×
C_g	Geometric concentration ratio	×
$C_{g,max}$	Maximum geometric concentration ratio	×
$C_{g,stationary}$	Fundamental limit of concentration for stationary concentrators	×
$C_{ideal,2D}$	Ideal (maximum) concentration ratio	×
D	Diagonal of an ACPC, which defines the acceptance angle	m
eT	Exposure time	s
f	Focal length	m
F	Acceptance function	-
gV	Grey value of pixels	Digital Numbers (DN)
H	Irradiance	W/m^2
H_b	Beam irradiance	W/m^2
H_d	Diffuse horizontal irradiance	W/m^2
H_G	Global horizontal irradiance	W/m^2
H_i	Radiative flux incident on inlet aperture	W/m^2
H_N	Direct normal irradiance	W/m^2
H_r	Reflected irradiance	W/m^2
H_o	Radiative flux incident on outlet aperture	W/m^2
H_β	Global horizontal irradiance on a tilted surface	W/m^2
$H_{d\beta}$	Diffuse horizontal irradiance on a tilted surface	W/m^2
k	Calibration constant	$DN/Ws/m^2$
L_N	Length (Height) of a parabola	m
(L,M,N)	Direction cosines of the X, Y, and Z cartesian directions, respectively	-
n	Refractive index	-
n_r	Number of reflections	-
$\langle n_r \rangle$	Average number of reflections	-

Q_i	Radiative power going through the inlet aperture	W
Q_o	Radiative power going through the outlet aperture	W
R_β	Geometric Factor for calculating optical efficiency of diffuse radiation	-
$\boldsymbol{s}$	Solar vector	-
S	Solar constant	W/m^2
$S_{s\text{-}Type}$	Thermocouple constant	V/°C
T_s	Temperature of the Sun's surface	K
T	Temperature	°C

Greek Characters

α_{in}	Tilt angle of the aperture, measured from the horizontal reference plane	°
α_s	Solar altitude	°
$\alpha_{abs,sol}$	Absorber absorptance in solar spectrum	-
β / β_t	Surface tilt angle	°
β_{max}, β_{min}	Acceptance angles, with respect to the normal of the inlet aperture	°
γ_s	Solar azimuth	°
δ	Solar declination angle	°
δ_{in}	Small addition to the acceptance angle due to the presence of a restriction on the exit angle of a concentrator	°
Δ	Change in value	-
$\epsilon_{abs,IR}$	Absorber emittance in IR spectrum	-
ζ_s	Solar zenith	°
η_{acc}	Acceptance efficiency	-
η_{heat}	Ratio of heat extracted from the absorber, either useful or losses	-
η_{op}	Optical efficiency	-
θ_s	Angular width of the solar disk	°
θ_{in}	Input/Inlet angle, design angle, half-acceptance angle	°
θ_{out}	Output/outlet angle	°
ϑ	Incidence angle	°

ρ	Reflectance	-
ρ_a	Albedo	-
σ	Tilt angle of the optical axis / tilt angle of a tilted CPC / standard deviation	°
σ_{GHI}	Uncertainty of GHI measurement	W\m^2
σ_{DNI}	Uncertainty of DNI measurement	W\m^2
σ_{gV}	Uncertainty of grey value measurement	DN
σ_k	Uncertainty of calibration	DN/Ws/m^2
σ_{Ho}	Uncertainty of output irradiance	W/m^2
τ_{in}	Inlet tilt angle, measured from the surface perpendicular to the optical axis	°
τ_{out}	Tilt angle between vector normal to physical outlet area and bisector of the exit edge rays	°
ϕ	Latitude	°
φ	Angle between straight section of θ_{in}/θ_{out} concentrator and optical axis	°
ω	Hour Angle	°

Abbreviations

ACPC	Asymmetric Compound Parabolic Concentrator
CPC	Compound Parabolic Concentrator
CPV	Concentrating Photovoltaics Systems
CPVT	Concentrating Photovoltaic Thermal Systems
CSES	Contactless Solar Evaporation Structure
CSP	Concentrating Solar Power Systems
CST	Concentrating Solar Thermal Systems
DHI	Diffuse Horizontal Irradiance
DNI	Direct Normal Irradiance
GHI	Global Horizontal Irradiance
MCRT	Monte Carlo Ray Tracing

Subscripts

Abs / absorber	absorber
d	From diffuse irradiance
G	From global horizontal irradiance
i / in	Incident/incoming/inlet
IR	Infrared
N	From DNI
o / out	Outlet/outgoing
r	Reflection / From reflected irradiance
sol	solar

Chapter 1: Introduction

1.1 Motivation

The Sun is the most abundant energy source on earth, at any given moment there are over 150,000 TW [1] of solar power hitting the earth, of which 55% reaches the surface of the earth. If this were to be distributed over the whole year, it would result in 2.6×10^{12} TJ, and considering the whole world utilized 4.18×10^{8} TJ of energy in 2019 [2], its safe to determine that the Sun would be able to power earth thousands of times over. Nevertheless, solar radiation reaching the surface of the earth is very dilute, reaching only up to 1000 W/m^2, this is not useful for applications that require temperatures higher than 150°C [3]. To solve this issue, concentrating solar power (CSP) systems use solar concentrators to concentrate the solar radiative flux to be able to reach higher temperatures for various applications. Using these systems, the maximum concentration achievable would be ~45,000× to achieve a maximum theoretical temperature equal to that of the Sun itself, 6050°C [4]. CSP systems can be classified into concentrated solar thermal (CST) and concentrated photovoltaics (CPV), and a combination of the two. CST systems concentrate solar radiation to use it as heat, whereas CPV systems attempt to increase the efficiency of solar panels by increasing the irradiance reaching the photovoltaic cells. Photovoltaic panels in CPV systems tend to overheat because are irradiated with more concentrated light [5]. To solve this issue, they usually include methods of removing excess heat from the panels, which can be quite significant. Therefore, Concentrated Photovoltaic and Thermal systems (CPVT) are much more common than CPV systems as they cogenerate electricity using PV cells and extract useful heat from the panels. CSP applications can be divided into low, medium, high, and ultrahigh temperatures, ranging from 20°C to more than 1500°C, and can be used for water heating, absorption chillers, electricity generation, solar fuels, among others (see Figure 1.1)[6].

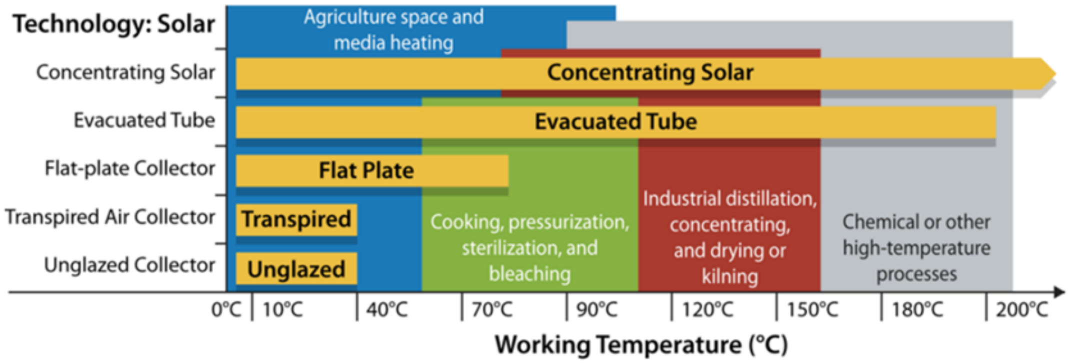

Figure 1.1 - Estimated temperature range for solar thermal technologies

Solar concentrators used in CSP systems work by funneling or reflecting radiation into an area of interest, but to do so the Sun (source of radiation) must be within their “field of view”, or acceptance range. Leading to two possible avenues, follow the Sun’s position or widen your “field of view” to be able to “see” it. Based on this, solar concentrators can be classified into two-axis tracking, one-tracking and stationary concentrators, based on their capabilities to follow the motion of the sun during the day. This plays a big role in the maximum concentration achievable by each of these systems because there is an inverse relationship between concentration and acceptance range. And since higher concentration often leads to higher temperatures, the tracking-based classification is often linked to temperature. With two-axis tracking being in the higher end of temperatures and stationary concentrators being in the lower end. In 2018, residential and commercial heating used up 24% of the total final energy consumption in Canada, with the industrial sector taking 22.9% [7]. Solar energy can play a significant role in these sectors, where the necessary temperatures range from 20°C to 400°C [8], [9]. This aligns well with the capabilities of stationary concentrators, which are the most common concentrators at these temperatures. This is because tracking systems stop being economically viable due to their high price point and maintenance cost[10]. CSP systems are often implemented for temperatures higher than 150°C, because of the difficulty of reaching these temperatures using only absorbers [3], but, depending on the application, concentrators can be useful for lower temperatures as well.

The solar concentrators used in CSP systems can be defined as non-imaging optical devices that concentrate solar radiation with specially designed surfaces [11]. The best examples of these are compound parabolic concentrators (CPCs), which are composed of two symmetrical parabolas that funnel radiation to its outlet. These are ideal concentrators because they accept all radiation within their designed acceptance range (acceptance angle) and reject all that is outside of it [4], [5], [11]. Similarly, Asymmetric CPCs (ACPCs), a variation of the CPC using asymmetric parabolic profiles, are also ideal concentrators and can reach higher concentrations than their symmetric counter parts. Because of this, they have been highlighted as promising designs for seasonal and yearly concentration. Inspired by this motivation, this work aims to investigate into stationary ACPCs, their performance and applications.

1.1. Literature Review

Asymmetric Compound Parabolic Concentrators, or ACPCs, are a variation of CPCs initially proposed by [4] in 1976, and sometimes considered to be the overarching base design for which symmetrical CPCs are just a possible category. Since its introduction, [12] developed the thermodynamic basis and the maximum concentration of asymmetrical non-imaging ideal concentrators and demonstrated that ACPCs can reach higher concentrations than symmetrical ones through a theoretical analysis in 1979. Later in 2005, [13] derived a useful expression for the maximum concentration of an asymmetric (and symmetric) concentrator, based on the entrance's aperture orientation. Building on this work, in 2017 [14] developed tools for determining the acceptance angles after a design is constructed. Also demonstrated the asymmetric nature of étendue and angular acceptance for ACPCs, providing derivations for both, and showed the uniformity of the distribution of these two quantities using ray tracing. Lastly, as seen in the definition of maximum concentration for a 3D concentrator, these collectors can reach much higher concentrations than their 2D counter parts, with 3D concentrators created by rotating the profile around the axis of symmetry. But because of the asymmetric nature of ACPCs, its not trivial to construct a 3D ACPC (because they are not axisymmetric). That being said, most recently in 2020 [15] introduced a method to design a three-dimensional asymmetric concentrator following the design principles of ACPCs, demonstrating a step forward in the conception of true 3D ACPC.

Current implementations of ACPCs are in the areas of concentrating photovoltaic thermal systems (CPVT), concentrating solar thermal systems (CST), integrated collector storage system (ICS) and illumination. These applications take advantage of the ACPC's higher concentration and compactness due to their asymmetry, and most commonly use tubular receivers to extract useful heat. Starting with ICS systems, [16], [17] studied the optical performance of a single and multivessel ICS solar water heater, respectively. These were composed of one or two water storage tanks, surrounded by respective ACPC trough collectors, reaching optical efficiencies of 0.75 to 0.91. CST systems usually operate using an evacuated tube to improve the thermal efficiency, in this research area various ACPC designs have shown promising performance [18], [19]. The most common application of concentrators involves cogeneration of electricity and heat, as is the case for CPVT system. Various numerical and experimental studies have been performed on a variety of CPVT system designs, portraying the possible uses of this type of systems [20]–[23]. As seen in literature, it is common to utilize ACPC designs with extreme asymmetry, similar to the "seashell" design presented by [24], because this geometry can provide excellent peak concentration [18], [20], [22], [23]. Though this is common, designs are not limited to extreme asymmetry, and ACPCs are often truncated to fit compact applications such as in the work of [19], [21], [25], [26]. Lastly, [25] presented a "solar window" design that integrated an asymmetric collector which utilized a wavelength selective film to reflect part of the IR radiation towards a tubular receiver, while allowing for visual light to pass through.

Another area of great interest for the design of non-imaging solar concentrators is the source/acceptance map matching method developed by [27]. This is a methodology that uses the range of ray directions available from a radiative source (from the perspective of the receiving solar concentrator) and the range of directions that can be accepted by a chosen collector, to find the appropriate design parameters (acceptance angle) that can maximize concentration (see section 2.6.). In the realm of stationary concentrators, work preceding the source/acceptance map matching method considered the parametrization of both the solar geometry and the acceptance condition of CPCs [28]. Later, in 2017, [14] described the parametrization of ACPCs to further the understanding of the principles behind how these concentrators work. Lastly, [29] developed the framework for using this design methodology for stationary concentrators. These works portray the building blocks for the defining the source/acceptance map matching method for ACPCs as is described in Chapter 3: of the present manuscript.

The examination of methodologies used in previous research in this area can help understand the common practices and state-of-the-art techniques that shape the study of solar concentrators. Like many areas of research, numerical analysis is a crucial tool for the understanding of the performance of solar collectors. In this respect, Monte Carlo ray tracing is the paramount method for performing numerical analyses in this area, showed by its extensive use in literature [5], [18], [19], [23], [25], [27], [30], [31]. Common software used for ray tracing include *LightTools*, *OptisWorks*, *Radiance* and *MATLAB* (*VeGaS+*), among others [5], [31]. This tool is often used to study the optical performance of concentrators, including the acceptance and number of reflections. The present work utilizes *VeGaS+* through *MATLAB* to perform the numerical optical analyses outlined in Chapter 4: , mainly drawing on the work performed by [31].

The experimental methodology seen in literature for measuring the performance of solar concentrators can divided between thermal, electrical, and optical measurements, or between indoor and outdoor testing. Thermal and electrical measurements are most common for studies where the main interest is the performance of a CST or CPVT system, as a whole. This is seen in the work performed by [20], [21], [23], where both the temperature of the heat transfer fluid and the electrical output of the PV cells were measured (among other factors). On the other hand, optical measurements focus only on the performance and behaviour of the concentrator. This is often performed on concentrators with flat outlets (such as regular CPC and ACPC troughs) by illuminating the concentrator with a known irradiance and measuring the irradiance at the outlet using a thermopile sensor or a PV cell as a sensor, like the method described by [32]. Most notably, outdoor experiments portray the true practical performance of solar concentrators, for these experiments the measurement of irradiation is of outmost importance. This is mostly performed via pyranometers and pyrheliometers to measure global horizontal irradiance and direct normal irradiance [21], [23], with some researchers also using PV cells to measure GHI[22].

1.2. Technological Gap and Scientific Question

Previous research has focused on the theoretical aspects of ACPCs, thoroughly describing the characteristics of these concentrators and their capabilities [4], [12], [14], [15]. Even though ACPCs are ideal for summer-winter[1] use and can reach higher peak concentrations than their symmetric CPC counterparts (for the same acceptance angle), they tend to provide lower effective concentration in the summer which gradually increases towards the winter (assuming a horizontal outlet) [11], [12], [14]. Following the concept of source/acceptance map matching, a new design was proposed where a removable flat wall is added to an ACPC designed for the winter, deemed from here on as Seasonally Adaptive ACPC[29]. This flat wall would be parallel to the optical axis and therefore would serve as an extension to tilt the opening for the summer months where the Sun is higher in the sky, this would then be removed for the winter months.

As mentioned in the literature review, previous researchers have used source/acceptance map matching procedures for the design of concentrators, but not for stationary ACPCs [27], [28]. Those that have analyzed stationary concentrators using similar methods have been limited to symmetric CPCs [28]. Similarly, previous stationary concentrator designs have failed to capture the Sun year-round in high latitudes while maintaining significant concentration [28]. Even though the Seasonal ACPC promises to solve this technological gap, the work previously performed only proposed the design, and didn't develop

[1] In this work, the term "summer" will be used to refer to the period of the year between the spring and fall equinox (starting on March 23rd finishing on September 23rd) and "winter" for the period between fall and spring equinox (starting on September 23rd and finishing on March 23rd).

a thorough analysis, consider modifications, nor test it through numerical or experimental procedures [29]. Even with these unknowns around the Seasonal ACPC, the promise of high concentration in the summer and winter justifies investigating further into this concept and finding ways to optimize it for deployment at high latitudes. Based on these considerations, the research question has been identified as: How to describe and optimize the performance of the Seasonally Adaptive ACPC to maximize concentration at high latitudes and what are its optical properties?

1.3. Objectives

Based on the previous research question, the overarching goal of the research is to design a Seasonally Adaptive ACPC that can maximize concentration in both winter and summer at high latitudes and investigate its optical properties. To achieve this goal, the following set of objectives has been outlined.

(1) Evaluate the theoretical concentration of the Seasonally Adaptive ACPC, how it changes through the year and how it is affected by changes in the design parameters.
(2) Establish a design method for the Seasonally Adaptive ACPC based on source/acceptance map matching and implement it to construct a functional prototype.
(3) Develop a series of Monte Carlo Ray Tracing numerical models to evaluate the optical performance of the Seasonally Adaptive ACPC.
(4) Quantify the optical performance of the Seasonally Adaptive ACPC by performing outdoor experiments using a functional prototype.
(5) Validate the theoretical performance of the Seasonally Adaptive ACPC using experimental results.
(6) Quantify the performance of the Seasonally Adaptive ACPC prototype when employed for outdoor solar-driven desalination.

1.4. Thesis Outline

The main focus of this Master's thesis is to study and describe the optical performance of a the Seasonally Adaptive ACPC via numerical and experimental analyses. To achieve this goal, this work describes the theory behind ACPC as stationary concentrator, a model of the performance based on the available irradiance, the design and development of a concentrator prototype, as well as an innovative method to perform flux mapping experiments. Along with this, this work also implements numerical analyses to quantify the optical parameters that play a role in the performance of the Seasonally Adaptive ACPC, which are implemented in the above-mentioned model.

Chapter 2: covers all the background theory and concepts necessary to understand the rest of this work. Starting with the Sun as a source of radiation for earth, describing the characteristics of its motion in the sky and the different directional distributions of irradiance that reach the surface of the earth. Then the main concepts of non-imaging optics are introduced including geometrical concentration, flux concentration, the thermodynamic limit of concentration, the Compound Parabolic Concentrator (CPC), and the concept of acceptance. This guides the way into some aspects of solar collectors, such as the maximum theoretical temperature achievable and the possibility of controlling the angular range exiting a concentrator. Followed by the most relevant aspects of stationary concentrators, such as the fundamental limit of concentration and the effect of that the angle of incidence of radiation has on the concentrating performance of these devices. And introduce one of the most popular variations of CPCs, asymmetric CPCs, along with a dive into its geometry and definition of geometrical concentration. Then, the concept of source – acceptance map matching is recognized as a useful tool for the design of concentrators, and the methodology for this procedure is covered. Lastly a set of relevant performance metrics of solar concentrators are introduced, including optical efficiency, acceptance efficiency, transmission angle curved and number of reflections, as well as how to calculate them.

Chapter 3 focuses on the design portion of the research, starting with the introduction and description of the three cases of asymmetric θ_{in}/ θ_{out} concentrators, and how this modification changes the performance of these devices. This is followed by the development of the methodology for source - acceptance map matching for asymmetric CPCs, which includes the parametrization of the Sun as a source for stationary concentrators and the parametrization of the acceptance condition for asymmetric CPCs. This is accompanied by an example design for Toronto's latitude, showcasing the capability of reaching high concentrations using this methodology. This paves the way for the introduction of the Seasonally Adaptive ACPC as a design, including the two semi-annual configurations, called summer and winter configurations. Following this, design considerations and performance of the concentrator are covered, including the introduction of a model for the estimation of concentrated solar flux based on available solar irradiance. Then a short analysis on the concentrating capabilities at different latitudes is presented. Lastly, an especially versatile design of the Seasonally Adaptive ACPC is introduced and used for the development of a prototype. The theoretical performance of said prototype is discussed, reaching a maximum flux concentration of 1.78×. Within this section the development and manufacturing of the prototype is also covered, and most notably an innovative method for the construction of parabolic profiles is introduced. This method allows for the fast redesign of CPCs by allowing the designer to reconfigure the prototype to the desired shape and acceptance angle.

Chapter 4 discuses the methodology used for the study of the Seasonally Adaptive ACPC, including numerical analysis and experimental procedures. The numerical studies, performed using the Monte Carlo Ray tracing method, are developed to analyse the optical performance of the design. To achieve this, the numerical studies included the analysis of the acceptance to obtain the transmission-angle curve of the concentrator. Along with the analysis of the performance under direct irradiance, imitating the experimental tests. Finally, a numerical study on the optical performance under diffuse irradiance is introduced. All numerical studies were performed using *VeGaS+* through *MATLAB*. The experimental methodology covers the introduction of a novel procedure for measuring the flux at the outlet of a concentrator. This procedure is shown to implement thermopile sensors, a camera and a Lambertian target to continuously obtain maps of the irradiance distribution at the outlet of the concentrator. The experiments following this procedure were all performed under real solar irradiance.

Chapter 5 dives into the analysis of the results obtained from the methodologies in Chapter 4, and does so by subdividing it into simulation results, experimental results, and discussion. The first begins by portraying the transmission-angle curve obtained and observing its deviance from the ideal case. Then follows with the confirmation of the theoretical performance under direct radiation. And finishes on the verdict that the concentrator design can not only accept a significant portion of the diffuse and reflected irradiances, but also concentrate diffuse radiation using the winter configuration. This is followed by the results of the flux mapping experiments, which are subdivided into summer, equinox, and winter, depending on the time of the year they were performed. This section covers all the specifics of the test and observations on the concentrations and irradiances reached, as well as the point when the concentrator stops providing useful concentration (lower than 1×). Finally, the discussion section begins with an analysis on the resulting output flux through the year, showcasing the achievable irradiances on different seasons and using this to draw conclusions on the performance of the concentrator and its applications. This is followed by the qualitative analysis of the flux distribution by using the maps obtained from the experiments and simulations. Conclusions are drawn on the manufacturing precision of the concentrator shape and on the effect that the irradiance distribution can have on the practical uses of the concentrator. Lastly, a short analysis on the optical efficiency achieved during the experiments is performed, comparing with a theoretical model of the optical efficiency based on the numerical results of number of reflections, and commenting on the observed reflectance of the concentrator.

Chapter 6 describes the implementation of the Seasonal Adaptive ACPC prototype for solar-driven desalination, starting with an introduction the importance of solar desalination in the current world. This is followed by an overview of the innovative solar desalination device used in conjunction with the concentrator prototype. This chapter then dives into the experimental methodology implemented, commenting on the specifics of the contact between the concentrator and the devices' absorber. Lastly, the results of this experiment are presented, diving into a discussion on the temperatures, mass flux, concentration and efficiency achieved.

Chapter 2: Background & Theory

This chapter provides a comprehensive background into the theoretical basis required to understand the contents of this work. More specifically, this chapter covers key aspects of solar radiation, non-imaging optics, as well as developments concentrating solar collectors and their performance criteria, setting the stage for subsequent analysis, design, and evaluation in the following chapters. For those who posses' prior knowledge of the topics highlighted here, this chapter will serve as a review.

2.1. Solar Radiation

The radiation emitted from the sun can be described as that of a blackbody at the sun's temperature of T_s = 5780 K [33]. With the sun measuring ~1.4×10^6 km in diameter and located at ~1.496×10^8 km from the earth, from the solar disc occupies an angular width θ_s of 0.266° [33]. This also defines the angular range of the radiation incoming from the sun to 0.266°. With the sun emitting 6.31×10^7 W/m^2/sr of radiation at any given moment, and the angular width mentioned, the amount of solar flux reaching the earth is 1367W/m^2 (extraterrestrial irradiance), often referred to as the solar constant (S)[33]. Nevertheless, the irradiance that reaches the surface of the earth is smaller than this quantity because radiation gets absorbed and scattered as it travels through the atmosphere before reaching the earth's surface.

2.1.1. Sun – Earth Geometry

It's possible to describe the position of the sun from the perspective of the earth (geocentric) using the horizon reference frame system shown in Figure 2.1. This is the coordinate frame that will be utilized in the rest of this work, unless otherwise stated. As seen in Figure 2.1, this coordinate frame follows the Cartesian Coordinate system, defining the North direction as the positive Y-axis direction, East as the positive X-axis direction, and the Z-axis pointing in the direction normal to the earth's surface. In this work, the convention used for measuring angles is to consider clockwise as positive and counterclockwise are negative. Following these coordinates, a unit vector **s** directed from the observer to the center of the solar disk can be used to define the position of the sun in the sky. The direction of this solar vector **s** can be defined by the solar altitude α_s and solar azimuth γ_s. These two angles are analogous to the spherical coordinate system, with solar altitude being defined as the angle between **s** and the XY plane, or polar angle. The solar zenith angle ζ_s can also be used to characterize the solar vector in the same way as the solar altitude, as their addition must total 90°. The solar azimuth is analogous to the azimuthal angle, measured from the negative Y axis to the solar vector. It's important to note that the coordinate system shown here is biased toward the northern hemisphere and might cause an added level of complexity to utilize it for defining the same parameters for the southern hemisphere.

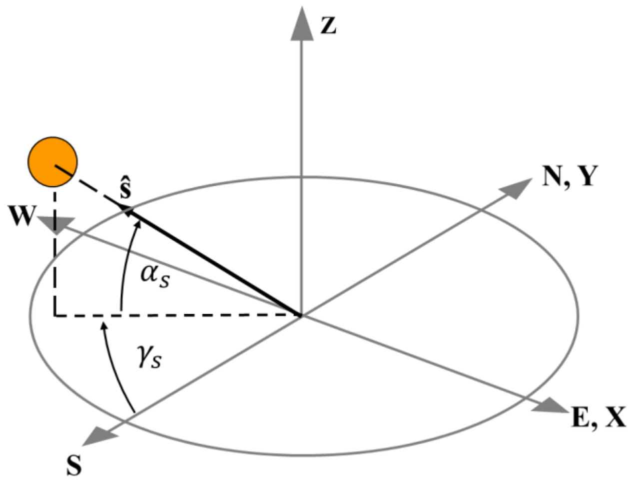

Figure 2.1 - Cardinal Coordinate Frame (*X, Y, Z*) to express the sun-earth geometry.

Following this coordinate frame, the solar vector can be defined in terms of the solar angles as:

$$\boldsymbol{s} = [-\sin\gamma_s \cos\alpha_s \quad -\cos\gamma_s \cos\alpha_s \quad \sin\alpha_s]$$

Equation 2.1 - Solar Vector

Similarly, the direction of the solar vector can also be described using the solar declination angle δ, latitude ϕ of the observer and hour angle ω. With the solar declination being defined as the angle made between the solar vector and the earth's equatorial plane, resulting in Equation 2.3 [28], [34].

$$\boldsymbol{s} = [-\cos\delta \sin\omega \quad \cos\phi \sin\delta - \sin\phi \cos\delta \cos\omega \quad \sin\phi \sin\delta + \cos\phi \cos\delta \cos\omega]$$

Equation 2.2 - Solar vector in terms of declination, latitude, and hour angle.

Based on this definition, δ is delimited by 23.45° in the summer solstice and -23.45° in the winter solstice.

$$\sin\delta = -\sin 23.45° \cos\left(\frac{360°(n+10)}{365.25}\right)$$

Equation 2.3 - Solar declination δ

And the hour angle is defined in Equation 2.4, where t = 0 at solar noon, t > 0 after solar noon, and every hour represents an increase in 15°.

$$\omega = \frac{360°}{24hr}t$$

Equation 2.4 - Hour Angle ω

These angles are related to α_s, γ_s and ζ_s according to these equations[34]:

$$\sin\alpha_s = \cos\phi\cos\delta\cos\omega + \sin\phi\sin\delta$$

Equation 2.5 - Solar Altitude α_s

$$\tan\gamma_s = \frac{\sin\omega}{\sin\phi\cos\omega - \tan\delta\cos\phi} = \frac{-\sin\omega\cos\delta}{\cos\alpha}$$

Equation 2.6 - Solar Azimuth γ_s

$$\cos\zeta_s = \cos\phi\cos\delta\cos\omega + \sin\phi\sin\delta$$

Equation 2.7 - Solar Zenith ζ_s

2.1.2. Directional Distribution

As stated before not all radiation reaching the top of the atmosphere reaches the earth's surface, but the portion of radiation that makes it through the atmosphere without being absorbed or scattered is called direct solar radiation. This type of radiation is characterized to have an angular span equal to the angular width of the solar disk. On the other hand, the radiation that is scattered as it travels through the atmosphere is called diffuse solar radiation and is responsible for the illumination of the sky. Similarly, there is a portion of the direct radiation that is forward scattered and creates a bright circumsolar region around the solar disk. This circumsolar radiation shows angular symmetry around the center of the solar disk and has an angular span larger than θ_s. The amount of circumsolar radiation is often considered to be 20% of the direct radiation (which can vary depending on the atmospheric conditions). Considering its relative brightness and small angular span, it is often considered to be play an important role in the field of concentrating solar power (CSP) [35], [36].

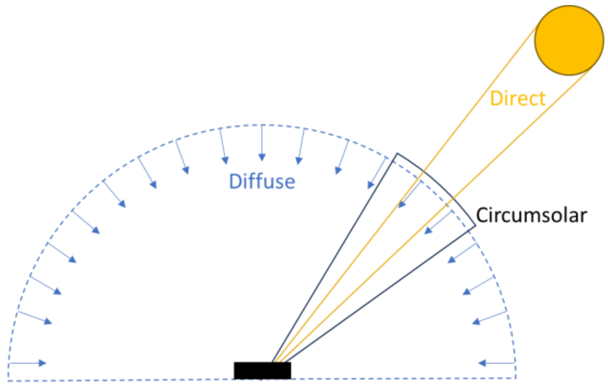

Figure 2.2 - Components of Solar Irradiance

2.1.2.1. Components of Solar Irradiance

The radiative flux reaching the surface of the earth (horizontal surface), or Solar Irradiance, can be described by a single value, the global horizontal irradiance or GHI (H_G). This term includes all forms of irradiance reaching the earth's surface as described above and can be calculated using Equation 2.8 (see Figure 2.2)[37]. The direct component of the solar irradiance is called direct normal irradiance, or DNI (H_N), and is the part of the solar radiation that reaches the earth's surface undisturbed. This term is related to GHI by the projection of the DNI onto the normal vector of the earth's surface, or direct beam irradiance (H_b), marked by angle ζ_s. Because of the circumsolar radiation's small angular span, it is common to include the circumsolar irradiance within the DNI term in CSP applications [35].

$$H_G = H_b + H_d + H_r = H_N \cos \zeta_s + H_d + H_r$$

Equation 2.8 - Global Horizontal Irradiance[2]

Similarly, the term diffuse horizontal irradiance or DHI (H_d), encompasses the diffuse component of the solar irradiance. In this work, this term will also include any reflected radiation from surrounding surfaces, with the exception of ground reflections, which will be characterized by the term reflected irradiance H_r. For a horizontal surface, the term H_r is often neglected, but becomes more significant for inclined surfaces. For these types of surfaces, a variation of GHI can be written as H_β, and has the following definition[37], [38], where ϑ is the incidence angle for the tilted surface, which is further defined in section 2.4.2.

$$H_\beta = H_N \cos \vartheta + H_{d\beta} + H_r$$

Equation 2.9 - GHI for a tilted surface

[2] This equation can also be written in terms of the acronyms GHI, DNI, and DHI.

2.2. Fundamentals of Non-imaging Optics

Non-imaging optics, sometimes called anidolic optics, is a branch of geometrical optics which seeks to maximize the efficiency of collection, concentration, and distribution of light. To do so, non-imaging optics deals with optical devices that capture and redirect light without forming an image. This non-imaging characteristic allows for more efficient concentrators that even approach the theoretical limit [11], [39], [40].

2.2.1. Geometrical Concentration Ratio

In general terms, any optical system or device will have an entry and exit apertures with dimensions A_i and A_o, respectively, and the ratio of these two quantities is called geometrical concentration ratio[3] C_g, seen in Equation 2.10. This unitless ratio represents the highest concentration that an optical system with a given geometry can achieve, regardless of the proficiency of the system to transmit rays into the exit aperture.

$$C_g = A_i/A_o$$

Equation 2.10 - Geometrical Concentration Ratio

Whereas the geometric concentration ratio defines the highest concentration achievable by a given geometry, there is an upper limit for concentration for an optical system with a prescribed input angle θ_{in} and ratio of refractive indices[4] n. This maximum geometric concentration ratio $C_{g,max}$ is defined in Equation 2.11 for a 2D device, and can be obtained by considering the conservation of étendue as explained by [40] and [11].

$$C_{g,\max} = \frac{n}{\sin\theta_i}$$

Equation 2.11 - Maximum Geometric Concentration Ratio for a 2D concentrator

Equation 2.11 assumes that radiation exits the concentrator with an angle of π/2. Even though concentration, as defined above, is a unitless quantity, in this work values of concentration are given a dimensionless unit ×, to give context to the values reported[5]. Considering that $C_{g,max}$ is inversely proportional to the sine of the design angle θ_{in}, minimizing this angle would result in the maximum possible concentration for a two-dimensional concentrator $C_{ideal,2D}$. With the sun being the source of

[3] From this point forward the term “ratio” is often be excluded when discussing concentration ratios, for conciseness.
[4] Refractive index inside the concentrator to refractive index outside the concentrator.
[5] The unit × can be pronounced as the letter “x”.

radiation, this $C_{ideal,2D}$ can be achieved by limiting θ_{in} to be equal to the angular width of the sun θ_s, resulting in a $C_{ideal,2D}$ of 213×[6] [4].

$$C_{ideal,2D} = \frac{1}{\sin(\theta_s)} \cong 213 \times$$

Equation 2.12 - Ideal (maximum) concentration for a 2D concentrator

2.2.2. Flux Concentration

Alternatively, concentration can be defined as the ratio of irradiance, or incident radiative flux, on the outlet aperture H_o and on the inlet aperture H_i, called flux concentration ratio C_f, seen in Equation 2.13. This quantity is related to the geometric concentration as seen in Equation 2.13, where η_{op} is the optical efficiency of the concentrator (defined in 2.7.1). Similarly, the maximum value of achievable by C_f is C_g, and occurs when η_{op} = 1.

$$C_f = \frac{H_o}{H_i} = \frac{Q_o/A_o}{Q_i/A_i} = \frac{Q_o}{Q_i} C_g = \eta_{op} \cdot C_g$$

Equation 2.13 - Flux Concentration Ratio

2.2.3. Compound Parabolic Concentrators (CPCs)

A compound parabolic concentrator, or CPC, is a non-imaging optical concentrator consisting of two symmetrical parabolic reflectors that redirect radiation from the inlet to the outlet apertures. This concentrator is considered ideal since its geometrical concentration is equal to the maximum theoretical concentration [40]. The geometry of the CPC is defined only by the design angle θ_{in} (also called half-acceptance angle), and the size of the outlet aperture, the former is used to determine the shape of the two parabolas. With each parabola having their focus located at either edge of the outlet aperture, the axis of each parabola is made to make an angle θ_{in} with the axis of symmetry of the CPC. The resulting geometry can be seen in Figure 2.3, where the outlet is segment *OO'*. Rays r_1 and r_2 are called edge rays, as they represent the maximum angle that a ray can make with the axis of symmetry and still reach the outlet. The vertical line shown in this figure is both the axis of symmetry, and the optical axis (O.A.) of the CPC, defined as the line bisecting the edge rays.

[6] Assuming a refractive index equal to 1.

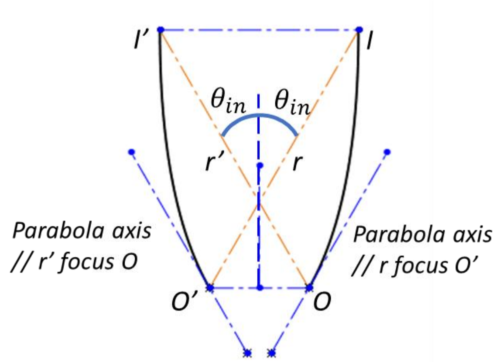

Figure 2.3 - Compound Parabolic Concentrator

CPCs are also characterized by their ability to accept all radiation entering the inlet area with an incident angle within their design angle and reject all radiation outside of it. As explained by [11], this is the case for the 2D CPC, but not for 3D CPCs[7], and can be demonstrated by plotting the transmission-angle curves (see section 2.2.4) of the 2D and 3D CPCs.

2.2.4. Acceptance

Acceptance is a property of concentrators that measures the ratio of rays hitting the receiver to rays entering through the inlet area, defined by [11] using Equation 2.14. This equation describes acceptance for CPCs but can be generalized for all concentrators.

$$Acceptance = \frac{number\ of\ rays\ hitting\ the\ receiver}{number\ of\ rays\ entering\ the\ CPC}$$

Equation 2.14 - Acceptance of a concentrator

Acceptance is commonly described as a function of the incidence angle ϑ and called acceptance function *F(*ϑ*)*[41]. This function is usually used to analyze the behavior of concentrators as ϑ changes. The curve obtained by plotting *F(*ϑ*)* against ϑ, is called transmission-angle curve, and an example of it can be seen in Figure 2.4. This figure plots the transmission-angle curve of a 2D CPC, which as explained in the previous section, *F(*ϑ*)* is 1 for $-\theta_{in} < \vartheta < \theta_{in}$, and zero for $\vartheta < -\theta_{in}$ and $\vartheta > \theta_{in}$. Because of this relationship between acceptance and the design angle θ_{in}, this angle is often called acceptance angle.

[7] 3D CPC are 3 dimensional concentrators constructed by rotating the CPC geometry around its central axis.

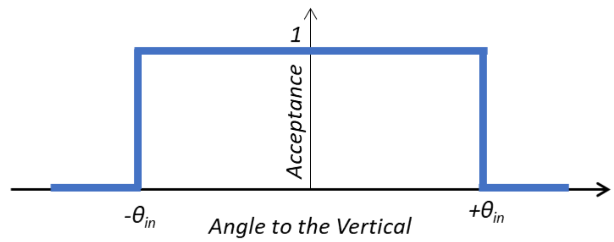

Figure 2.4 - Transmission-angle curve

Consider Equation 2.11, if it is desired to maximize the theoretical concentration of a solar concentrator, then one of the main methods to do so is to minimize the acceptance angle. Because of this, most solar concentrators focus on the collection of direct radiation, and not diffuse, because the angular distribution of the latter would result in a design with near-zero concentration. Even though designers are often concerned with just the direct radiation, a solar concentrator can still accept a portion of the diffuse radiation, given by Equation 2.15, which gives the ratio of accepted diffuse radiation to total diffuse radiation [39].

$$\frac{H_{d,i}}{H_d} = \frac{n}{C_{g,max}}$$

Equation 2.15 - Ratio of diffuse radiation collected by a solar concentrator.

2.2.5. Ray representation in direction-cosine space

Geometrical optics often depicts radiation in the form of rays, which are idealized geometrical representations of how electromagnetic radiation propagates through a medium and can be represented as a vector. Like any vector, for any ray **r** to be defined in three-dimensions it requires a point **P** and a unit vector **v**. It's convenient to define **v** in terms of direction cosines *L*, *M* and *N*, which, since they are related by $L^2 + M^2 + N^2 = 1$, means that **v** can be defined using only two of its components (e.g., *L* and *M*). As explained above, for an ideal concentrator in non-imaging optics all radiation that intercepts the inlet aperture with an incidence angle within θ_{in} is accepted. Meaning that the location where a ray intercepts the inlet area doesn't contribute to determining its acceptance, all that matters is whether the ray is within θ_{in}. This realization allows to simplify the definition of a ray into only the *L* and *M* components of its unit vector **v**.

Because of this simplified definition of a ray **r**, it's possible to plot any ray onto direction cosine space (L-M space), bounded by a unit circle; take example of the vector in Figure 2.5a which is incident on a surface, and how its *L* and *M* components are plotted onto the direction cosine space. This method of visualizing the ray direction is convenient for understanding the available ray directions for a given application and the performance of various concentrator designs (see section 2.6.).

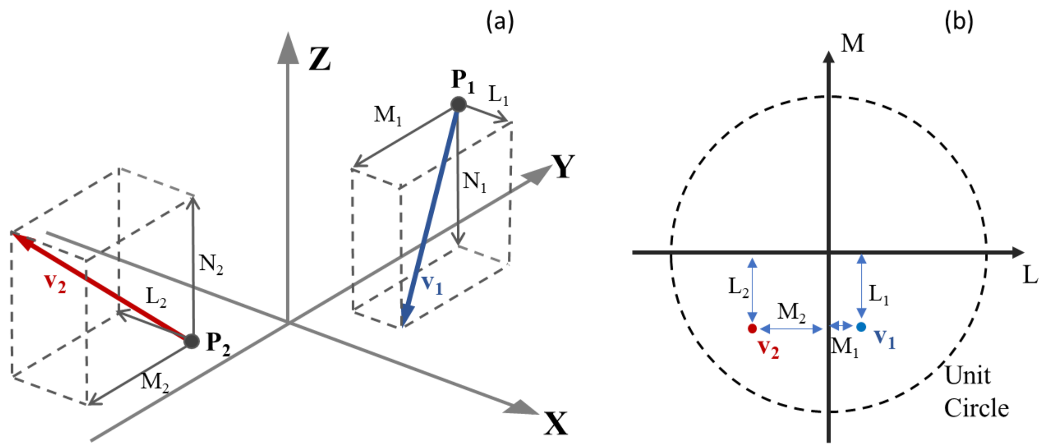

Figure 2.5 - Vector representation of a ray in direction cosine space

2.3. Concentrating Solar Collectors

The main purpose of solar concentrators, concentrating solar collectors, is to accept solar radiation incident on a large area (nearly collimated) and redirect it into a small receiver in an efficient manner.

2.3.1. Second Law of thermodynamics for solar collectors

Since commonly the output for solar concentrators is energy in the form of heat, it would be desirable to understand the maximum possible temperature achievable for a given design. To achieve this, the second law of thermodynamics can be implemented to describe the sun-absorber system and find the temperature of the absorber, while considering both the thermal losses and the useful heat extracted from the absorber. From this analysis, its possible to describe the maximum absorber temperature for a given C_f, as seen in Equation 2.16 [4].

$$T_{abs} = T_s\left[(1-\eta_{heat})\left(\frac{\alpha_{abs,sol}}{\epsilon_{abs,IR}}\right)\frac{C_f}{C_{ideal,2D}}\right]^{1/4}$$

Equation 2.16 - Maximum theoretical absorber temperature

Here, $\epsilon_{abs,IR}$ and $\alpha_{abs,sol}$, are absorber emittance in IR and absorptance of the absorber for the solar spectrum, respectively. On the other hand, η_{heat} is the ratio of incoming solar radiation that is extracted as useful heat or lost by conduction and convection, and $C_{ideal,2D}$ is as defined in Equation 2.12. For an absorber with η_{heat} = 0, and assuming $\epsilon_{abs,IR} = \alpha_{abs,sol}$, the maximum temperature achievable is ~1513K.

2.3.2. Restricted Exit Angles

θ_{in}/θ_{out} concentrators, sometimes called angle transformers or θ_{out} CPCs, are ideal concentrators often defined as a variation or modification of the symmetric CPC design seen in section 2.2.3. These not only accept radiation within a prescribed acceptance angle, but also limits the angular width of the output ray fan to a prescribed θ_{out}. To achieve this effect, a conical section is made from the bottom portion of the parabolic profiles and defined by both θ_{in} and θ_{out}, as seen in Figure 2.6. Limiting the spread of the radiation at the output can improve the absorptance of radiation exiting the concentrator, since most absorber materials demonstrate a low absorptance at high incident angles. Similarly, it facilitates the implementation of a gap between the concentrator outlet and absorbers, preventing thermal shorts. Lastly, implementing the θ_{out} modification removes the curved section at the bottom of the CPC, decreasing complexity in the manufacturing parabolic profiles [40], [42].

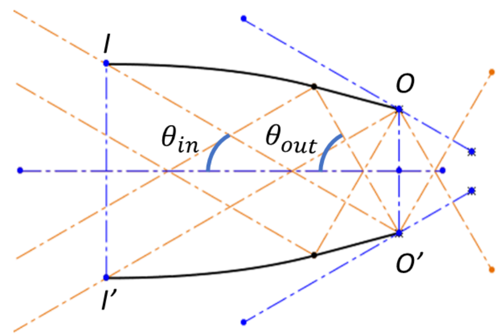

Figure 2.6 - θ_{in}/θ_{out} concentrator

2.3.2.1. Concentration Ratio

The maximum geometric concentration achievable by a concentrator that has an output ray fan characterized with an angle lower than π/2, is defined in Equation 2.17. This definition applies only to symmetrical θ_{in}/θ_{out} concentrators, with asymmetric cases covered in section 3.1. .

$$C_{g,max} = \frac{n_o \sin\theta_o}{n_i \sin\theta_i}$$

Equation 2.17 - Maximum geometric concentration for an ideal concentrator with restricted angles

2.3.2.2. Effect on acceptance efficiency

Even though 2D θ_{in}/θ_{out} concentrators accept all radiation within θ_{in}, and output it within θ_{out}, it does not reject all radiation outside of θ_{in}. Rays that reach these concentrators outside of θ_{in} are redirected into the outlet at angles higher than θ_{out}. Because of this, the transmission-angle curve for these concentrators differs from the one seen in Figure 2.4, by not zeroing at $F(\vartheta) = \theta_{in}$ and linearly approaching zero at some $\theta_{in} + \delta_{in}$ [40], [42].

2.4. Stationary Concentrators

As the name suggests, stationary solar concentrators are a class of solar collectors which collect radiation from the sun without the use of tracking as it moves through the sky. Because they are stationary, they are designed to have wide acceptance angles to accept solar radiation as the solar disk moves in the sky. This in turn limits their concentration, as seen in Equation 2.11, making them much less effective at concentrating radiation when compared to their tracking counterparts.

2.4.1. The fundamental limit of concentration for stationary collectors

Like the maximum geometrical concentration, stationary concentrators have their own theoretical limit to the concentration they can achieve. This limit of concentration for a stationary collector $C_{g,stationary}$, is dependent on the latitude of the observer and the desired daily collection time. Developed by [29], the $C_{g,stationary}$ increases with latitude and with a shorter collection time. For instance, at a latitude of 35° and full day collection is $C_{g,stationary}$ = 2.4×, but for the same collection time at 50° the maximum would be ~3×. This limit of concentration considers a theoretical concentrator that only accepts radiation coming from the possible positions of the sun, in other words, its acceptance map can match the sun's source map perfectly (see section 2.6.). Currently no stationary concentrator has been ideated that can match this theoretical limit. For an existent concentrator design, [28] demonstrated that for an 8-hour collection time and using a tilted CPC[8], its possible to achieve 2.3×.

2.4.2. Incidence Angles

The incidence angle ϑ of solar radiation on a concentrator inlet can be defined as the angle between the normal **n** of said inlet and the direction of the solar vector **s**. ϑ can be described using the declination, latitude, and hour angle together with the tilt angle of the surface (measured from the horizontal) and the surface azimuth (deviation from the south direction) by [38]:

$$\begin{aligned}\cos\vartheta = {} & \sin\delta\sin\phi\cos\beta - \sin\delta\cos\phi\sin\beta\cos\gamma + \cos\delta\cos\phi\cos\beta\cos\omega \\ & + \cos\delta\sin\phi\sin\beta\cos\gamma\cos\omega + \cos\delta\sin\beta\sin\gamma\sin\omega\end{aligned}$$

Equation 2.18 - Incidence angle of solar radiation on a surface

[8] Using a tilt equal to the latitude of the site implemented.

The presence of an incidence angle between **s**(L, M) and **n**(L, M), causes the flux concentration to be a function of ϑ, $C_f(\vartheta)$. This can be seen in Figure 2.7, where the projected area of the inlet changes drastically for the two incidence angles shown. In other words, for a solar concentrator to achieve its maximum possible concentration, the incidence angle of the incoming radiation must be minimized. But this is not possible for stationary concentrators, because of their nature the incidence angle changes throughout the day and year, causing $C_f(\vartheta)$ to fluctuate with $\cos\vartheta$. This results in every day having a maximum at solar noon[9], and a yearly maximum when **s**(L, M) and **n**(L, M) are equal.

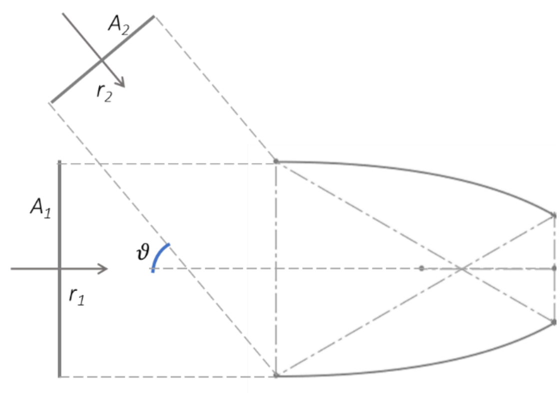

Figure 2.7 - Visualization of the effect incidence angle has on the projected inlet area.

2.5. Asymmetric Compound Parabolic Concentrators (ACPCs)

Asymmetric Compound Parabolic Concentrators, also called Asymmetric CPCs or ACPCs, just like CPCs, are ideal concentrators that use two parabolic profiles to funnel radiation from their inlet aperture into their outlet aperture. Unlike CPCs, ACPCs don't have symmetrical parabolas, because they are defined by two different design angles $\theta_{in,1}$ and $\theta_{in,2}$, as seen in Figure 2.8. These concentrators are well suited for use as stationary concentrators because their difference in acceptance angles can be taken advantage to match the range of positions taken by the solar disk in the sky. Because of this, they are often used for year-round collection, and applications where it is desired to have a significantly different behaviour from one season to the next. An example of the latter would be to design an ACPC so that it works as a concentrator in the winter and a radiative cooler in the summer[10]. ACPCs can also reach higher peak concentrations

[9] Assuming that the surface azimuth angle $\gamma = 0°$.

[10] This can be achieved by designing an ACPC it so that the inlet area projection is near zero in the summer and is maximized in the winter.

than their symmetric counter parts (see section 2.5.2), making them a promising tool for concentrating solar radiation.

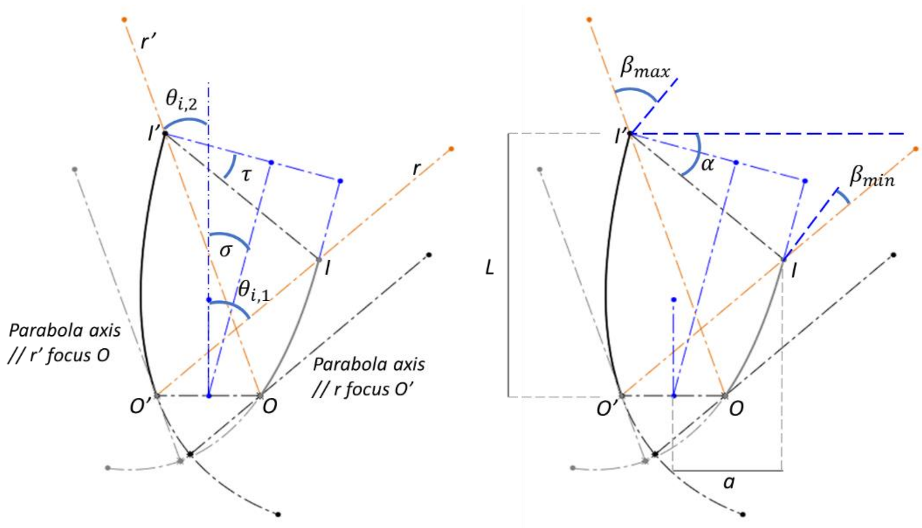

Figure 2.8 - Geometry of an asymmetric CPC, separated into two for clarity.

2.5.1. Geometry of an Asymmetric CPC

In the same way as CPCs, the parabolas that make up an ACPC have their focus on the outlet edge their profile (i.e., parabola *IO* has its focus on point *O'*). Their axes are parallel to the edge ray that meets their edge of the outlet (i.e., axis of parabola *IO* is parallel to edge ray **r'**, which lands on point *O*), in other words the axis of parabola *IO* makes an angle $\theta_{in,2}$ with the vertical axis. Finally, the top edge of the parabola is defined as the point *I* where the parabolic profile meets the edge ray. Because of their asymmetric acceptance angles, the optical axis[11] is not normal to the outlet, as is the case for CPCs, resulting in the optical axis making an angle σ with the vertical plane, as seen in Figure 2.8.

$$\sigma = \frac{\theta_{in,2} + \theta_{in,1}}{2}$$

Equation 2.19 - Tilt angle of the Optical Axis, with respect to the vertical plane

A convenient way to define the acceptance angles for an ACPC is to do so with respect to the normal of the inlet aperture, resulting in β_{max} and β_{min}. These acceptance angles can be used to find the tilt angle τ_{in} between the inlet aperture A_i and A_g (the projection of A_i onto a surface perpendicular to the optical axis), which can be found using Equation 2.20.

[11] The optical axis is the bisector of the edge rays, in other words, the line that splits the

$$\tau_{in} = \frac{\beta_{max} + \beta_{min}}{2}$$

Equation 2.20 - Inlet tilt angle, as measured from the surface perpendicular to the Optical Axis.

The tilt angles τ_{in} and σ can be joined into one tilt angle α_{in}, which is simply the angle between the horizontal plane and the inlet area, which could be found by calculating the dot product of a horizontal vector and the inlet area [14]. Alternatively, α_{in} can be found geometrically using Equation 2.21. Here, L_1 and L_2 are the length (or height) of the parabolas, and a_1 and a_2 are the horizontal distance between the center of the outlet and the top edge of the parabola (see Figure 2.8).

$$\tan \alpha_{in} = \frac{(L_1 - L_2)}{a_1 + a_2}$$

Equation 2.21 - Tilt between vector normal to physical inlet area and horizontal reference plane

The acceptance angles β_{max} and β_{min} can be calculated using Equation 2.22, which shows the general definition of β, which can be applied to either β_{max} or β_{min}.

$$\beta = \theta_{in,N} - \tau_{in} - \sigma = \theta_{in,N} - \alpha_{in}$$

Equation 2.22 - Acceptance angles, measured from the inlet aperture.[12]

Further geometrical parameters of the ACPC include the focal length of each parabola f_1 and f_2 (Equation 2.23), the length of the diagonals *IO'* and *I'O* (marked generally as D_N) defined by the design angles $\theta_{in,1}$ and $\theta_{in,2}$ (Equation 2.24), and the length of each parabola L_N (Equation 2.25), the larger of which defines the total height of an ACPC:

Focal Length of parabola 1: $f_1 = a'\left(1 + \sin \theta_{in,2}\right)$

Focal Length of parabola 2: $f_2 = a'\left(1 + \sin \theta_{in,1}\right)$

Equation 2.23 - Focal Length of the parabola forming an ACPC.

$$D_N = \frac{2f_N}{1 - \cos\left(\theta_{in,1} + \theta_{in,2}\right)} = \frac{f_N}{\sin^2\left(\frac{\theta_{in,1} + \theta_{in,2}}{2}\right)}$$

Equation 2.24 - Length of Diagonal defining $\theta_{in,N}$.

[12] Where *N* is equal to either 1 or 2, to specify each parabola.

$$\text{Length of parabola N: } L_N = D_N \cos\theta_{in,N}$$

Equation 2.25 - Height (or Length) of a parabola

2.5.2. Concentration Ratio

Because of the asymmetry of the concentrator, the outcome of Equation 2.11 is not the maximum geometric concentration for an ACPC, since it doesn't properly consider the two different acceptance angles of the concentrator. A more precise and convenient calculation for the maximum concentration of an Asymmetric CPC was developed by [13]:

$$C_g = \frac{2n}{\sin\beta_{max} - \sin\beta_{min}}$$

Equation 2.26 - Maximum Geometrical Concentration Ratio, using the inlet aperture as reference to define the acceptance angles β.

2.6. Source – Acceptance Map Matching

Source – acceptance map matching method is a design procedure developed by [27], where the position of the radiation source and the acceptance capabilities of a concentrator are parameterized in LM-space (see section 2.2.5) to determine the most effective concentrator design parameters for a given radiation source. This method can be divided into three basic steps:

- Parameterize and plot the source map on direction cosine space (LM-space).
- Parameterize the acceptance map in direction cosines space (LM-space) for a selected concentrator design.
- Overlay the acceptance map on the plotted source map and control the concentrator design parameters (acceptance angles) to have the acceptance map fully envelop the source map.

Because stationary concentrators have a hard time to accept radiation from every sun position, the third step can be modified to have the acceptance map enveloping the desired section of the source map. This would mean defining a specific collection time to determine the acceptance angles of the concentrator.

2.6.1. Source Map for stationary concentrators

The source map is a cosine space representation of all ray directions from the radiative source incident on the collecting surface. It's important to note that the source map is defined for the perspective of the concentrator to be used. For stationary concentrators, the source map can be defined simply using the parametrization of the sun vector in LM-space. Equation 2.2 gives the two components L and M necessary for plotting the source map:

$$\boldsymbol{s} = [L \quad M] = [-\cos\delta\sin\omega \quad \cos\phi\sin\delta - \sin\phi\cos\delta\cos\omega]$$

Equation 2.27 - Source map for a stationary concentrator

For a specific latitude, the two most extreme values of solar declination will define two ellipses that will mark the summer and winter solstice. Plotting the sun vector (Equation 2.27) with respect to ω, for these two values of δ, results in two ellipses that highlight the most extreme sun positions. Within these two ellipses is the total range of sun positions (or ray directions) for the whole year (Figure 2.9).

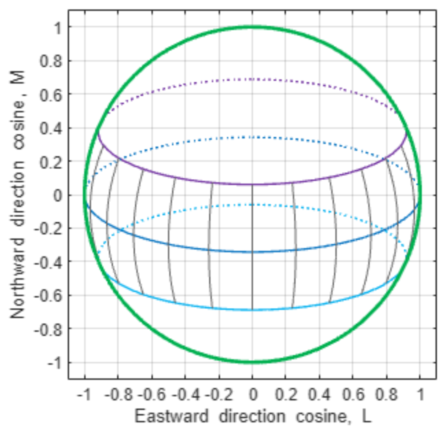

Figure 2.9 - Source map for a stationary concentrator (ϕ = 20°). The purple ellipse is the summer solstice, the blue is the equinoxes, and the clear blue is the winter solstice. Each hour of the day is marked with a vertical line inside the source map.

For a latitude of 0°, the summer and winter solstice ellipses appear as two straight lines (their minor axes are zero), which, as latitude increases, their minor axes increase. This creates a source map with a crescent shape, which gets closer to the lower edge of the unit circle for increasing latitudes[13] (see Figure 2.9).

2.6.2. Acceptance Map for stationary concentrators

On the other hand, the acceptance map is a direction cosine space representation of the range of ray directions that a concentrator design can accept. For a 2D CPC trough extruded across the x-axis (east-

[13] For extremely high latitudes, the winter solstice ellipse disappears from the source map as it folds around the unit circle. Similarly, the summer solstice ellipse appears to form an edge close to the unit circle's circumference.

west) the acceptance map can be obtained by the realization that all rays whose projected angle in the yz-plane are $\leq\theta_{in}$ are accepted, which can be expressed as [28]:

$$L^2 + \frac{M^2}{\sin^2\theta_{in}} \leq 1$$

Equation 2.28 - LM space acceptance condition for a 2D CPC

This is the equation of an ellipse, symmetrical across the L axis, and can be seen in Figure 2.10. For a 2D CPC, the acceptance map marks the edge where the concentrator goes from accepting all radiation, to not accepting any. This is not the case for a non-ideal concentrator which tend to reject some radiation within their acceptance map.

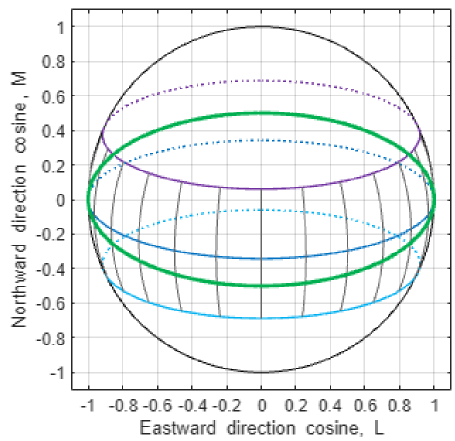

Figure 2.10 - Acceptance map of a 2D CPC

2.7. Performance Metrics of Solar Concentrators

2.7.1. Optical Efficiency

Optical efficiency is one of the main performance criteria for solar concentrators, since it expresses the ratio of energy exiting the outlet aperture to the one entering through the inlet aperture.

$$\eta_{op} = \frac{Q_o}{Q_i} = \frac{C_f}{C_g}$$

Equation 2.29 - Optical Efficiency

This quantity comprehends any losses due to absorption, acceptance, and inaccuracies in the reflector surface, which is reflected in the following equation [43].

$$\eta_{op} = \eta_{acc} \cdot \langle \rho^n \rangle$$

Equation 2.30 - Components of optical efficiency

2.7.2. Acceptance Efficiency

The acceptance efficiency is closely related to the definition of acceptance shown in section 2.2.4. And can be defined, in an integral manner, as the part of the optical efficiency that is related to geometrical losses and is equal to η_{op} in the ideal case where the concentrator surfaces have perfect optical properties [39].

2.7.3. Transmission-Angle Curve

The transmission-angle curve, as introduced in section 2.2.4, is an important tool to evaluate the performance of a concentrator, as it provides a basic understanding of how the concentrator will behave (ignoring reflectance and number of reflections). An ideal concentrator has a transmission-angle curve similar to the one seen in Figure 2.4, and any deviation from this curve is a measure of the non-ideality of a concentrator design.

2.7.4. Average Number of Reflections

The average number of reflections $\langle n_r \rangle$ is a geometrical quantity that describes the arithmetic mean of the number of reflections (n_r) each accepted ray goes through as they make their way into the outlet aperture. With every reflection, a ray loses a portion of its energy by the reflectance of the reflector surface ρ. Considering this, the total energy of a ray as it reaches the outlet can be described by ρ^{n_r}. The average number of reflections is related to the optical efficiency and acceptance efficiency by the expression developed by [24], [43][14]:

$$\eta_{op} = \eta_{acc} \langle \rho^{n_r} \rangle \approx \eta_{acc} * \rho^{\langle n_r \rangle}$$

Equation 2.31 - Effect of reflectivity on optical efficiency

The estimation in this expression holds for high values of ρ. A method to describe the average number of reflections was described by [31], using Monte Carlo ray tracing simulations. This method involves evaluating the optical efficiency of two simulations cases, one with $\rho = 1$ and one with $\rho = 1 - \Delta\rho$, and calculating $\langle n_r \rangle$ using:

[14] Applicable only to collectors with high surface reflectance.

$$\langle n_r \rangle = \frac{1}{\eta_{acc}} \frac{\Delta\eta_{op}}{\Delta\rho}\bigg|_{\rho\cong 1} = \frac{1}{\eta_{acc}} \frac{\eta_{op}(\rho_1 = 1) - \eta_{op}(\rho_2 = 1 - \Delta\rho)}{\Delta\rho} \text{ }, where\ \Delta\rho \ll 1$$

Equation 2.32 - Average number of reflections

Considering the above simplifications, flux concentration can be written in the following way for concentrators with high values of reflectance:

$$C_f \approx \eta_{acc} \cdot \rho^{\langle n_r \rangle} \cdot C_g$$

Equation 2.33 - Estimation of flux concentration

Chapter 3: Design

The primary objective of this chapter is to further discuss design considerations pertaining to Asymmetric CPCs, which previous works have not extensively addressed, thus creating a gap in knowledge. These include all forms of asymmetric θ_{in} /θ_{out} concentrators, and the use of Source-Acceptance Map Matching for ACPCs. In addition, this chapter builds upon these concepts to aid the design and development of the Seasonally Adaptive ACPC, a stationary concentrator that can maximize concentration throughout the year. By exploring these topics, this chapter aims to contribute to the existing understanding and further the advancement in the field of stationary solar concentrators.

3.1. Asymmetric Concentrators with Restricted Exit Angles (Asymmetric θ_{in} /θ_{out})

As seen in section 2.3.2, θ_{in}/θ_{out} concentrators, or transformers, can limit the angular extent of the rays emerging from the outlet of a concentrator, at the cost of a penalty on the maximum theoretical concentration (compared to non-θ_{in}/θ_{out} CPCs). Typically, the motivation for implementing this type of design (or modification on a concentrator) is to improve the absorption of radiation exiting the concentrator and/or prevent radiation leakage when contact between the concentrator and absorber is undesirable. Previous work has outlined the definition, theoretical background, and uses of this type of concentrator, with focus on symmetrical cases [11], [40], [42], [44]. Even though [42] recognized the possibility for implementing this concept with ACPCs and to obtain asymmetrical ray fans at the outlet, to the best of the author's knowledge, there has been no explicit description of these cases. Inspired by this realization, the present section focuses on the theoretical description and design limitations of θ_{in}/θ_{out} ACPCs and θ_{in}/θ_{out} concentrators with asymmetric exit angles.

3.1.1. θ_{in}/θ_{out} concentrator with Asymmetric Exit Angles

By following a procedure similar to the one described by [40], it is possible to create a θ_{in}/θ_{out} concentrator with an asymmetrical outlet ray fan. Consider the case of a concentrator with acceptance angle θ_{in}, and desired exit angles $\theta_{out,1}$ and $\theta_{out,2}$. Let *OO'* be the exit aperture, starting with $\theta_{out,1}$, consider two most extreme rays leaving the outlet at $\theta_{out,1}$ with the optical axis. Trace the two rays back so that they make one reflection before reaching the inlet of the concentrator, making an angle θ_{in} with the optical axis. The two reflections would then occur at points *O* and *R*, and the straight segment created between the two (*OR*) would form an angle φ with the optical axis. Then we trace all rays leaving *O'* at angles less than $\theta_{out,1}$ so they appear at the inlet aperture at θ_{in}, using a parabolic profile with a focus at *O'* and an axis parallel to the edge rays. The parabola would start at point *R*, tangent to the straight section, and finish at point *I*, where it meets the extreme ray passing through *O'* making an angle θ_{in} with the optical axis.

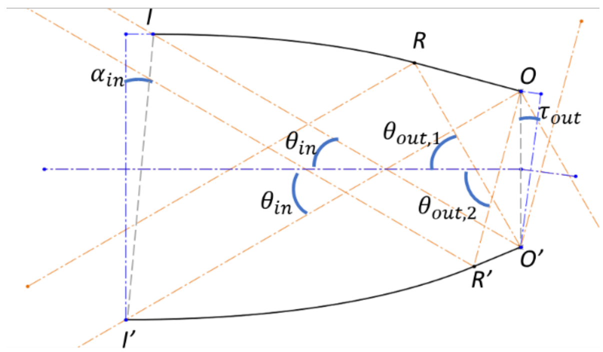

Figure 3.1 - θin/ θout concentrator with Asymmetric Exit Angles

$$\varphi = \frac{\theta_{out} - \theta_{in}}{2}$$

Equation 3.1 - Angle formed between straight segment and optical axis.

The same procedure is applied for the other side using $\theta_{out,2}$ as the reference angle. Note that this will result in an inlet and an outlet whose normal vectors form an angle with the bisector of the edge rays, defined as τ_{in} (Equation 2.20) and τ_{out} (Equation 3.3), respectively. Equation 2.21 describes the trigonometrical definition of the tilt angle of the inlet area from a horizontal plane of reference, α_{in}, with Equation 3.2 showing the same quantity defined only by the design angles for the case of a symmetric CPC with asymmetric exit angles. The relationship between α_{in} and τ_{in} can be seen in Equation 2.22.

$$\alpha_{in} = \tau_{in} = \tan^{-1}\left(\frac{\sin\theta_{out,1} - \sin\theta_{out,2}}{\tan\theta_{in}\left(\sin\theta_{out,1} + \sin\theta_{out,2}\right)}\right)$$

Equation 3.2 - α tilt for a CPC with asymmetric exit angles

$$\tau_{out} = \frac{\theta_{out,1} - \theta_{out,2}}{2}$$

Equation 3.3 - Tilt between vector normal to physical outlet area and bisector of the exit edge rays.

The maximum geometric concentration for this type of concentrator, doesn't follow Equation 2.17 because the inlet is no longer normal to the optical axis. The addition of a cosine term to consider the tilt from the bisector of the edge rays can help define the geometric concentration resulting from this concentrator, as seen in Equation 3.4.

$$C_g = \frac{\sin(\theta_{out})}{\sin(\theta_{in})} \frac{\cos(\tau_{out})}{\cos(\tau_{in})}$$

Equation 3.4 - Maximum Geometric Concentration Ratio

Following the expression developed by [13] (Equation 2.26), which expresses geometric concentration based on the inlet area and can describe C_g in a more general manner than Equation 2.11, its possible to write C_g for this kind of concentrator as seen in Equation 3.5.

$$C_g = n \; \frac{\sin\theta_{out,1} + \sin\theta_{out,2}}{\sin\beta_{max} - \sin\beta_{min}}$$

Equation 3.5 - Concentration Ratio for a θin/θout concentrator with asymmetric exit angles.

3.1.2. θ_{in}/θ_{out} Asymmetric CPC

A similar procedure is followed when creating an angle transformer on an ACPC with symmetrical exit angles, taking care of using the two different $\theta_{in,1}$ and $\theta_{in,2}$ that define the ACPC and the desired θ_{out}. Thanks to the symmetric ray fan at the outlet, there is no tilt in the bisector of the edge rays at the exit, yet the resulting straight segments are asymmetrical. Similar to a regular ACPC, the optical axis tilt (σ) is defined by Equation 2.19, but the α_{in} is not the same as the one for an ACPC with the same acceptance angles, as it changes with θ_{out}. Nevertheless, this quantity can still be calculated with Equation 2.21 but defining it based on the design angles results in a much more extensive equation. Regardless, the concentration is the same as defined in Equation 3.5, with β_{max} and β_{min} following Equation 2.22.

Consider a scenario where an ACPC with inlet acceptance angles of $\theta_{in,1}$ = 30° and $\theta_{in,2}$ = 80°, and a restriction on the exit angle of 80° is desired. In this scenario point R would merge with point *I*, creating only a straight profile defined by the design angles, and eliminating the parabolic shape. The point where θ_{out} surpasses θ_{in}, also marks the limit of this type of concentrator, since past this point the geometry no longer behaves as an ideal concentrator. Meaning that a θ_{in}/ θ_{out} concentrator can only be ideal if $\theta_{out} \geq \theta_{in}$.

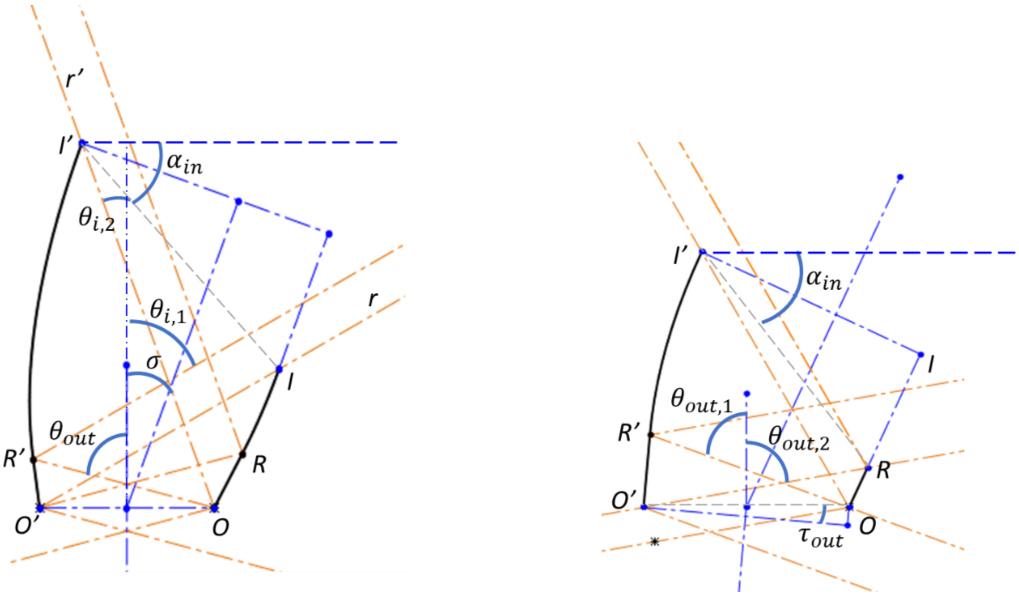

Figure 3.2 - a) ACPC with symmetric exit angles; b) ACPC with asymmetric exit angles

3.1.3. θ_{in}/θ_{out} Asymmetric CPC with Asymmetric Exit Angles

Following the last scenario presented above, it wouldn't be possible to limit the exit angle to 70°, due to the $\theta_{out} \geq \theta_{in}$ restriction. This is the exact scenario where a θ_{in}/θ_{out} ACPC with asymmetric exit angles would be useful to circumvent this design limitation, by imposing a larger exit angle onto the ACPC's right arm, while keeping θ_{out} = 70° for the left arm. With a procedure similar to the two cases shown above, this concentrator uses $\theta_{in,1}$ and $\theta_{in,2}$ to define the incoming edge rays, and $\theta_{out,1}$ and $\theta_{out,2}$ to define the limits of the outgoing rays. Since the concentrator is asymmetric at both the inlet and outlet, it has a tilt in the optical axis (σ), a tilt in the physical inlet (α_{in}) and a tilt in the bisector of the edge rays at the exit (τ_{out}). The tilt of the straight segments with the optical axis (φ) is still defined by Equation 3.1, the optical axis tilt by Equation 2.19, τ_{out} using Equation 3.3, and α_{in} can be calculated using Equation 2.21. Finally, Equation 3.5 can be used to calculate the maximum theoretical concentration ratio (C_g) of this design.

3.1.4. Performance

As briefly explained by [42], the θ_{in}/θ_{out} concentrator/transformer deviates from the ideal performance of the CPC by transmitting radiation outside of the θ_{in}, with this extra radiation leaving the concentrator at angles higher than θ_{out}. This can be attributed to the straight segments that form the θ_{in}/θ_{out} modification: rays that enter the concentrator at angles $\theta_{in}+\delta_{in}$ and reflect on the straight segment, will reach the outlet at $\theta_{out}+\delta_{in}$. This results in the acceptance function being higher than zero at θ_{in}, and as δ_{in} increases past this angle the acceptance function decreases linearly until reaching zero.

As can be seen in Equation 3.4 and Equation 3.5, maximum geometric concentration decreases with decreasing θ_{out}, following a sinusoidal curve. This means that for small decreases in θ_{out} (from 90°) it's possible to obtain significant improvements in absorptance with small decreases in concentration. For example, limiting θ_{out} to 70°, can lead to a reduction of only 6%.

3.2. Source – Acceptance Map Matching for ACPCs

As explained in section 2.6. , Source-Acceptance Map matching is a useful tool for designing concentrators for any given application. When designing a stationary concentrator for high latitudes, such as Toronto (43.77°), the source map would be asymmetric across the unit circle in cosine space, as explained in section 2.6. , which can be seen in Figure 3.3a. Following the Source-Acceptance Map matching procedure, we can attempt to design a stationary concentrator by plotting the acceptance map and verifying how well it matches the source map seen in Figure 3.3. To perform this procedure, first it is necessary to define a daily period of operation (or operation time) for the concentrator, which will in turn guide the selection of the acceptance angles and evaluation of the acceptance map. An appropriate time of operation could be 6hrs a day since it is the minimum hours of daylight available in any day of the year. Minimizing the hours of operation also improves the concentration as seen in section 2.4. , further supporting the selection of 6hrs of operation. For Toronto, this would result in operating between 9am and 3pm in the winter, and 10am until 4pm in the summer.

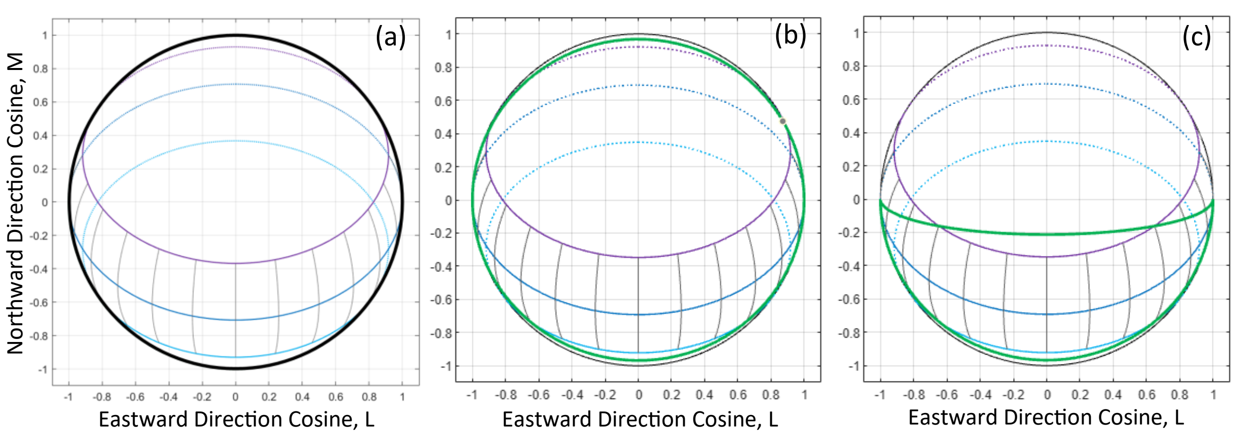

Figure 3.3 - Direction Cosine (L-M) Space plots of the source map and acceptance maps. a) Source Map for Toronto, Canada (43.77° of Latitude), b) Acceptance Map for a 75.5° CPC, c) Acceptance Map for both a 43.77° CPC and a β_{max} = 75.3, and β_{min} = 12.3 ACPC

Now that the operation time for the concentrator is known, it's possible to start plotting acceptance maps for different concentrator designs and determining the acceptance angles and resulting concentration. To find an appropriate concentrator design, it would be of interest to start with a CPC, similar to the work performed by [28]. The acceptance map for a CPC trough, is defined as an ellipse with a formula seen in Equation 2.28, which states that for a ray to be accepted its projected angle in the symmetry plane (L-N plane) must be ≤ θ_{in} [28], [29]. The acceptance angle required to meet the operating time would need to be at least 75.5°, resulting in a $C_{g,max}$ of 1.03×. This is very low compared to the maximum concentration calculated in section 2.2.1, and the gap can be attributed to the waisted acceptance map. This means that there is a large angular range where the concentrator would accept radiation, without the Sun occupying the same range, seen on the top half of the acceptance map in Figure 3.3b.

There are two possible avenues to circumvent this problem: tilt the CPC or design an ACPC. The first option would require a tilt equal to the latitude of the location of operation (σ = 43.77°), and to implement an angle rotator to connect the CPC back into the horizontal plane[28]. The acceptance map resulting from tilting the CPC would be formed by two half-ellipses with semi-minor axes equal to sin(θ_{in} - σ) and sin(θ_{in} + σ), defined by Equation 3.6 [14], [29]. Solving these equations using the source map and the hours of operation would result in the acceptance map seen Figure 3.3c, which has a θ_{in} ~32°, and a concentration of ~1.9×. This level of concentration is much closer to the fundamental limit and can be used for medium temperature applications.

$$L^2 + \frac{M^2}{\sin^2(\theta_{in} - \sigma)} \leq 1 \; for \; M \geq 0$$

$$L^2 + \frac{M^2}{\sin^2(\theta_{in} + \sigma)} \leq 1 \; for \; M \leq 0$$

Equation 3.6 - Cosine Space Definition of a tilted CPC's Acceptance map

Similarly, designing an ACPC for the source map in Figure 3.3 would result in an acceptance map composed of two half-ellipses with semi-minor axes equal to sin(β_{max}) and sin(β_{min}) [14]. The resulting acceptance map can be seen in Figure 3.3c, with design angles β_{max} = 75.3, and β_{min} = 12.3, and $C_{g,max}$ of ~3.2x.

$$L^2 + \frac{M^2}{\sin^2(\beta_{max})} \leq 1 \; for \; M \geq 0$$

$$L^2 + \frac{M^2}{\sin^2(\beta_{min})} \leq 1 \; for \; M \leq 0$$

Equation 3.7 - Cosine Space Definition of a ACPC's acceptance map[15]

As seen in Figure 3.3c, these two designs show equal acceptance maps, with an upper half-ellipse that folds on itself creating a crescent shape that allows it to match the source map. When comparing the two designs it is clear that the ACPC does a better job in concentrating, with a $C_{g,max}$ ~1.6 times the tilted CPC's. When evaluating these designs, there are a few more points to consider, namely material use, dimensions, and flux concentration. For comparison purposes, the two designs will be considered to have a 1m outlet and dimensions will be given in a per-meter-of-depth basis. Starting with material use, the tilted CPC is made up from two reflective surfaces of ~2.67m, and an angle rotator measuring ~0.76m in length, for a total of 6.1m. On the other hand, the ACPC is composed of two different reflective sheets measuring 4.14m and 0.56m, for a total of 4.7m. This indicates that the ACPC requires less material than even the case when the tilted CPC doesn't make use of the angle rotator. In terms of dimensions, the CPC measures 2.6m in height and 2m in width but when tilted and using the ground as frame of reference, it occupies 2.91m in height and 2.88m in width, with the angle rotator adding an extra 0.28m. On the other hand, the ACPC measures 3.47m in height and 1.83m in width, making it overall larger. Regardless, the benefits presented by the ACPC makes it a more promising design.

Even though Source - Acceptance Map matching is a very useful tool in the design of stationary ACPCs and concentrators in general, there are some factors to consider when implementing this procedure. The main issue has to do with impractical geometries that might result from strictly following the results obtained from solving the ellipse equations for the acceptance map of an ACPC (Equation 3.7). Doing so will result in the maximum geometric concentration possible for the latitude and time of operation of interest but can result in extreme geometries. Figure 3.4 demonstrates the $C_{g,max}$ and height resulting from solving Equation 3.7 for every possible latitude for a period of operation of 6hrs (when 6hrs of sun are available). As the latitude approaches 90° the $C_{g,max}$ increases significantly, but so does the height of the concentrator. This means that to design practical ACPCs for extremely high latitudes, its useful to consider design angles wider than the ones obtained by the procedure demonstrated in this section. Finally, it is useful to note

[15] Note that the inequality in the condition for the first equation ($M \geq 0$) changes directions when $\beta_{max} > 0$.

that the ratio of $C_{g,max}$ to height becomes greater than 1 only at ~51° of latitude, and that there is a local maximum in the concentrator height at ~41° of latitude.

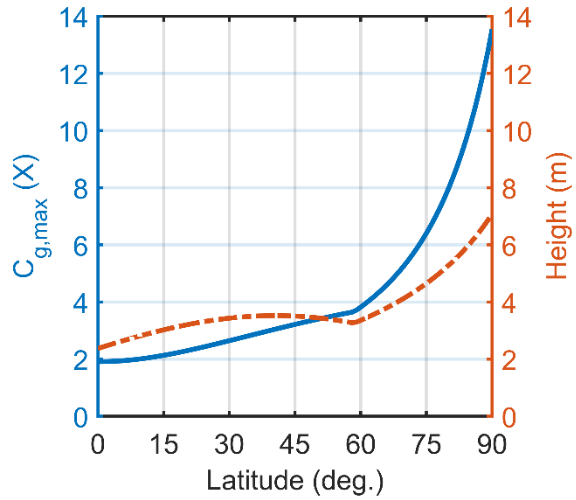

Figure 3.4 - Maximum geometric concentration ratio and height for ACPC designed for various latitudes.

3.3. Seasonally Adaptive ACPC

As seen in the previous section, an ACPC designed for a given high-latitude source map and hours of operation can reach higher $C_{g,max}$ than a tilted CPC, while using less material. Nonetheless, calculating the flux concentration that these two designs can achieve through the year draws a different conclusion. Figure 3.5 shows that the tilted CPC reaches its $C_{g,max}$ twice in a year, and portrays concentrations above 1x for the operation time desired. On the other hand, the ACPC falls short of its promising $C_{g,max}$, reaching ~2.7x, and achieves little to no concentration around the summer solstice. This situation is caused by the variation of the projection of inlet area onto the solar vector as the Sun moves between the winter and summer solstice visualized on Figure 3.6a. The largest projection occurs during the winter solstice, where it reaches ~2.7x at noon, and the smallest occurs during the summer solstice, as low as ~0.15x at the edges of the operation time and ~0.64x at noon.

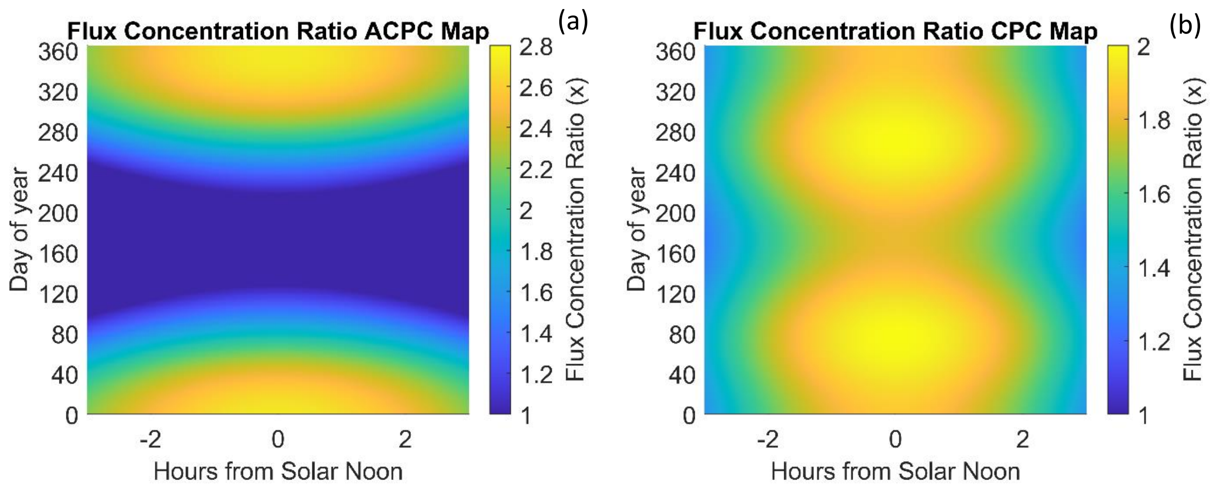

Figure 3.5 - Yearly Flux Concentration Ratio for a) ACPC and b) Tilted CPC

A possible way to improve the performance in the middle of the year is to use a flat mirror extension attached to the end of the parabolic profiles to tilt the inlet area and improve concentration in the summer, as seen in Figure 3.6b. Said extension has to be parallel to the optical axis of the ACPC to not alter the angle of the edge rays and keep the same acceptance map. The effect this has on the concentration can be shown by observing the definition of flux concentration, where ϑ is the angle between the solar vector and the inlet area's normal vector. Without any tilt, the flux concentration ratio could be defined as:

$$C_f = C_g \cos\vartheta = \frac{A_i}{A_o}\cos\vartheta$$

Equation 3.8 - Flux concentration with incidence modifier

But by tilting the inlet by τ, the incidence angle changes by -τ, and the new inlet area (A_m) measures $A_i cos(\tau)$. Resulting in the following:

$$C_f = \frac{A_m}{A_o}\cos(\vartheta-\tau) = \frac{A_i}{A_o\cos\tau}\cos(\vartheta-\tau) = C_g\frac{\cos(\vartheta-\tau)}{\cos\tau}$$

Equation 3.9 - Effect of using an extension on flux concentration.

Which can also be written in the same format as Equation 3.5, where the tilt τ would be included within the terms β_{min} and β_{max}.

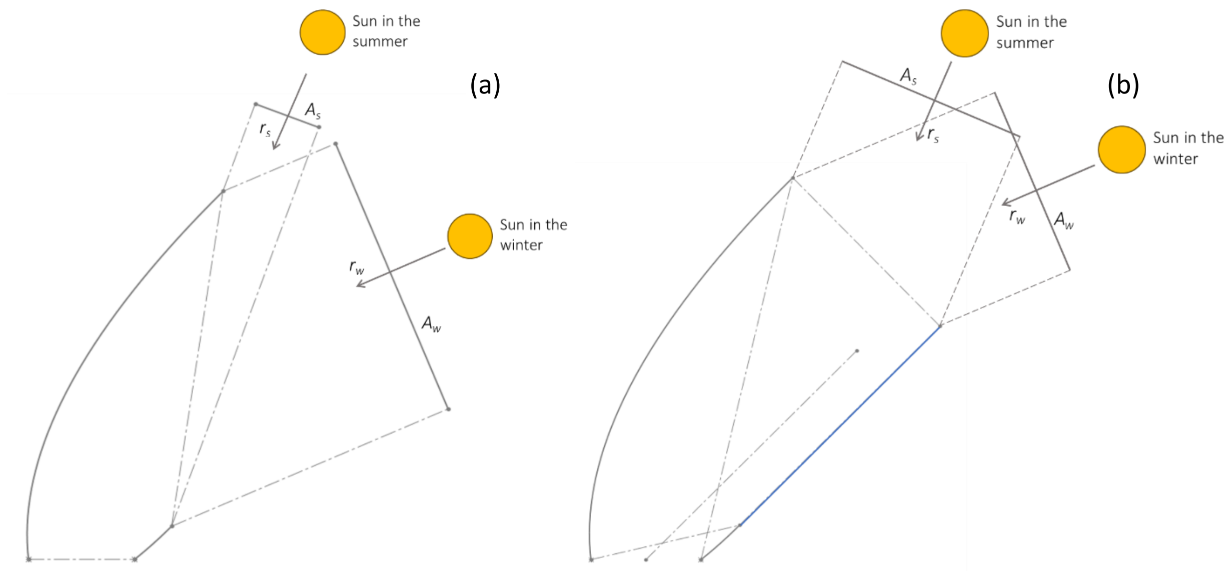

Figure 3.6 - Projected areas for an ACPC and a ACPC with a tilted aperture

Considering the cosine terms in the last equation, the introduction of τ has the effect of reducing the incidence angle for the summer-time, but this automatically increases it for the winter-time. This in turn enlarges the projected inlet area during the summer but reduces it in the winter, reducing concentration for this period of the year (Figure 3.6b). To mitigate this issue, a novel design concept called *Seasonally Adaptive ACPC* was ideated by Cooper, T. (2021) to maximize concentration in both halves of the year. This design implements an extension between the spring and fall equinoxes (summer) and removed it between the fall and spring equinoxes (winter) [29].

The Seasonally Adaptive ACPC is a simple, yet useful alternative concentrator design composed of an ACPC and a flat mirror extension that can tilt the aperture area to improve flux concentration for the summer term. The base ACPC must accept radiation through the year at the location where it is designed to be implemented, making it perform exceptionally well for the winter-time as seen above. The flat mirror extension is then designed to be parallel to the optical axis and attach to the shorter parabolic profile, improving summer-time concentration. The extension can be designed to create the aperture area to a size of interest, taking into consideration of the material use associated with it[16]. As stated before, this extension is meant to be engaged for the summer-time and disengaged for the winter-time, from here on called *summer configuration*, and *winter configuration*, respectively. This shift in configurations

[16] Increasing the extension size can increase the size of the inlet area almost indefinitely, taking into consideration than there is a maximum useful extension length.

constitutes a pseudo-tracking system that only comes into play twice a year, which would require less maintenance than a more complicated tracking system.

3.3.1. Performance

The acceptance map of the Seasonally Adaptive ACPC, would follow the same definition as the one for a regular ACPC (Equation 3.7). On the other hand, the resulting flux concentration would change drastically between the summer and winter configurations as seen in Figure 3.7. The concentrator design used for figure utilizes a flat mirror extension with a length of ~4.48m, which results in a horizontal inlet aperture. The winter configuration would have the same peak concentration as seen above, ~2.7x, and the summer one would have a peak concentration of ~2.5x. By considering the two configurations simultaneously, it is possible to find the minimum noon (daily peak) concentration at ~1.9x, and the overall minimum concentration at ~1.3x, both happening at the equinoxes (Figure 3.7b). The biasing effect that using the flat mirror extension has on the performance of the design is better represented in Figure 3.7a, where the minimum concentration of each configuration can be seen drastically lower than the total performance of the system. Variation in the orientation of the inlet would cause changes in the flux concentration profile seen on Figure 3.7a. For the summer configuration, further tilting the inlet aperture upwards would increase the maximum concentration and generate a sharper flux concentration profile. On the other hand, tilting it down to make an inlet normal to the optical axis (as the one seen in Figure 3.6b) would follow a flux concentration profile similar to the CPC's (Figure 3.5b), with two peaks occurring at the equinoxes and the lowest concentration occurring at the solstice.

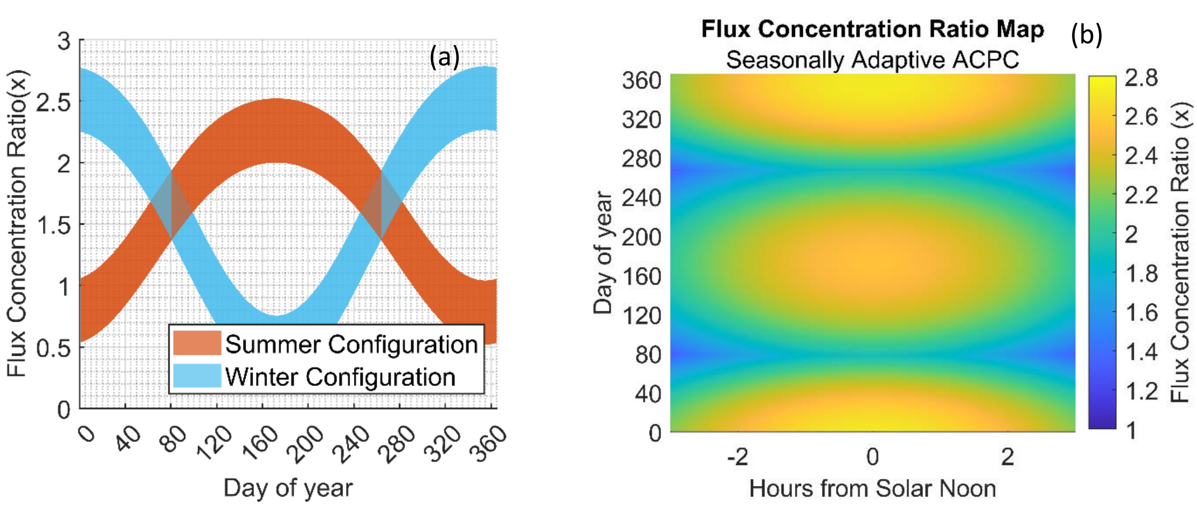

Figure 3.7 - Flux Concentration for Winter and Summer Configuration for a Seasonally Adaptive ACPC with β_{min}=21.75 and β_{max}=85.21 & a horizontal summer inlet

The concentration plots shown above focus on the effect that the direct irradiance's angle of incidence has on the flux concentration. But the performance of a concentrator can also be described using the output radiative flux. Following the definition of flux concentration C_f, its possible to obtain a simple model to describe the irradiance reaching the outlet of a concentrator, as seen in Equation 3.10. Where η_{op} is the optical efficiency for direct irradiance, which can be estimated using numerical analysis, and H_i is the beam irradiance, or $H_N cos\vartheta$ for stationary concentrators, which can be measured or estimated using representative data.

$$H_o = C_f \cdot H_i = \eta_{op} \cdot C_g \cdot H_i$$

Equation 3.10 - Simple model of output flux

This model only accounts for the direct irradiance, which is often considered to be enough for systems that have a large $C_{g,max}$, or small acceptance angles, because the accepted H_d is quite small (see section 2.2.4). But for stationary concentrators, which have relatively small $C_{g,max}$, the accepted H_d can be quite significant. The same can be said about reflected irradiance, which can become significant for concentrators with a tilted inlet and with the ground located within their acceptance range, like the winter configuration shown above. The acceptance efficiency and optical losses of these types of irradiances can be quantified using a dedicated optical efficiency for each. Considering this, a model that can more accurately describe the irradiance reaching the outlet of the concentrator can be developed, based on the geometric concentration, optical efficiency, and incoming irradiance (Equation 3.11).

$$H_o = C_g \left(\eta_{op,N} \cdot H_N \cdot \cos \vartheta + \eta_{op,d} \cdot H_d + \eta_{op,r} \cdot H_r \right)$$

Equation 3.11 - Model for the output radiative flux

Where $\eta_{op,N}$ is the optical efficiency for direct irradiance, $\eta_{op,d}$ is the optical efficiency for diffuse irradiance coming from the sky hemisphere and $\eta_{op,r}$ is the optical efficiency for the reflected irradiance. All of which are equal to acceptance efficiency (η_{acc}) times reflectance to the power of number of reflections ($\rho^{\langle n_r \rangle}$), following Equation 2.31. If diffuse and reflected irradiances are assumed to follow an isotropic distribution, $\eta_{op,d}$ and $\eta_{op,r}$ can be considered to be independent of the incidence angle ϑ, leaving only $\eta_{op,N}$ as a function of ϑ. Following this assumption, H_r would be considered to be diffuse and could be expressed as H_G times the ground albedo (ρ_a). All acceptance efficiencies and number of reflections can be estimated using numerical analysis, whereas the ground albedo can be estimated based on the surrounding surfaces, and the irradiance values can be measured or estimated using representative data.

3.3.2. Implementations

The use of the Seasonally Adaptive ACPC design is most beneficial for instances when tracking is not financially or physically viable. This is the case for absorbers or systems that depend on a specific orientation to function, such as solar desalination devices, absorber on rooftops and walls, etc. Based on the concentrating capabilities demonstrated in this section and the remarks made in section 2.4. , this concentrator design is capable to work for low to medium temperature applications up to 240°C, following Equation 2.16. Further design characteristics include the possibility to implement the flat mirror extension as a method of protecting the mirror surfaces from the elements by rotating it onto the entrance aperture. Likewise, this capability could help hold the absorber temperature for longer after the daily end of operation. However, closing the extension daily could require a more advanced mechanism than otherwise needed for the standard operation described above.

Due to the nature of the ACPC design and the process of Source-Acceptance Map Matching, changing the latitude of implementation has a direct effect on the maximum concentration of the Seasonally Adaptive ACPC as is the case for ACPCs (Figure 3.4). Using the method introduced on section 3.2. to design a Seasonally Adaptive ACPC for high latitude cities, results in the designs outline on Table 3.1.

Table 3.1 - Seasonally Adaptive ACPC designs with maximum possible geometric concentration for various high-latitude cities.

City	Latitude	β_{max}	β_{min}	$C_{g,max}$	Height(m)[17]
Svalbard, Norway	78°	70.5°	-46.5°	~7.3x	5.00
Helsinki, Finland	60°	89.6°	-29.6°	~4x	3.52
Edmonton, Canada	53.6°	88.6°	-25.6°	~3.6x	3.40
London, UK	51°	87.6°	-24.5°	~3.4x	3.43
Seattle, USA	48°	86.4°	-23.3°	~3.3x	3.48
New York, USA	41°	82.3°	-19.9°	~3.1x	3.52
Montevideo, Uruguay	-35°	79.9°	-16.1°	~2.8x	3.50

[17] Based on a concentrator outlet measuring 1 meter of length

3.4. Prototyping the Seasonally Adaptive ACPC

3.4.1. Design

The design introduced in the previous section constitutes the highest concentration possible for the Seasonal Adaptive ACPC's winter configuration designed for 6hrs of operation and a latitude of 43.77° (Toronto's Latitude). Even though this is the highest concentration for this use case, designs that are less constricted to the latitude and operating time requirements can occupy a smaller footprint while still achieving significant concentration. Consider an ACPC with design angles $\theta_{in,1}$=0° and $\theta_{in,2}$=90°, with a vertical inlet this concentrator has a $C_{g,max}$ of 2x, and a total height 2 times the concentrator outlet. The acceptance map of this design occupies the lower portion of the hemisphere in cosine space, meaning that it can accept radiation coming from anywhere in the southern half of the sky. Thanks to these properties, this design could be used for at least 3 hrs of operation anywhere with a latitude higher than ~31° North (or South), while maintaining a footprint significantly more compact than any of the designs obtained from strictly following the methodology seen in section 3.2. , and the ones discussed on section 3.3. . The compact proportions of this design also translate into less material use as the length of the mirror required for this ACPC is only 2.3 times the outlet, more than a 2x reduction in material. This also applies to the flat mirror extension, which only requires a length of ~2.84 times the outlet to obtain a horizontal inlet, a more than 1.5x reduction. Based on this rationale, it was determined that the prototype used for testing the performance of the Seasonally Adaptive ACPC would follow the 0°-90° design, even though it means a 1.6x reduction of $C_{g,max}$[18].

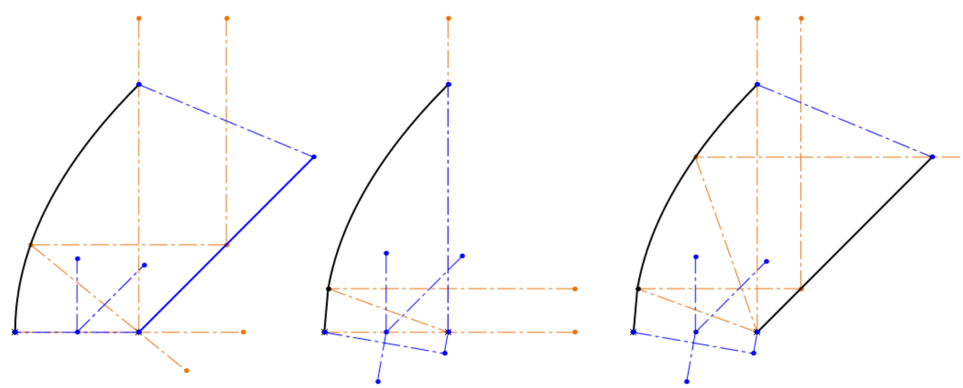

Figure 3.8 - Seasonally Adaptive ACPC with θ_1 = 0° & θ_2 =90°. a) With a θ_{out} = 90°, the extension is represented in blue. b) Winter Configuration with θ_{out} = 80°, c) Summer Configuration with θ_{out} = 80°.

[18] All references of reduction of size, material use or concentration made in this paragraph are compared to the design discussed in section 3.3. , with $\theta_{i,1}$=-12.5° and $\theta_{i,2}$=75.5°

For the prototype design, a horizontal inlet area results in a maximum summer aperture ratio equal to $C_{g,max}$, whereas the maximum extension length before loosing rays is equal to 3.23 times the outlet. However, attempting to implement the closing capabilities of the concentrator with these extension lengths would result in the flat mirror being exposed on the top of the concentrator. To avoid this issue, it was decided to reduce the extension length to match the size of the concentrator inlet (2 times the outlet), reducing the maximum summer concentration 1.53× (Figure 3.8).

The prototype was designed for outdoor operation and to concentrate onto an existing solar desalination device, with an absorber measuring 18in-by-18in (2.25sqft.). Based on this purpose, it was decided to design a 17in-by-17in (2sqft.) square outlet, ensuring most radiation exiting the concentrator would reach the absorber. Together with this design, a second prototype downscaled to a 6in-by-6in (0.25sqft.) outlet was also considered, to test the manufacturing and construction process, and allow for in-lab experiments. The operation and performance described in the previous section considers a two-dimensional concentrator, which is equivalent to an infinitely long trough, a common assumption when studying CPC troughs. This assumption neglects radiation that might enter the concentrator inlet area and land outside of the absorber. Because of the outlet geometry proposed, this assumption wouldn't hold for this design. To approach the performance of the two-dimensional concentrator it was decided to implement reflective side walls, which would allow it to perform like an infinitely long trough. Reflective side walls do this by redirecting radiation that entered the concentrator inlet area but would have missed the outlet if these walls weren't present.

To avoid a thermal short between the concentrator and the solar desalination device's absorber, the Seasonally Adaptive ACPC prototype was decided to be built implementing a θ_{out} restriction. This allows for a separation between the concentrator's outlet and the absorber without loss of radiation, as highlighted in sections 2.3.2 & 3.1. . Nevertheless, the lack of a right parabolic profile forces the design to be unable to have a θ_{out} restriction on the right side, and therefore obtain an asymmetric exit ray fan. With that consideration, the left parabola was designed to have a $\theta_{out,1}$ of 70°, for a total θ_{out} of 80°, resulting in a ~1.5% reduction in concentration ratio, for a total of ~1.94×. The final dimensions of the θ_1 = 0° and θ_2 =90° prototype design, were, for a 1-unit outlet, a winter inlet area and height of ~1.94 units, a summer inlet area of ~1.53 units, a flat mirror extension measuring ~1.94 units, a footprint of ~2.41 units, and a parabola length of 2.3 units.

3.4.2. Theoretical Performance

With a $C_{g,max}$ of 1.94×, and an inlet orientation of 22.5° in the summer and 90° in the winter, when implemented in Toronto, this concentrator reaches a maximum concentration of 1.78× in the winter and 1.48× in the summer. Like the design shown in section 3.3, the design reaches its minimum noon concentration, of 1.37×, on each of the equinoxes. On these same dates, the concentrator reaches its overall minimum concentration at the end of its operation time, 0.97×, though this is not he only instance of concentration reaching lower than 1×. Around these dates, for a total of 10 days twice a year, concentration becomes lower than 1× at the end of the operation time, but occurs no more than 6 minutes from the end (or beginning) of the operation time (Figure 3.9b). Due to the orientation of the inlet aperture, the summer configuration curve on Figure 3.9a doesn't follow the same profile as Figure 3.7a, this of course is related to the effect of incidence angle. The seemingly flat profile resulting from this, has two peaks of concentration occurring on the 147^{th} and 197^{th} days of the year (May 27^{th} and July 16^{th}, respectively). Nevertheless, the design has a range of 131 days where the concentration stays within 2% (>1.456x) of the summer configuration's maximum, making the summer operation relatively constant.

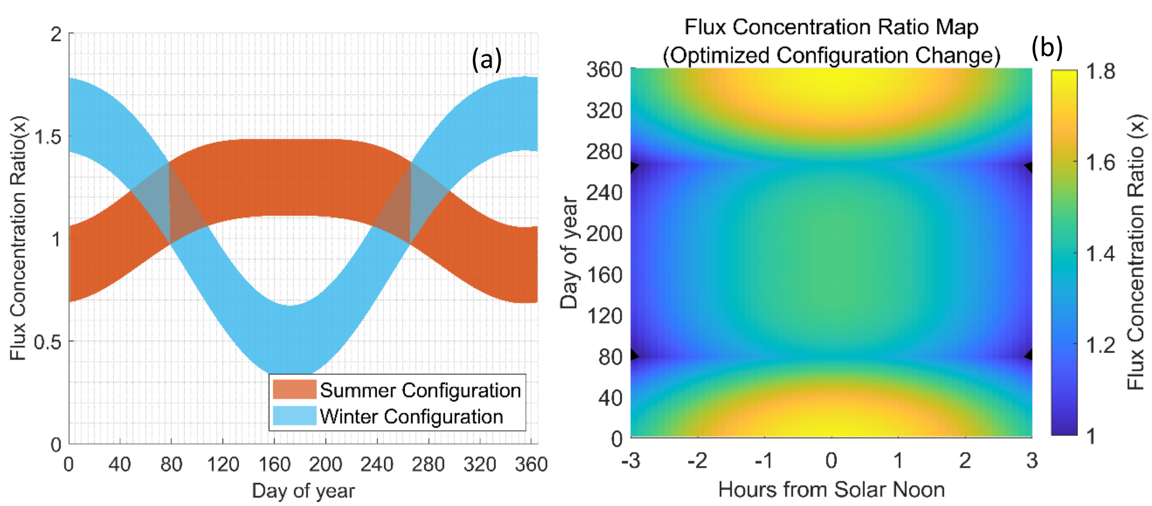

Figure 3.9 - Flux Concentration Winter and Summer Configurations for the Seasonally Adaptive ACPC Prototype (β_{min}= 0° and β_{max}=90°) & a summer inlet tilted 22.5° from the horizontal, when used at a latitude of 43.77°.

3.4.3. Construction

The Seasonally Adaptive ACPC design shown above was scaled to construct a prototype and use it for experimental procedures. The design and construction of the concentrator was developed in-house, with an emphasis on prototyping flexibility and weightlessness. The structural components of the design were selected to be 1 inch T-slot aluminum extrusion framing for ease of construction and flexibility. These were obtained in generic sizes, except for the ones used for the reflector control points. The chosen reflector material was a 0.5mm aluminum sheet with an oxide reflective coating applied via physical vapour deposition, and a reported minimum specular reflection of 90% (Anolux Miro IV). The reflector material was cut to size and shape using a water-jet cutter, this manufacturing decision was made based on the manufacturing tools available. This was found to bring a series of problems to the sheet metal, with water damage being the most prominent one. The reflective sheets were bonded to structural components, where necessary, using a two-part epoxy specifically formulated for metal bonding. Here bonding was chosen over fastening or welding, since it doesn't involve any from of fastener that can obstruct the reflector surface nor cause thermal damage to the reflector coating, as welding would.

The design was developed using a CAD software, where all the concentrator components were modeled, along with the structural components. The resulting design was composed of two parts, an aluminum frame to mount the reflective sheets, and a base frame to place the solar desalination device under the concentrator (only built for the 17in prototype). To simplify construction, the prototype wasn't designed to utilize the concept of a shift in the front wall. Instead, the front wall was made to be installed in place when needed using fasteners, which would physically lock it in the correct position. The top aluminum frame was the main structure to form the concentrator and parabolic profile, the following section goes in further detail into how this was accomplished.

3.4.3.1. Constructing the Parabolic Profile

During the ideation process, an innovative method to create the parabolic profile was developed with reconfigurability in mind. By supporting the parabola from only two points and controlling the location and tilt angle of the profile at these locations, it was possible to form the parabolic profile accurately without relying on a solid backing, commonly used in CPC designs. In this design concept, the control points of the parabola are to be the two most extreme points in the profile (i.e., the top and bottom edges of the parabola), so it allows for full control over the parabolic shape. This allows to shape the reflective sheet into various parabolic profiles (including truncated ones), without the need for any further manufacturing, making it especially useful for prototyping, researching and iterating designs. It must be noted that modifying the parabolic profile for a reflective sheet with a given size requires the inlet and outlet to be scaled appropriately. For example, if it is desired to study two CPCs with 30° and 45° acceptance angle, by starting from the 30° one with a 1m outlet, the reflective sheet would have to be cut to ~2.67m. But this same reflective sheet dimensions would form a ~2.17m outlet for the 45° CPC. Alternatively, a given reflective sheet size can be used for a truncated CPC, if the outlet shape is a critical design aspect.

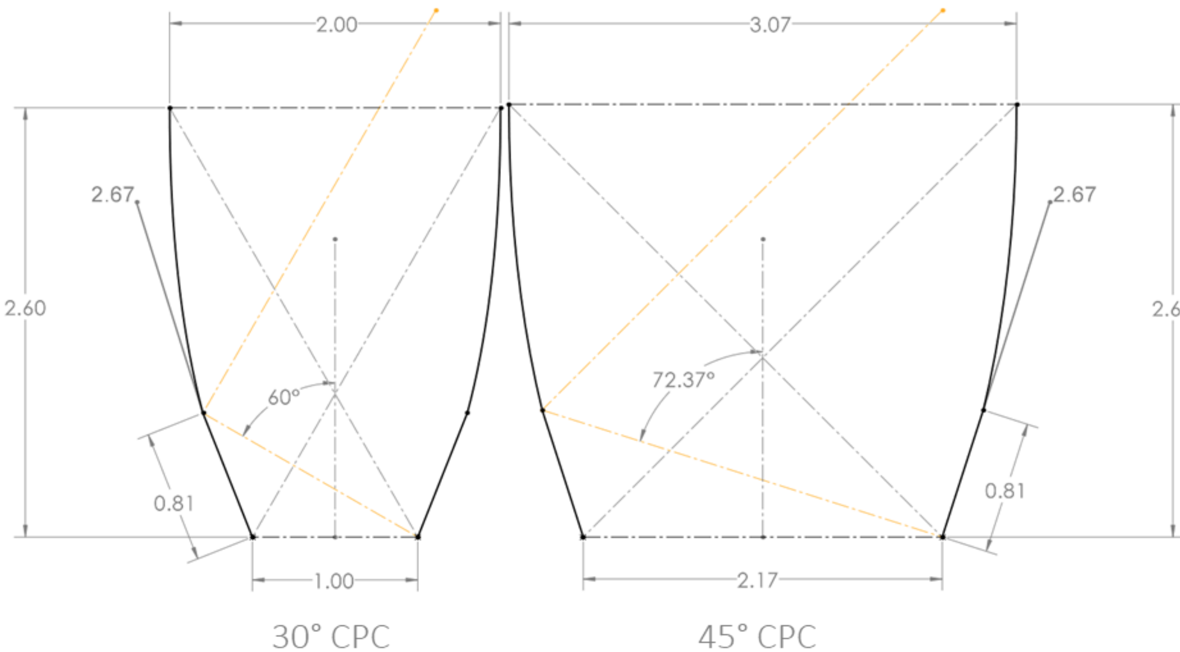

Figure 3.10 - Example case of forming a 45° CPC from a pre-set 30° CPC's reflective sheets.

When designing θ_{out} CPCs, such as the design described in previous sections, the lower control point of the parabola has to be placed at the meeting point between the parabola profile and the straight section. This ensures tangency between the two sections and precise control of the parabolic profile. The positioning of the control point away from the lower edge of the concentrator is especially beneficial for avoiding bulky elements near the outlet and receiver, allowing for the outlet to be closer to the receiver without risking thermal shorts. It is important to note that implementing θ_{out} modifications to this construction method limits its flexibility to iterate between designs. This is because by setting the control point at some given distance from the outlet edge, causes the subsequent iterations to have a pre-set restriction in the exit angle. For example, for the same case given above, if the 30° CPC is designed with an exit angle of 60° (resulting in a straight section measuring ~0.81m), the resulting 45° CPC would have an exit angle of ~72.37°.

After cutting the reflector material to size, a pair of aluminum extrusions with the same width as the reflector were bonded at the top of the parabola and the highest position within the θ_{out} straight section. The position where the extrusions were bonded can be seen in the Figure 3.11. As stated above, this construction method works by setting the position and tilt of two control points in the parabola. With the epoxy fully cured, the control extrusions were mounted on an aluminum framing, setting the distance between the two control points. After which, the tilt of the extrusions was set by measuring the angle between the control extrusions and vertical components in the framing. The tilt angle of the higher control point was 44.6°, and 10° for the lower control point.

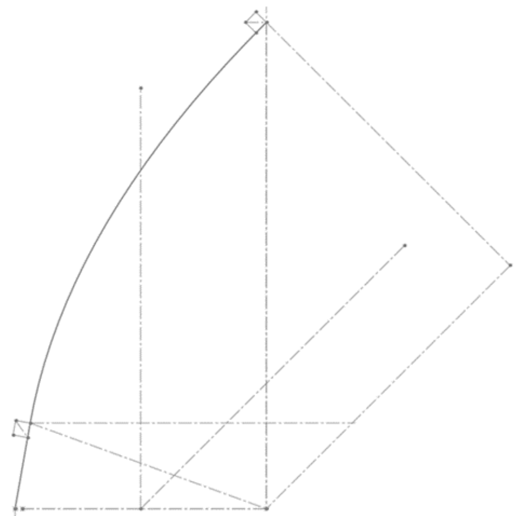

Figure 3.11 - Outline of parabola profile with location of aluminum extrusions

This parabolic profile construction method depends on the yield strength and modulus of elasticity of the mirror material. The ratio of these (yield strain) must be high enough to allow for the necessary strain to be within the elastic behaviour of the material. Similarly, the elastic modulus must be high enough to maintain enough tension in the material to prevent it from folding on itself and maintain the shape. For the right range of values, the parabolic profile can be shaped without the need for forming, bending or other permanent manufacturing processes that might cause deviations from the smooth mirror shape. This method was ideated with prototyping and researching in mind, since it allows for different parabolic profiles to be created without the need for further manufacturing, saving money and time. Even though the usefulness of this method for more robust applications is yet to be analyzed, its lightweight and limited material use makes it a promising method for manufacturing CPCs.

Chapter 4: Methodology

4.1. Monte Carlo Ray Tracing Simulations

The numerical studies performed had the objective of validating the theory behind the workings and performance of the Seasonal ACPC, along with expanding the understanding of said concept. Numerical analysis allows for testing physical situations without the need for physical testing and can help researchers come up with numerous data points that might be hard to obtain using traditional experimental methods. But for numerical solutions to be trusted, they have to be validated with experimental results, to make sure the numerical scenario is an accurate representation the physical system. That being said, for a given geometry, Monte Carlo Ray Tracing methods are able to accurately estimate the radiative behaviour of a system by averaging the path of a random finite sample of rays, or energy packets. This method is stochastic in nature, because all points in a ray's path (emission point and direction, and interaction) are determined randomly [45].

The numerical analyses cases included the development of the transmission angle curve for the Seasonally Adaptive ACPC, and scenarios that reproduced the flux mapping experiments' conditions (described in 4.2.1). All numerical analyses were performed using Monte Carlo Ray Tracing (MCRT) codes, which were set up by defining the geometry introduced in Chapter 3: in Matlab and using VeGaS+ software (version 19.1) to solve the ray tracing problem. The simulation cases that aimed to reproduce the experimental conditions considered scenarios with only DNI incident on the concentrator, and scenarios with only diffuse horizontal irradiance. The transmission angle curve allowed to determine how close is the concentrator to the ideal performance. The DNI based simulations allowed for the calculation of the radiative flux output, average number of reflections and the efficiency of the concentrator. And the ones that focus on DHI offered insight into the acceptance and output of diffuse radiation. All simulations performed neglected the wavelength of the rays, and only considered surface exchange. The following sections include a more detailed insight into the setup of the numerical validation cases.

All simulation cases utilized the same basic geometry for the concentrator model which directed its inlet towards the -*Y* direction and scaled the design to have an outlet with a width and depth of 1 unit of length, making the total height of the concentrator equal to 1.9397 units. Following the concentrator design ratios, the resulting inlet area for the Summer Configuration had a length of 1.4846 by 1 unit of width, and the Winter Configuration's inlet was 1.9397 units by 1 unit. A parabolic surface with 1 unit of width was created to extend from z = 0.3420 to 1.9397 with a foot located at (0.5, -0.4699, 0). The lower edge of the parabola was intercepted by a flat surface, oriented 10 degrees from the vertical, and extending towards the outlet surface; this acted as the θ_{out} portion of the concentrator. The concentrator was bounded on either side by one square surface extending from the outlet to the top of the parabola and a triangular surface with sides meeting the winter inlet surface, summer inlet surface and summer extension.

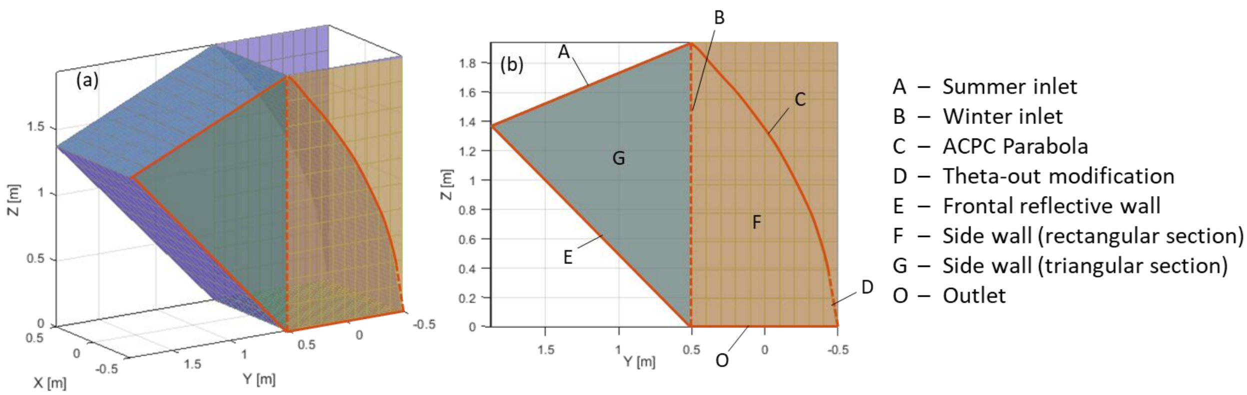

Figure 4.1 - Geometrical definition of the concentrator prototype used for numerical simulations. a) Isometric view; b) Side view, with surfaces labeled for reference.

The overall geometry can be seen in Figure 4.1. The source's target changed between the summer and winter configuration, with the summer configuration using surface A, and the winter one using surface B. These two surfaces were also considered to be the inlet surfaces for each case, with all cases having the outlet as surface O with an absorptance of 100%. On the other hand, all other surfaces C to G were set to have the same reflectance (e.g., 100%). The summer cases implemented the front wall (surface E), whereas the winter case removed this wall, imitating the experimental scenario. The following sections include more detailed insight into the setup of the numerical validation cases.

4.1.1. Transmission Angle Curve

As stated previously, the objective of this numerical analysis is to measure the ratio of flux reaching the absorber to flux entering the inlet area to determine the Acceptance Function, $F(\vartheta)$. The simulations defined for this analysis used the geometry described above and a ray source that shot radiation at every angle starting from 0° until 100° from the horizontal. The source was defined as a uniformly emitting disk near infinity with an angular variation of 0°. Following software's definition of a source, a surface had to be defined as a target, where the generated rays were to intercept. This helps define the starting point, or location, of the sun vector and delimits the extent of area that the rays will be present. The target is set as a "counter surface", which allows the software to count the number of rays that cross it, without influencing the rays' path. For this simulation, only the summer configuration was used, which defines the target surface as the summer configuration's inlet (surface B).

4.1.2. Direct Normal Irradiance

The input for these simulation cases included the geometry of the concentrator highlighted above, and the 3 components of the sun vector in cosine space (L, M, N) defined by the day of the year and time of day. The ray source was defined to be a uniform emitting disk near infinity, with an angle range equal to half the sun's angle (4.65e-3 rad) at either side of the defined sun vector and an output power of 1000 units of power. The simulation cases covered by this numerical analysis followed the dates of the experimental procedures seen in section 4.2. (Table 4.1) to define the configuration used and the direction of the sun vector. All simulation cases used a range of 4 hours from solar noon to study the behaviour of the concentrator. The number of rays used for these simulations were determined by the convergence study described in section 4.1.1.

To determine the average number of reflections of the concentrator, the simulation cases were run with two different reflectance values for the concentrator walls. The reflectance assigned was 100% and 99.9%, respectively. The results from these two sets of simulations were then used to calculate the average number of reflections using Equation 2.32.

4.1.3. Diffuse Horizontal Irradiance

The simulation was divided into two cases, one with diffuse irradiation coming from the sky hemisphere, and the other from the ground hemisphere with the assumption that radiation distribution follows Lamberts Law (isotropic distribution) for both cases. The objective of these simulations was to obtain the acceptance efficiency and the number of reflections under the specified conditions. These could then be used to estimate the optical efficiency of the concentrator when subjected to diffuse irradiance and reflected irradiance, as discussed in section 3.3.1.

The geometrical definition of the concentrator was kept the same as described in section 4.1. . On the other hand, the source was defined to be a parallel source with an angular distribution of a direction cosine ellipse with major and minor semidiameters of 1. This resulted in radiation distributed over a hemisphere, following Lamberts Law, with the rays coming from above or below the ground, for the sky and ground simulations, respectively. Similar to the previous simulations, the average number of reflections was calculated by running the same cases with reflectance of 100% and 99.9%. The incident flux was defined as the total incoming power over the area of the outlet. The geometry and ray distribution for the summer configuration with sky diffuse radiation is shown in Figure 4.2.

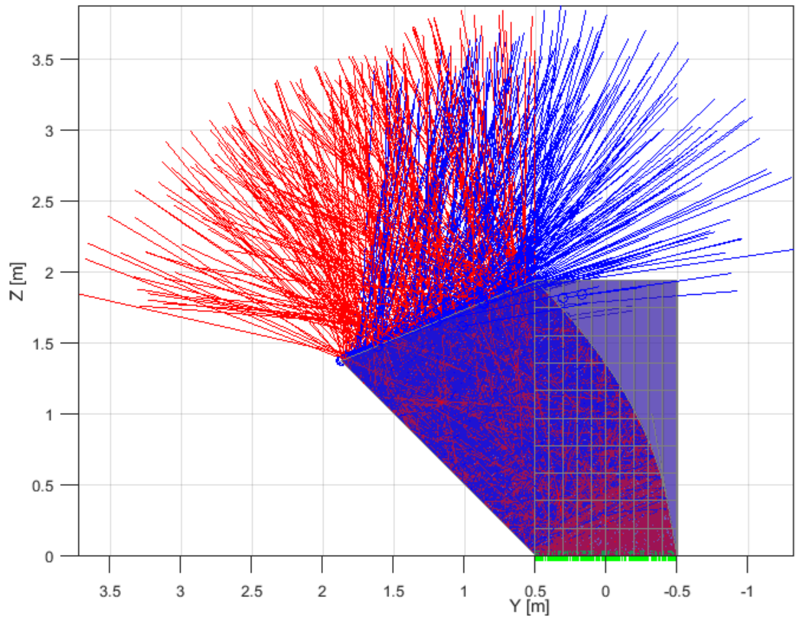

Figure 4.2 - Simulated DHI incident on simulated geometry. The image portrays 1% of the total amount of rays used for the simulation. Rays that reached the outlet are represented in red, and rays that failed to reach the outlet, represented in blue.

4.2. Experimental Methodology

4.2.1. Flux Mapping

The flux mapping procedure had the objective of measuring the irradiance that reaches the outlet of the concentrator during regular operation, while measuring the available radiation from the Sun. These measurements allowed for calculating the flux concentration of the Seasonally Adaptive ACPC, map the distribution of flux onto the outlet and verify the theoretical operation of the concentrator. The experiment entailed placing a Lambertian target at the outlet of the concentrator, capturing gray-scale images of said target and utilize them to calculate the irradiance on the output aperture by relating the images' grey values to the incoming solar flux. This was achieved by calibrating the grey scale values of the camera pixels with the incoming GHI.

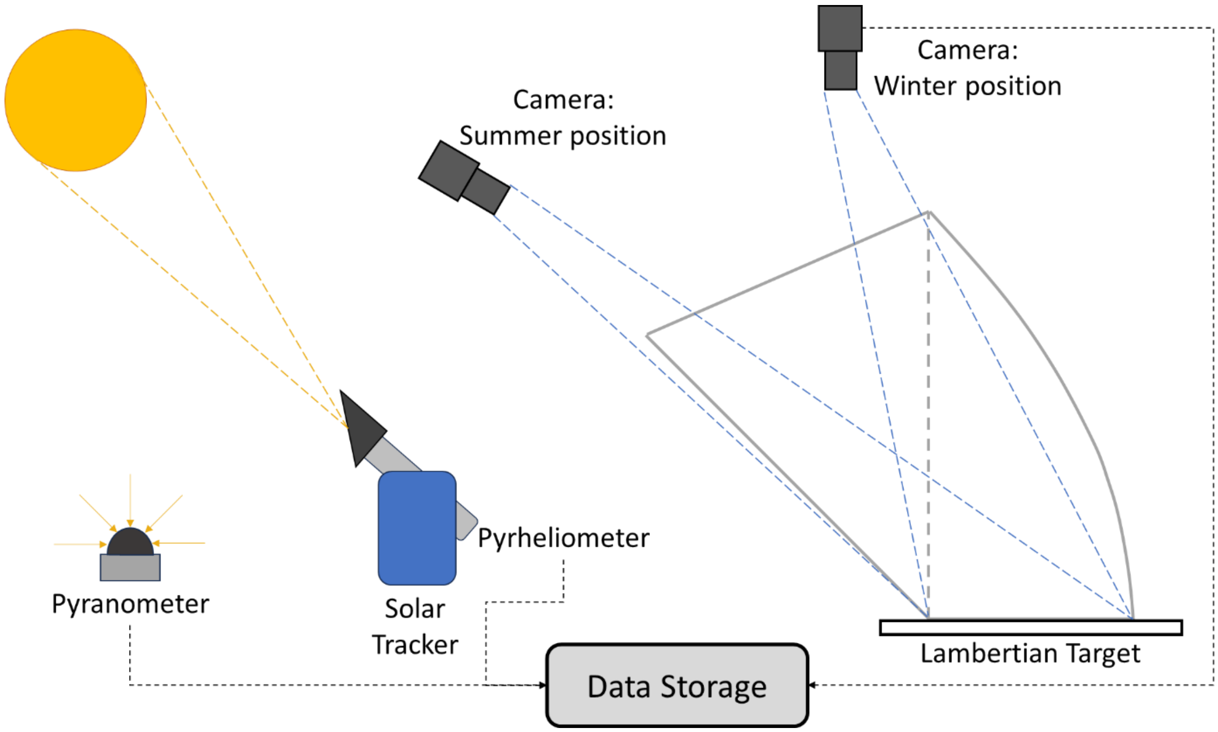

Figure 4.3 - Diagram of the flux mapping experimental set-up

The experimental procedures were performed on top of the Bergeron Building at York University in Toronto, Canada (43.772° North, 79.507° West). The days when the experiments were performed can be seen in Table 4.1, which were selected as representative dates to describe the yearly performance of the Seasonally Adaptive ACPC. Because the experiment was to be performed outdoors, testing when the weather conditions were expected to have few clouds and clear skies were of great importance to limit noise in the data. Table 4.1 also shows the configuration used for each experiment date and the theoretical peak concentration achievable for the day.

Table 4.1 - List of date when the experimental flux mapping procedures were performed.

Date	**Maximum α_s**	**Configuration**	**Theoretical Peak C_f**
July 10th, 2023	68.6°	Summer	1.48×
July 25th, 2022	65.9°	Summer	1.48×
September 23rd, 2022	46.1°	Summer	1.37×
September 29th, 2022	43.8°	Summer	1.34×
November 23rd, 2022	25.9°	Winter	1.75×

4.2.1.1. Experimental Equipment

The main experimental assembly seen in Figure 4.4 served as a base for the concentrator, Lambertian target and camera. This base only allowed for the concentrator to sit in place in a single location, avoiding misalignments in the concentrator positioning with respect to the camera. The Lambertian target used was a 24’ by 24’ plastic sheet designed to behave as a Lambertian Surface, or an ideal diffusely reflecting surface (see Table 4.2). These surfaces are considered to have an isotropic radiance when illuminated which follows Lambert’s cosine law [46], [47]. The concentrator (and assembly) was position so that it aligned towards the south (-*Y* direction), ensuring the surface azimuth $\gamma = 0°$ (see section 2.4.2).

Figure 4.4 - Experimental Setup

The grey scale camera was placed outside of the direct line of sight between the concentrator’s inlet and the sun’s position throughout the day. The camera was placed in front of the concentrator’s front edge at 52° from the vertical for all summer configuration days and directly overhead of the concentrator during all Winter Configuration days (see Figure 4.3). A monochromatic camera was chosen because it’s sensors only recognize brightness, regardless of the colour of the light. The image acquisition software used (*Spinnaker*), also allowed for the control of the camera settings. The image acquisition was set to obtain 1 image every 10 seconds for the whole duration of the experiments, which included time stamps for data processing. The general camera settings are summarized in the following table.

Table 4.2 - Experimental apparatus

Equipment	Brand & Model	Specifications	Data Acquisition Settings
Pyrheliometer	Kipp & Zonen "Pyrheliometer CH1 Serial no: 080042"	Sensitivity: 9.79x10^-6 V/Wm^{-2} Response Time: 7s - 10s (95% to 99%)	Sample rate = 0.5 s^{-1}
Pyranometer	Kipp & Zonen "Pyranometer CM4 Serial no: 120347"	Sensitivity: 9.22 x 10^-6 V/Wm^{-2} Response Time: <8s (63%), 18s (95%)	Sample rate = 0.5 s^{-1}
Monochrome Camera	FLIR "Blackfly S BFS-PGE-31S4M"	Resolution: 2048 × 1536 Sensor: Sony IMX265 (CMOS) Exposure range: 25 μs to 30 seconds	Sample rate = 0.1 s^{-1} Gain = 0 (Auto = off) Gamma = off Black Level Clamping = on Exposure time (eT) = 25 - 48 μs Pixel format = mono16
Lambertian Target	Anomet "WhiteOptics® Film 98"	Dimensions: 24 in × 24 in	N/A

Both the Global Horizontal Irradiance (H_G) and Direct Normal Irradiance (H_N) were measured, which allowed for the calculation of the Diffuse Horizontal Irradiance (H_d) (see Equation 2.8)[19]. The GHI and DNI were measured every 2 seconds, using a pyranometer and a pyrheliometer[20], respectively. The pyranometer and pyrheliometer were placed south of the concentrator without any surrounding obstructions of light for an accurate reading. The pyrheliometer was installed on a telescope tracker

[19] This is grouping both the diffuse and reflected irradiance under DHI, as highlighted in chapter 2.
[20] The pyranometer and pyrheliometer are thermopile sensors commonly used for solar radiation measurements and help assess the efficiency of solar collectors and photovoltaic panels. The pyranometer is able to measure the GHI, and the pyrheliometer the DNI.

which allowed for sun tracking throughout the day. This device was set to the date and location of the test site for tracking, and the alignment with the solar vector was ensured using the built-in sight of the pyrheliometer. The pyranometer and pyrheliometer's response time and sensitivity are reported in Table 4.2. The device used for recording the pyranometer and pyrheliometer measurements was a thermocouple reader set to record S-type thermocouples. The recorded thermocouple reader data, in degrees Celsius, was subsequently converted into voltage using both the S-type thermocouple tables and the temperature around the Thermocouple reader.

$$Voltage\ (V) = -S_{S-type}\Delta T$$

Equation 4.1 - Governing equation for thermocouples

The voltage values obtained were then converted into irradiance values using the pyrheliometer's and pyranometer's sensitivity and the following equation. The values obtained from this equation were subsequently verified using the data provided by the York University's ESSE Meteorological Observation Station (EMOS) and found to be within 15% error in the worst cases.

$$H(W/m^2) = \frac{Voltage\ (V)}{Sensitivity\ (\mathrm{V/W/m^2})}$$

Equation 4.2 - Calculation of Irradiance from pyrheliometer/pyranometer readings

4.2.1.2. Experimental Procedure

The flux mapping experiment involved the following key steps:

(1) Set up of experimental apparatus and continuous data acquisition (both camera and sensors)

(2) Removal of the concentrator from the Lambertian target (out of camera's line of sight and without reflecting radiation towards the target) and acquisition of calibration image.

(3) Reinstallation (if removed) of concentrator on Lambertian target and image acquisition of outlet irradiance.

(4) Data processing of images and sensor measurements

The calibration procedure involved the Lambertian target having an unobstructed line of sight to the Sun, capturing an image of the target and a simultaneous GHI measurement. The relationship between irradiance (*H*) and gray value (*gV*) can be seen in the following equation where *eT* is the exposure time of the camera and *k* is the calibration constant that relates the three other values. Knowing the irradiance from the GHI measurement, the gray value from the camera and the predefined exposure time, it's possible to calculate the proportionality constant k. This constant allows for the measuring of the irradiance when the concentrator is on the Lambertian target, as long as the exposure time remains constant, and the camera sensor is not saturated. In this equation H is equal to H_G when calculating k during calibration, and H_O during regular operation.

$$H = \frac{gV}{k \cdot eT}$$

Equation 4.3 - Calculation of Irradiance from grey-value, exposure time and calibration constant

After calibration, the concentrator was placed on top of the Lambertian target, making sure there were no gaps between this surface and the outlet of the concentrator. The greyscale camera was then used to take images of the Lambertian target every 10 seconds. The camera captured images continuously, and calibration images were taken every 20 to 30 minutes by removing the concentrator from the Lambertian target. During data acquisition, the camera sensor's grey value histogram was kept under observation, to ensure the camera sensor wasn't saturated (over exposed). To control the sensor's saturation, or under exposure, the exposure time was modified from the *Spinnaker* software.

Finally, the data processing following the tests was performed using a custom software written on *Matlab*. The software developed used the raw thermocouple data, captured images and datetime data as input to perform the calibration calculations based on calibration images, and calculate the output irradiance and concentration throughout the test period.

4.2.1.3. Experimental Uncertainty

The uncertainty associated with the experimental measurements obtained from the procedure described above can be classified into irradiance and camera uncertainty. The first is related to the propagated uncertainty of the pyranometer when measuring GHI and the pyrheliometer when measuring the DNI. On the other hand, the latter one can be attributed to the propagated camera uncertainty when measuring the grey value. These two sets of uncertainties then propagate into the calibration constant and the calculated output irradiance H_o.

The uncertainty of the pyranometer can be calculated considering the propagation of the sensor's non-linearity, non-stability, directional error, and temperature dependence, reported in percentages by the manufacturer. With the non-stability being the largest contributing factor, the total relative uncertainty of the GHI measurements σ_{GHI}/H_G is 10.3%. Similarly, the uncertainty of the pyrheliometer is based on the non-linearity, non-stability, calibration accuracy and temperature dependence. Like with the GHI measurements, the DNI uncertainty is mainly affected by the non-stability, and the total relative uncertainty σ_{DNI}/H_N reaches 10.1%.

The grey value uncertainty σ_{gV} can be calculated using Equation 4.4, where $\sigma_{d,gV}$ is the temporal dark noise, $\sigma_{q,gV}$ is the quantization noise, and $\sigma_{e,gV}$ is the photon shot noise [48]. Of these components, the $\sigma_{q,gV}$ defined by a fixed value, and the $\sigma_{e,gV}$ is defined by the square root of the grey value, for which the average grey value of the image was used.

$$\sigma_{gV} = \sqrt{\sigma_{d,gV}^2 + \sigma_{q,gV}^2 + \sigma_{e,gV}^2}$$

Equation 4.4 - Grey value uncertainty

Finally, the temporal dark noise can be calculated using Equation 4.5, where $\sigma_{read,gV}$ is the read noise, and I_{gV} is the dark current.

$$\sigma_{d,gV}^2 = \sigma_{read,gV}^2 + I_{gV} \cdot eT$$

Equation 4.5 - Temporal dark noise

Following these definitions its possible to quantify the propagation of uncertainty into the calibration constant of the flux mapping procedure and the output irradiance. As seen in the previous section, the calibration constant k depends on the irradiance (GHI) measured during calibration, $H_{G,c}$, and the average grey value of the calibration image gV_c. Following Equation 4.3, the total uncertainty in the calibration constant can be estimated from Equation 4.6. Here the GHI and grey value uncertainty are specified to be from calibration values using the subscript c.

$$\sigma_k = \sqrt{\sigma_{H_{G,c}} \left(\frac{\partial k}{\partial H}\right)^2 + \sigma_{gV,c} \left(\frac{\partial k}{\partial gV}\right)^2}$$

Equation 4.6 - Calibration uncertainty

Similarly, the uncertainty of the output irradiance can be quantified using Equation 4.7, which depends on the propagation of the grey value and calibration constant uncertainty.

$$\sigma_{H_o} = \sqrt{\sigma_{gV} \left(\frac{\partial H_o}{\partial gV}\right)^2 + \sigma_k \left(\frac{\partial H_o}{\partial k}\right)^2}$$

Equation 4.7 - Uncertainty of the output irradiance measured.

Chapter 5: Results

5.1. Simulations

5.1.1. Transmission Angle Curve

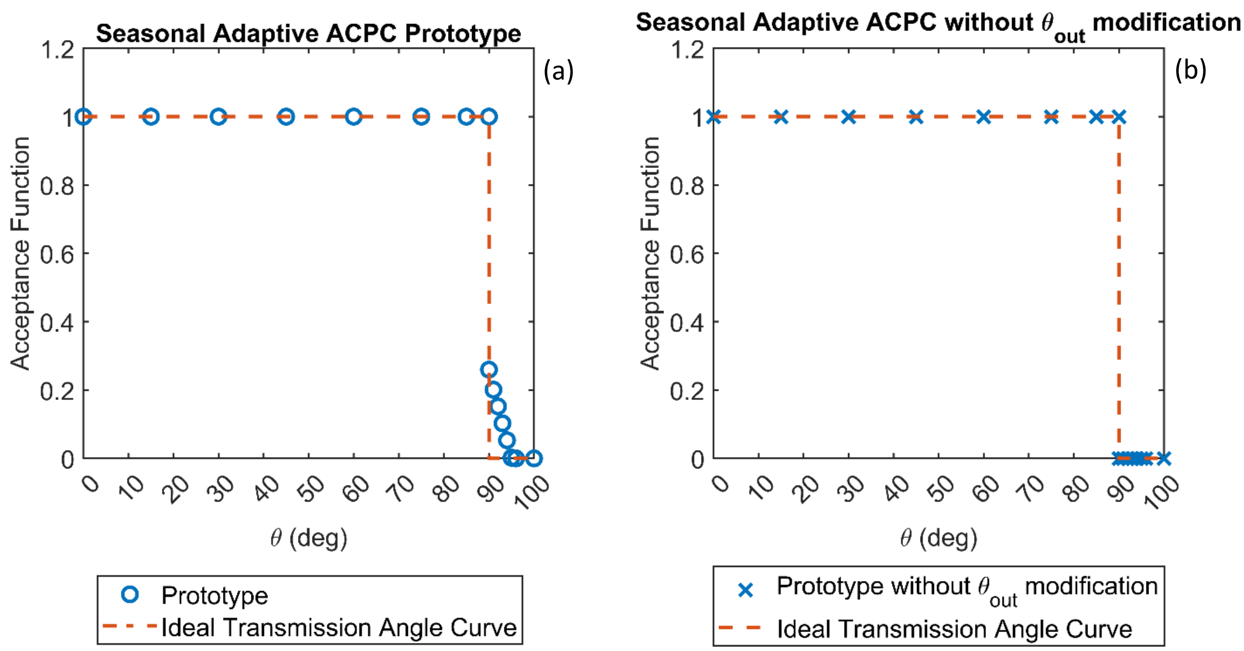

Figure 5.1 - a) Transmission Angle Curve for the Seasonally Adaptive ACPC prototype and b) Ideal Transmission Angle Curve for an ACPC

The optical model described in section 4.1. was subjected to the conditions described in section 4.1.1, to determine the acceptance function (F(ϑ)), and therefore the transmission angle curve of the concentrator design used for the Seasonally Adaptive ACPC prototype. The F(ϑ) was calculated for the prototype following (Equation 2.14), which, for the case of ρ = 1, is simply the ratio between the power reaching the outlet to the power entering the inlet aperture. As can be seen in Figure 5.1a, the transmission angle curve of the prototype shows ideal behaviour until reaching 90°, where it portrays an acceptance of ~26%. From this point F(ϑ) decreases linearly until reaching ~95°, around 5° higher than the ideal case. This deviation from the ideal acceptance is most likely due to the presence of the θ_{out} modification in the design. As explained in section 3.1.4, for an acceptance angle of θ_{in} there is a range of incidence angles past θ_{in}, where a θ_{in}/ θ_{out} concentrator accepts a portion of the radiation. To verify this deviation from the ideal case is associated with the presence of the θ_{out} modification, a 0°-

90° Seasonally Adaptive ACPC without a θ_{out} modification was subjected to the same simulation scenarios to find its Transmission Angle Curve. Figure 5.1b confirms this hypothesis by demonstrating that the Seasonally Adaptive ACPC behaves as an ideal concentrator.

5.1.2. Direct Normal Irradiance

The optical model was subjected to simulated solar rays in the direction of the Sun's position on the dates of the flux mapping experiment. This allowed to calculate the average number of reflections, concentration, acceptance efficiency and obtain the flux distribution of at the outlet on these dates and times. The flux concentration was calculated from the optical simulations, following the ratio of flux entering the concentrator's outlet area to the one entering the inlet area. The results were found to match the theoretical prediction with under 1e-3% error, confirming the validity of the theoretical equations.

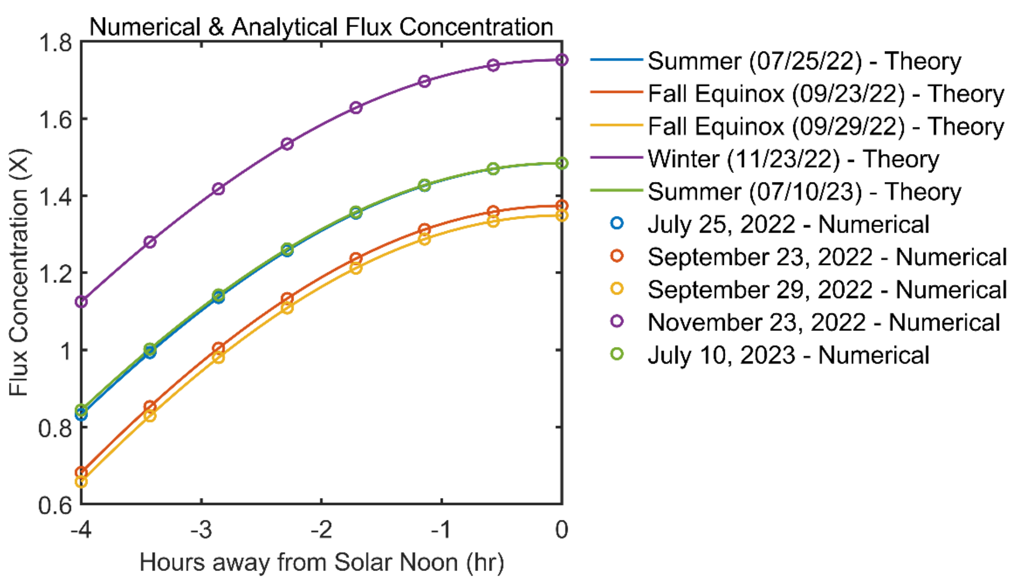

Figure 5.2 - Comparison between theoretical and numerical flux concentration

As the Sun position changes in the sky, the rays that hit the concentrator follow a distinct path, reflecting on the concentrator walls. Each of these reflections reduce the power of the incoming rays by the reflectance of the surfaces, reducing the output flux. MCRT simulates this power loss by treating photons as individual rays with a probability of getting absorbed on each surface, where this probability is dictated by the reflectance of the surface. Each ray can undergo a different number of reflections, making estimating the power lost a difficult task. To simplify this calculation, an average number of reflections is calculated, allowing for a much simpler calculation of the ratio of power lost or optical efficiency. Equation 2.32 was used to find the average number of reflections in the concentrator for all altitude angles, ranging from 0 to 90, and throughout the day. The following figure shows the behaviour of $\langle n_r \rangle$ for a range of altitude angles for each configuration, not including the effect of the azimuth angle. This specific condition shows the behaviour of the Seasonally Adaptive ACPC as a two-dimensional concentrator, which is equivalent to an infinitely long concentrator. Considering the position of the sun in the sky through the year, the reflectance of the concentrator, and the acceptance efficiency demonstrated above, it is possible to estimate the optical efficiency of the concentrator using the $\langle n_r \rangle$ curve in Figure 5.3 and Equation 2.29.

The efficiency of this concentrator is highlighted in the Figure 5.3, demonstrating a very low reduction in power within its acceptance angle, thanks to the low number of reflections. The optical efficiency shown in the plot uses a reflectance of 95%, portraying the theoretical efficiency when utilizing the prototype reflectors. Along with this, the maximum solar altitudes (for Toronto, 43°39'N) are represented by a vertical red line, showing the range of average number of reflections for each configuration.

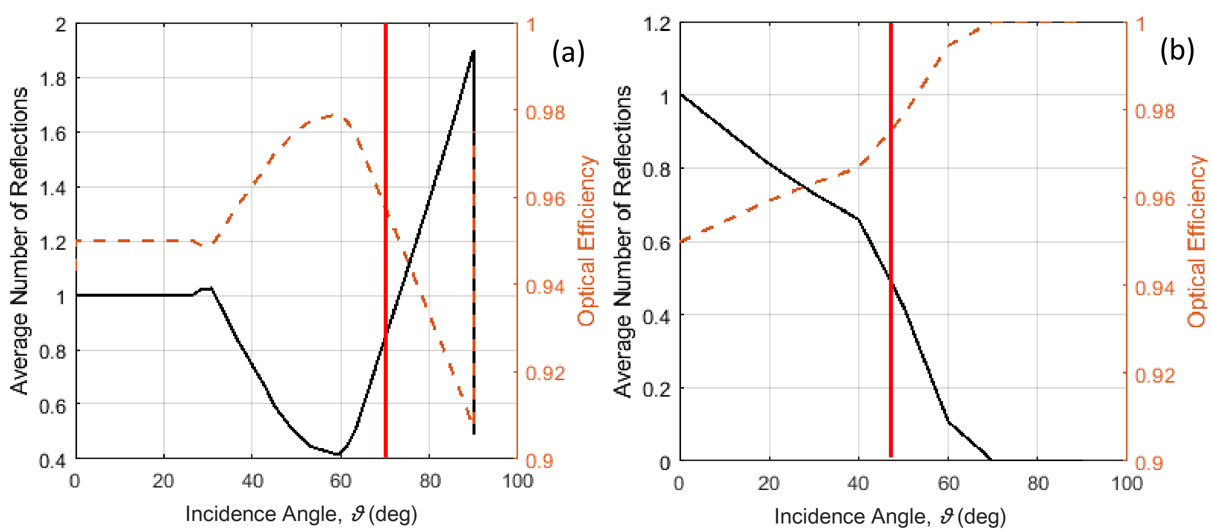

Figure 5.3 - Average Number of Reflections & Optical Efficiency for a 2D Seasonally Adaptive ACPC, using a reflectance of 0.95 for (a) Summer configuration and (b) Winter configuration

Unlike the two-dimensional concentrator seen before, a concentrator with a finite depth will only follow the behaviour seen above at solar noon. Outside of this time, it will either have end losses due to lost rays, or a higher number of reflections, if utilizing reflective side walls. Both of these scenarios will cause lower optical efficiency than the 2D concentrator, but the latter can result in better optical efficiency than the former, depending on the depth of the concentrator. The higher average number of reflections that occur due to the side walls and the finite nature of the concentrator was studied using the prototype's geometry. The method to calculate the average number of reflections was similar to the one described previously, but unlike the previous case, this simulation considered the solar azymuth.

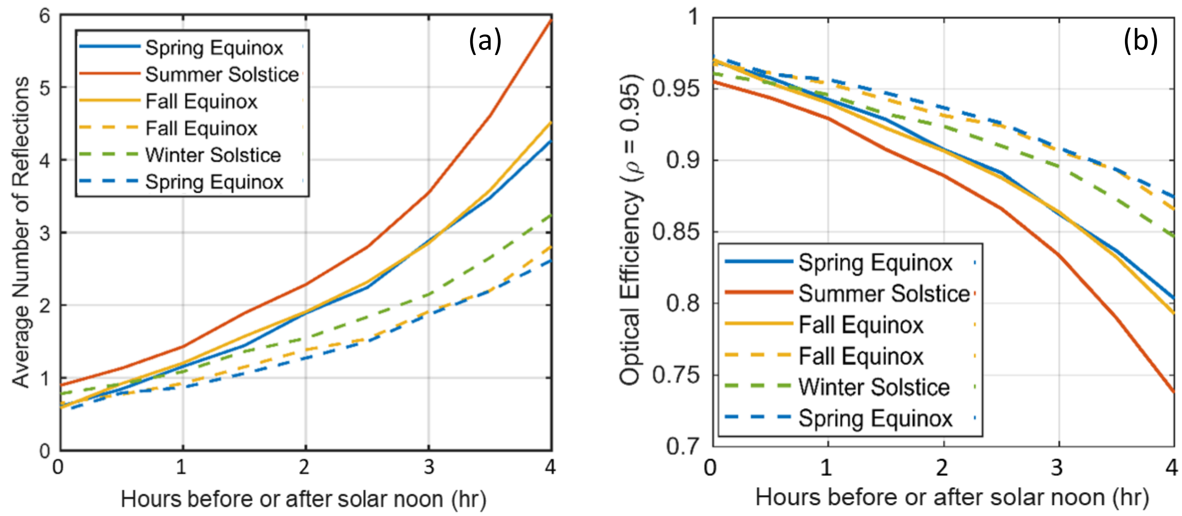

Figure 5.4 - (a) Average Number of Reflections for each configuration's date range and (b) Optical efficiency for each configuration's date range. With the summer configuration marked by solid lines, and the winter configuration marked by dotted lines.

As expected, the resulting number of reflections at solar noon is similar to the one for the two-dimensional concentrator. Figure 5.4a grants a great deal of understanding on the daily and yearly behaviour of the number of reflections for this concentrator, and therefore its optical efficiency. As the Sun deviates from Solar noon (both before and after), the resulting number of reflections increases significantly. The winter configuration demonstrates overall lower $\langle n_r \rangle$, resulting in a more efficient performance. For both configurations, the respective solstice marks the date with the highest number of reflections, and the equinoxes the dates with the lowest number of reflections. All other dates not shown in the figure would be encompassed by the area between the Solstice curve and the equinoxes curves, for each configuration, with these dates following a similar curve than the ones shown. For example, a day in May, would show a curve found within the area between the summer solstice curve and solid spring equinox curve, with a similar profile to the other two. Whereas the curve for a day in January would fall between the winter solstice and the dotted spring equinox curve. Knowing the acceptance efficiency throughout the year is equal to one, Figure 5.4b shows the resulting ranges of optical efficiency for each of the configurations, for a reflectance of 95%. The lower number of reflections and higher optical efficiency shown by the Winter Configuration, comes as a benefit to the year-round performance of the Seasonally Adaptive ACPC, as during this period of the year the incident solar radiation tends to be more diffuse.

5.1.3. Diffuse Horizontal Irradiance & Reflected Irradiance

The optical model was subjected to diffuse radiation coming from both the sky and ground, representing the diffuse horizontal irradiance and the reflected irradiance, with the objective of understanding the acceptance, average number of reflections and optical efficiency of the concentrator for this type of radiation. With the sky diffuse irradiance distribution following Lambert's Law and the ground reflected irradiance being treated as isotropic, the optical efficiency can be modeled using the following equation[13], [37]. When dealing with diffuse irradiance, the Geometric Factor (R_β) uses a positive sign, and the irradiance term, H, is equal to the sky's diffuse irradiance (H_d). On the other hand, for ground reflected radiation, the cosine term in R_β is negative, and the irradiance term is equal to the global horizontal irradiance (H_G) times the ground albedo (ρ_a).

$$\eta_{op,d} = \frac{Q_o}{H}\left(\frac{1 \pm \cos\beta_t}{2}\right)^{-1} \rho^{<n>} = \frac{Q_o}{H} * \frac{1}{R_\beta} * \rho^{<n>} = \eta_{acc} * \rho^{\langle n \rangle}$$

Equation 5.1 - Optical Efficiency of Diffuse Radiation

The following table shows the results from the MCRT simulations for both cases and configurations. The resulting flux concentration demonstrates that the winter configuration takes advantage of the diffuse radiation, which can result in higher output fluxes. On the other hand, the three other cases show a flux concentration lower than 1, resulting in an output flux lower than the incoming diffuse irradiance. The reported geometric factor can be used to investigate the ratio of output power to available irradiance.

Table 5.1 - Performance of Seasonally Adaptive ACPC under Diffuse Horizontal Irradiance & Reflected Irradiance

Configuration	**Source of Irradiance**	**Acceptance Efficiency η_{acc}**	**Avg. Number of Reflections $\langle n \rangle$**	**Flux Concentration C_f**	**Geometric Factor R_β**
Summer	Sky	0.5255	1.3325	0.7801	~0.962
	Ground	0.5549	0.1494	0.8228	~0.038
Winter	Sky	1.0000	1.0256	1.9390	0.5
	Ground	0.4141	0.0318	0.8035	0.5

5.2. Experiments

5.2.1. Flux Mapping Experiments

The experiments performed allowed for the measurement and calculation of Output Flux, Flux Concentration, and flux distribution at the outlet of the concentrator. The flux mapping experiments were performed using the summer configuration on July 25th , September 23rd and 29th , in 2022, as well as July 10th , 2023; and the winter configuration on November 23rd , 2022.

5.2.1.1. Summer Experiments

The experiments performed in July showcase the summer performance of the concentrator. For test performed on July 25th, the theoretical peak concentration reached up to 1.484×, which the day of the test occurred at 1:24pm (Solar noon). This test lasted 2 hours, between 1:40 pm and 3:40 pm, with calibration images taken every 20 minutes. Figure 5.5a shows the concentrated solar flux exiting the concentrator, along with the GHI, DNI and DHI reaching the concentrator during the full two hours of the test. As it is visible in this figure, during this test the direct irradiance was largely obstructed by passing clouds, causing large fluctuations in the measured irradiance readings. As expected, the direct radiation is the only one to be significantly concentrated but, when DNI is mostly obstructed, the outgoing solar flux is around the value of GHI. This indicates that, unlike concentrators with smaller acceptance angles, using this concentrator design on a receiver during overcast days can allow the receiver to perform as well as it would without the concentrator.

Figure 5.5b shows a small section (~20 minutes) of the full test performed, which had relatively stable irradiance readings, unlike the rest of the test for this date. The step down in the figure displays a calibration measurement performed during this time, with the lower valley resulting from a shadow when placing the concentrator back into the setup. This plot more prominently shows the operation of the concentrator during sunnier conditions, with the major contributor to the concentrated flux being the direct irradiance. Similarly, it portrays how the diffuse irradiation plays a small, but significant, part by dictating the pattern of the outgoing concentrated flux during this time frame.

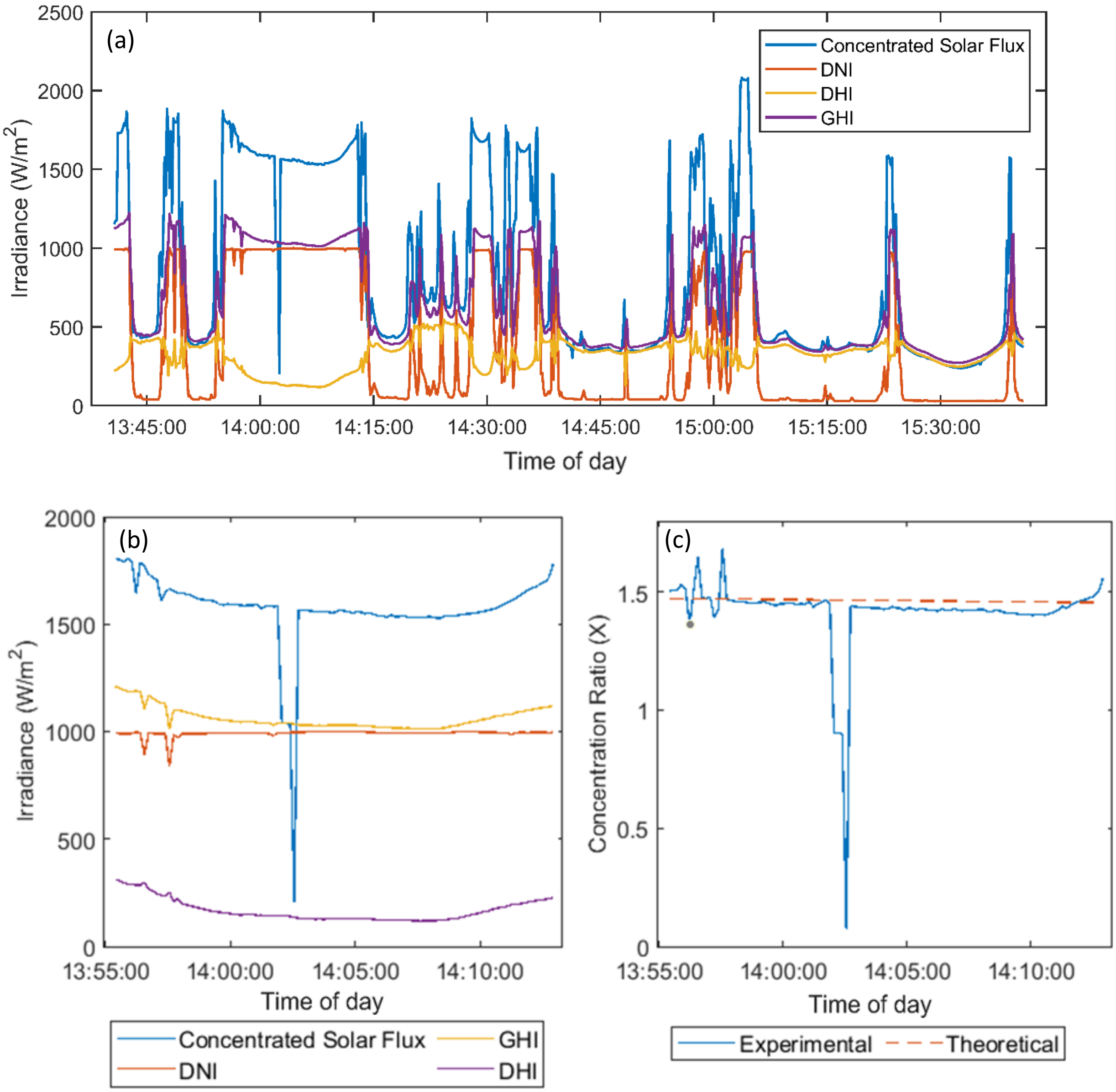

Figure 5.5 - Results from July 25th, 2022

The concentration resulting from this same test period can be seen in Figure 5.5c, together with the theoretical concentration. The concentration ratio shown in this figure only considers direct radiation and is calculated using the following equation. The flux concentration resulting from this test differs from the theoretical concentration up to 4%, showing a good match between real world and theoretical performance. The sudden peaks and valleys in the concentration are often caused by a mismatch between the response time of the camera and irradiance sensors, this issue is mostly prominent in Figure 5.5c because of how concentration is calculated.

$$C_{f,avg} = \frac{H_{avg} - DHI}{DNI}$$

Equation 5.2 - Experimental Average Flux Concentration Ratio

For the test performed on July 10th, 2023, the maximum theoretical concentration reached was 1.484×, as it does for most of the summer configuration, which occurred at 1:22 pm. The test lasted 5 hours, from 11:11 am until 4:20 pm, with calibration images taken every 30 minutes. Figure 5.6a, shows the concentrated solar flux reaching the outlet of the concentrator, along with the GHI, DNI and DHI measured during the test. Even though the presence of clouds obstructing the incoming radiation also played a role in this test, it was lower than the one on July 25th, this along with the duration of the test, made it possible to observe the overall trend of the concentrated flux. The experimental output flux reached a maximum of 1546.7 W/m^2, which occurred at 1:21pm, 1 minute before solar noon.

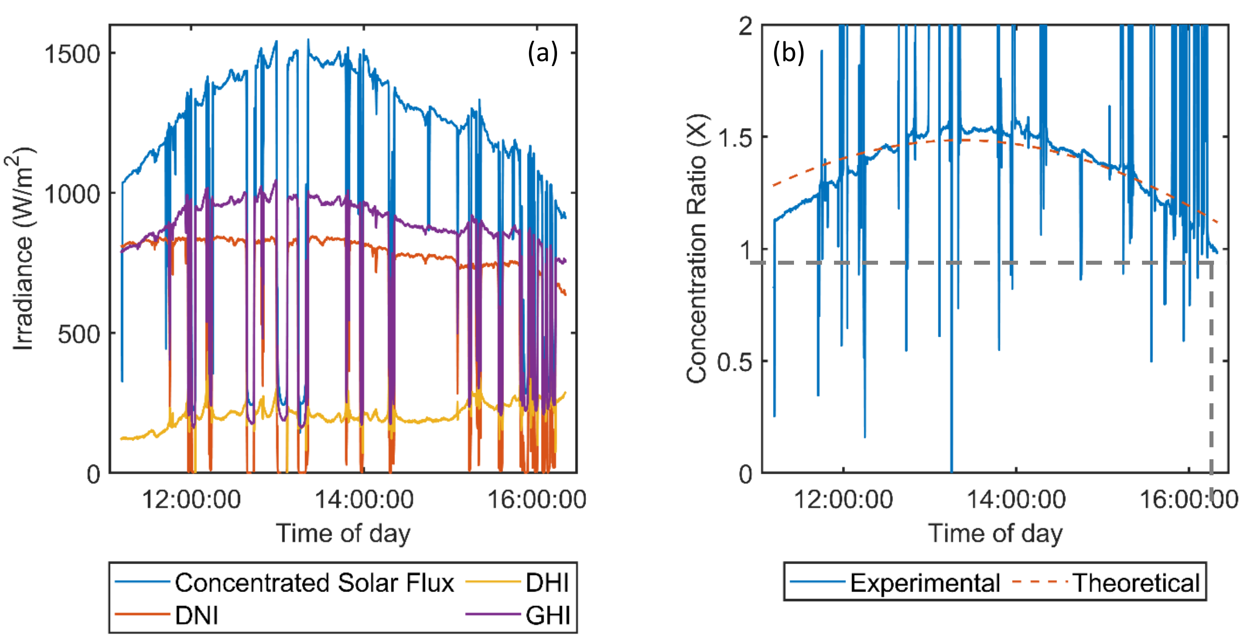

Figure 5.6 - Results from July 10th, 2023

On the other hand, Figure 5.6 shows the calculated concentration, reaching a maximum of 1.582×, 6.6% higher than the theoretical one. Like the previous experiment, the difference in response time between sensors caused sudden peaks and valleys in the concentration, which are associated with sudden changes in incoming irradiance due to cloud coverage. The calculated concentration can be observed to be decreasing under 1× at 4:17 pm, which is 5 minutes short of the 3-hour mark. At this time, the theoretical concentration is around 1.109×, ~11% higher.

5.2.1.2. Equinox Experiments

There were two experiments performed around the fall equinox, both using the Summer Configuration. Both experiments were performed on very clear sunny days, which allowed for the data to be considerably cleaner and without much noise. The first test was performed on the day of the equinox (September 23rd, 2022), the theoretical peak concentration for this date reaches up to 1.374x, which the day of the test occurred at 1:09pm (Solar noon). Similarly, the minimum concentration for this day is 0.969x, and happens 3hrs before and after solar noon, at 10:09am and 4:09pm, respectively. This test lasted 2.15 hours, between 2:50 pm and 5:00 pm, with only two calibration images taken 20 minutes apart during the first 30 minutes of the test. This test focused on the last portion of a day's performance, with the purpose of studying when concentration goes bellow 1x, and when output flux goes bellow the DNI. Following the assumption made in Equation 5.2, these two should happen at the same time, but considering the concentrator accepts diffuse radiation, it holds that the former would occur before the latter. As can be seen in Figure 5.7a, the concentrated flux diminishes past the direct irradiance at around 3:55 pm, which is 14 minutes short of the 3hr mark from solar noon. On the other hand, the theoretical concentration falls under 1x at 3:54pm, which means that the output flux matches well with the theoretical behaviour. The experimental concentration ratio calculated using Equation 5.2, diminishes past 1x at 3:30 pm, which is around 25 minutes before predicted by theory. When this happens, the theoretical ratio is 8% higher than the experimental one. This gap can be attributed to the reflectance of the concentrator and increased number of reflections during this time. Regardless, while considering the losses, it is beneficial that the concentrator is able to match the theoretical performance thanks to its ability to accept diffuse irradiance. The valley seen in the DNI reading at around 3:10 pm is associated with an obstruction of the pyrheliometer, and because DHI data is calculated from GHI and DNI readings, there is an accompanying peak in DHI. Similarly, the valleys in the output flux data occurring after the two calibration images mentioned are associated with obstructions of the radiation reaching the concentrator.

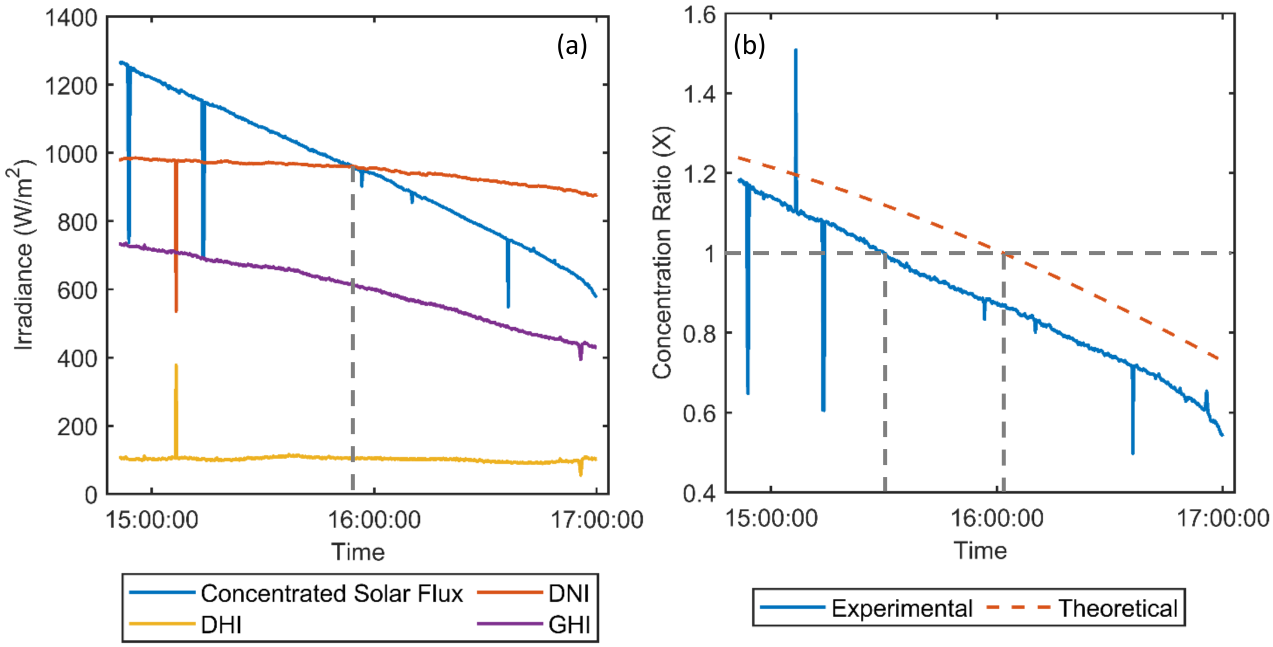

Figure 5.7 - Results of September 23rd, 2022

The second equinox experiment was performed 6 days after the equinox (September 29th, 2022), while using the summer configuration, even though the configuration change should happen on the equinox or the day after. The theoretical peak concentration for this date and configuration reaches up to 1.349x, which the day of the test occurred at 1:07pm (Solar noon). Similarly, the minimum concentration for this day is 0.944x, and happens 3hrs before and after solar noon, at 10:07am and 4:07pm, respectively. Using the winter configuration for this date, results in a theoretical peak concentration of 1.423x, and a minimum theoretical concentration of 1.031x, happening at the same times described above. This experiment lasted 4.5 hours, between 12:00 pm and 4:30 pm, with calibration images taken every 20 minutes for the first 2 hrs, and every 30 minutes until the end of the test. The objective of this test was to study how a lapse in configuration change would affect performance, and to observe the operation through a longer time scale. Following Figure 5.8, and similar to previous experiments, the steps down in the data mark the calibration images. Valleys in irradiance that go down past the GHI data are associated with shadowing while placing the concentrator back into the setup. Thanks to the length of this test, it is possible to clearly observe the arc formed by the output flux and concentration ratio in Figure 5.8a and b, respectively. In this instance, the point at which the concentrated flux diminished under the DNI value was at 3:55 pm, matching again with the time at which the theoretical concentration ratio decreased under 1x, 12 minutes before the 3hrs after solar noon mark. Like the previous test, the point at which the experimental concentration decreased under 1x happened around 20 minutes before this, at 3:35 pm, and 30 minutes before the 3hrs after solar noon mark. Notice that the 4 steps down seen to go further than the GHI curve in the figure are associated with the motion of the camera during reinstallation of the concentrator onto the Lambertian target. In these instances, the camera took an image when facing the ground, reducing the irradiance captured.

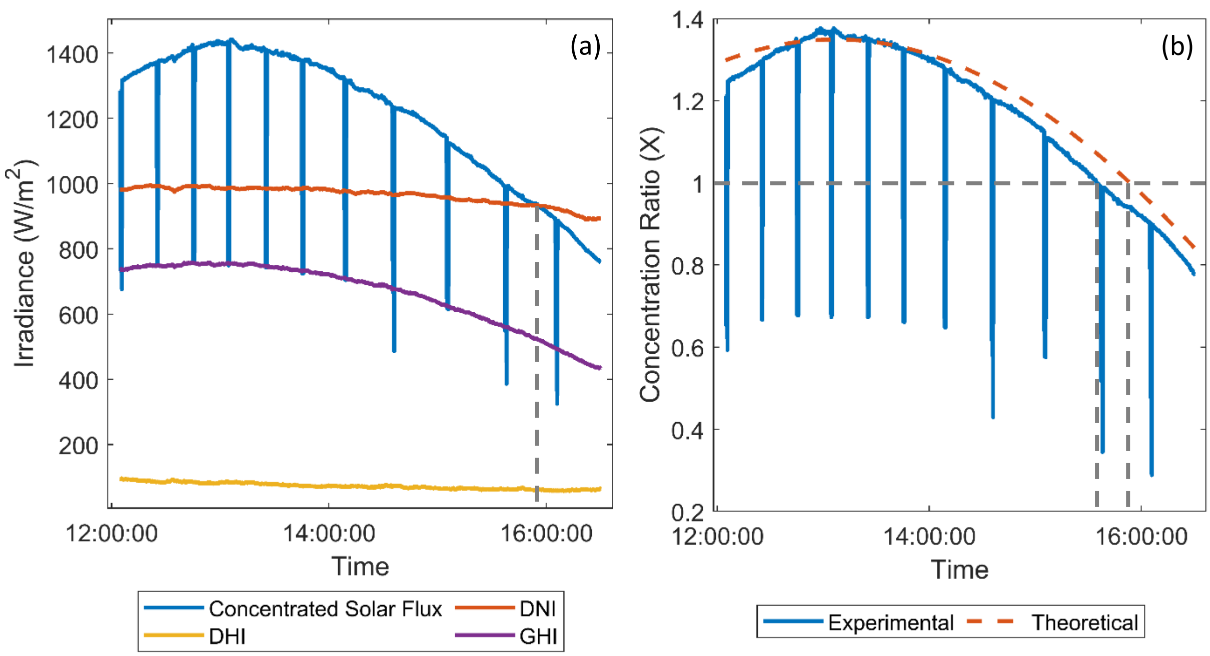

Figure 5.8 - Results of September 29th, 2022

5.2.1.3. Winter Experiment

The experiment was performed in winter (November 23rd, 2022), while using the winter configuration. The theoretical peak concentration for this date reaches up to 1.752x, which the day of the test occurred at 12:03pm (Solar noon). Similarly, the minimum concentration for this day is 1.385x, and happens 3hrs before and after solar noon, at 9:03am and 3:03pm, respectively. This experiment lasted 4.3 hours, between 10:45 pm and 3:05 pm, with calibration images taken every 20 minutes for the first hour, and every 30 minutes until the end of the test. This experiment was performed to study the winter operation of the concentrator. There were clouds on the day of this experiment, causing fluctuation in the data visible in Figure 5.9a. The overall irradiance for this date was lower than previous experiments, which is expected as solar irradiance tends to be lower in the winter. The resulting concentration approached the theoretical one closely, with the highest gap being an 8% difference, not accounting for the peak found at 2 pm. This peak is considered to be noise caused by fluctuations in the irradiance in a time scale between the camera's and irradiance sensors' response time.

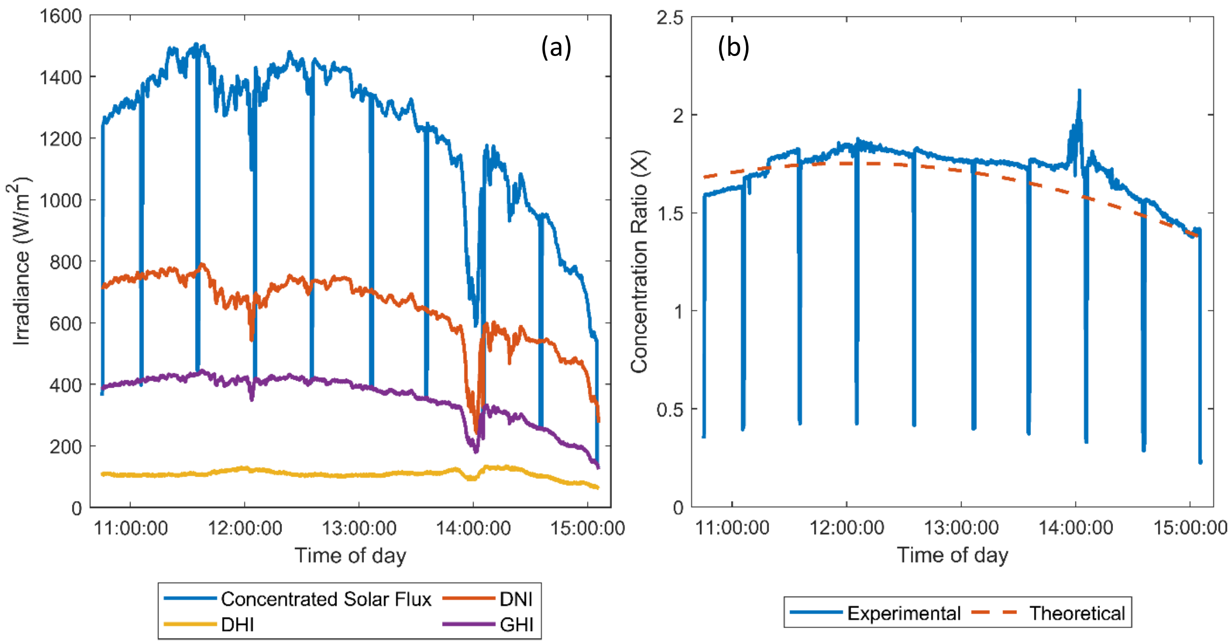

Figure 5.9 - Results of November 23rd, 2022

5.3. Analysis and Discussion

5.3.1. Sources of Error

Some of the major sources of uncertainty in the results presented were found to be the measurements of DNI and GHI, with a relative uncertainty of 10.1% and 10.3%, respectively. As can be seen from the uncertainty equations presented in section 4.2.1, the value of uncertainty of the outlet irradiance fluctuates based on the measured data, but the average relative uncertainty σ_{H_o}/H_o was found to be around 11.0%. The uncertainty calculated wasn't presented in the above figures for visual clarity, but the uncertainty of the measured output flux for all experiments can be seen in Figure 5.10.

Aside from the uncertainty from the measuring devices mentioned, a few sources of error were found to affect the results presented. The clearest one being the fluctuations in irradiance due to passing clouds. This phenomenon caused large and rapid variations in the irradiance, which proved to be faster than the response time of the thermopile sensors, which failed to fully capture the instantaneous changes in irradiance. Unlike these sensors, the camera captured images instantaneously, effectively capturing immediate changes in irradiance. Because of this, the concentration ratio calculated using

Equation 5.2, would tend to have large and sudden peaks and valleys when the fluctuations in irradiance became faster than the response time of the pyranometer and pyrheliometer (>10s), such as the ones seen in Figure 5.6b. Lastly, the surrounding buildings and surfaces might have caused the diffuse irradiance to be less isotropic due to reflections and obstructions, which could have affected readings from the sensors and measurements of the output flux. Similarly, reflections of direct irradiance from nearby surfaces could have been within the acceptance angle of the concentrator, increasing its output.

5.3.2. Concentrated Solar Flux

The output flux of a concentrator is a crucial aspect to consider when assessing the performance and effectiveness of the design. This section explores the resulting output flux through the year, by understanding this behaviour, it's possible to gain valuable insights on the performance of the concentrator and its applications. When considering a standalone stationary design such as the one presented here, the resulting output flux can be very different from what the concentration ratio dictates because of the variation of Sun positions through the year and the changes in solar irradiance. This is portrayed in Equation 3.11, which represents a model for the radiation accepted by the Seasonal Adaptive ACPC but can be extended to any stationary concentrator. Equation 5.3 restates this model while breaking down the optical efficiency to show the different acceptance efficiencies and average number of reflections. As explained in Chapter 3: , the geometric concentration and incidence angle (ϑ) changes between configurations, with both playing the most significant roles in the performance of the design. That being said, as it was found in section 5.1.3, the diffuse and reflected irradiance can play a substantial role in the performance, with acceptance being as high as 1, for diffuse radiation in the winter, and $\langle n \rangle$ no higher than 1.33 overall.

$$H_o = C_g\left(\eta_{acc,N} \cdot \rho^{\langle n_N \rangle} \cdot H_N \cdot \cos\vartheta + \eta_{acc,d} \cdot \rho^{\langle n_d \rangle} \cdot H_d + \eta_{acc,r} \cdot \rho^{\langle n_r \rangle} \cdot \rho_a \cdot H_G\right)$$

Equation 5.3 - Output Flux (Irradiance)

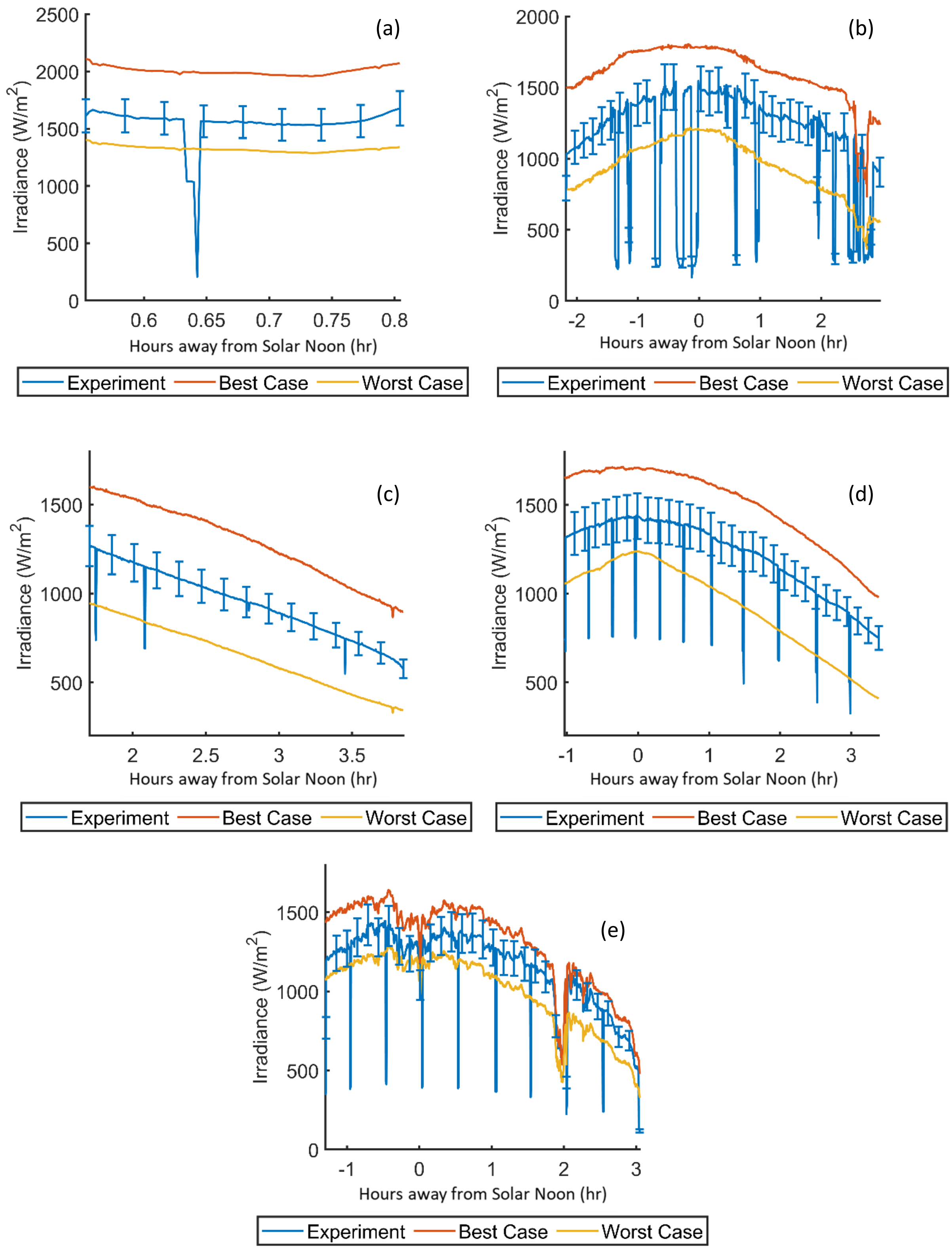

Figure 5.10 - Best and worst cases for the concentrator performance in terms of output flux (irradiance) during the experiment dates: (a) July 25th, 2022, (b) July 10th, 2023, (c) September 23rd, 2022, (d) September 29th, 2022, and (e) November 23rd, 2022.

Using this model and the values reported for acceptance efficiency and number of reflections for direct and diffuse radiation (see sections 5.1.2 and 5.1.3), it's possible to accurately estimate the irradiance at the outlet of the concentrator for any given day. To do this, an estimate of the reflectance of the concentrator's surfaces and the ground albedo are necessary, as well as data for the GHI and DNI. Using this same model, it's possible to calculate the maximum output flux achievable for the experimental dates as well as gain precise insight into the effect that losses have on the performance of this concentrator design. Following this idea, Figure 5.10 shows the best and worst cases scenarios for the output flux for all experimental dates, along with the experimentally observed irradiance reaching the outlet of the concentrator. For the maximum output flux, the values used for reflectance and albedo was ρ = 1, and ρ_a = 0.5; similarly, for the worst cases a reflectance of ρ = 0.8, and an albedo of ρ_a = 0.1 were used. The DNI, DHI and GHI used for the calculation of these curves was the same one measured during the experiments, apart from the ones shown in Figure 5.10b, where large variations in the data were removed for clarity. Considering these parameters, the experimental flux was found to be mostly in the middle of these two curves, even including the uncertainty of the measurements. Because the calculation of these curves depends on the measured irradiances, the best- and worst-case scenarios shown in Figure 5.10 would also have a relative error similar to the DNI's and GHI's but were omitted for visual clarity.

Figure 5.11 is a compilation of all the experiments performed, showing the output flux for each, together with a best fit theoretical flux based on the simulated parameters and measured irradiances, following Equation 5.3. Note that the experimental results presented here have removed the outlier data from calibration images, and present only 1 of every 5 data points to improve clarity. As can be expected, the concentrated flux in the summer (July 25th) is the highest measured in the experiments. On the other hand, the irradiance reached on July 10th was not nearly as high as the one from July 25th, reaching almost 1500W/m^2, which can be attributed to lower solar irradiance on the testing day, which means that the performance in the summer is not guaranteed to reach the levels observed in the first test. Even though the lowest concentration for this design occurs at the equinoxes, the design proves to have good performances through this time of the year, reaching concentrated fluxes of 1400W/m^2. During this same period, we see minimum fluxes of 870W/m^2, which is similar to typical daily DNI peaks throughout the year. Demonstrating the usefulness of implementing this design over standalone absorber plates.

On average, the irradiance reaching the concentrator can be lower in the winter than the rest of the year, because of increased atmospheric losses. This means that the output flux for this season would tend to be lower, but because of the increased geometric concentration and inlet area tilt of the winter configuration, it is possible to obtain increased concentrated fluxes even when atmospheric losses are greater. Such is the case of the output flux measured in the winter experiment (November 23rd), where the day had plenty of clouds with varying levels of transparency, reducing the irradiance reaching the concentrator. Even with the lower irradiance for this day, and thanks to the increased concentration capabilities of the Winter Configuration, the output flux measured was in the same range as that of the experiments performed on the fall equinox and summer. This performance under cloudy conditions is specially promising, since it can improve energy harvesting for any solar application.

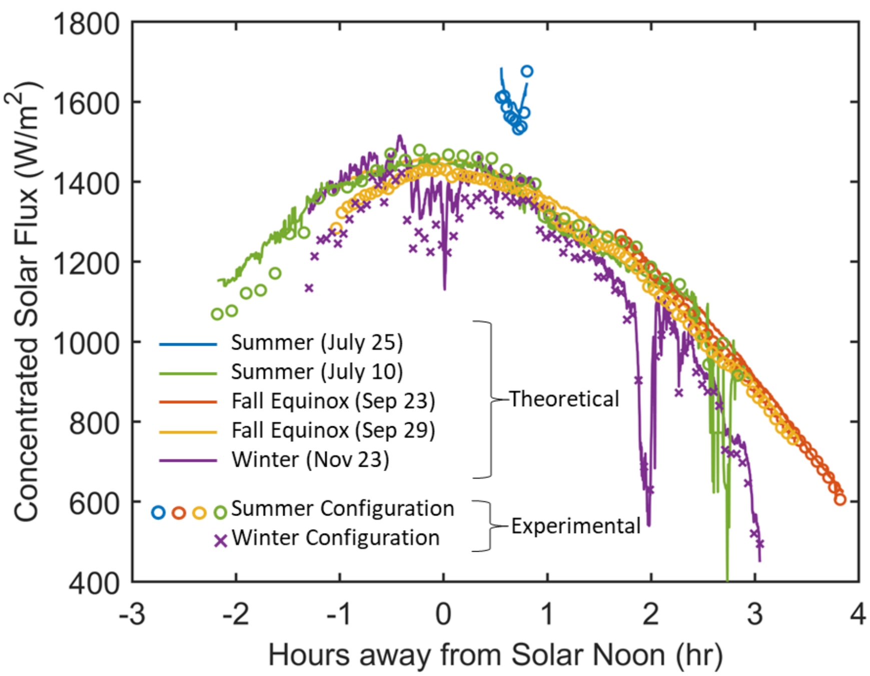

Figure 5.11 - Overview of Output Fluxes for all Flux Mapping Experiments

5.3.3. Outlet Flux Distribution

The present section presents a qualitative analysis of the flux distribution at the outlet of the concentrator, examining the spatial distribution patterns and characteristics of the emitted flux. By performing this analysis, it is possible to identify regions of high and low radiative flux and how they are distributed, these insights, together with the quantitative data, can be used to gauge the effectiveness of the design. Understanding how the flux is distributed at the outlet throughout the year can help identify its capabilities and limitations, and therefore inform design considerations when used for applications in Concentrated Photovoltaics (CPV) and Concentrates Solar Thermal (CST). By comparing the experimental to the simulated flux distribution, the quantitative analysis can also inform about the accuracy of the concentrator construction. This will help evaluate the performance of the parabolic profile construction method proposed in Chapter 3: and utilized on the experimental prototype. To perform this qualitative analysis, the images taken of the Lambertian target at the outlet were transformed into irradiance contour plots.

Through experimental tests and simulations, it has been found that the flux distribution exiting the concentrator is mostly anisotropic, with regions of high flux being common throughout the year, as seen in Figure 5.12. Note that the top of the plots is the edge of the outlet adjacent to the parabolic profile, or back parabola, and the front aligns with the front of the concentrator. This anisotropic behaviour is mostly characterized by a line of peak flux, surrounded on one side by a gradient reaching the top of the concentrator and a small gradient bellow the mentioned line. At the winter solstice (solar altitude of 22.9°) this line is located at the center of the outlet, but as the sun moves higher in the sky through the year, this high flux line moves closer to the top of the outlet. The area below this line is the region with the lowest flux, but as the solar altitude increases the flux in this area increases as a result. For solar altitudes approaching 63°, the high flux line reaches the top edge of the concentrator and most of the outlet is illuminated evenly. Past this point, the concentrator is illuminated evenly, but a low flux area appears at the top of the outlet, and it becomes wider as solar altitude increases.

Delving into the differences in outlet flux distribution between the design developed and its ACPC counterpart, Figure 5.12 serves as an example case for these differences. For this figure, the inlet and outlet area of the concentrators were kept the same, but since the ACPC has a slightly shorter outlet, there is a small gap at the top edge of the ACPC's outlet. The two designs result in very similar output distributions, with the θ_{out} version having a more focused high flux line. Similarly, the flux displayed by the ACPC is more diffuse, while having an average flux 1.5% higher than its θ_{out} counterpart.

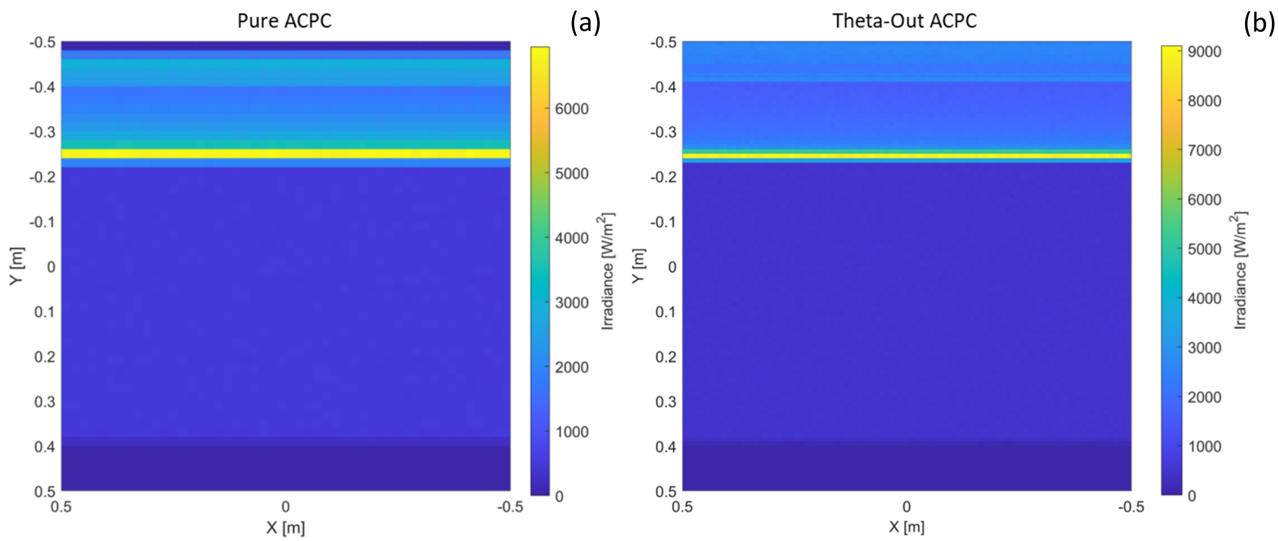

Figure 5.12 - Simulated outlet flux distribution for an ACPC and the θ_{out} design used for the prototype.

For an ideal infinitely long concentrator, the outlet flux distribution would be identical at any cross-section normal to the width of the concentrator. Ideal concentrators with finite width would show the same behaviour apart from its two ends, where the flux distribution would vary. Similarly, due to the presence of reflective sidewalls in the design, rays that would otherwise land along the width of the concentrator get reflected into a finite area, overlapping, and causing hotspots. An example of this is shown in Figure 5.13, where a caustic partially covers the width of the outlet, displaying double the radiative flux on the leftmost portion. The overlapping effect is more dramatic when comparing this to Figure 5.14a and b, where the caustic doesn't fold over itself. All of these features that cause anisotropy in the distribution must be considered when designing for applications such as CPV or CST, because they can affect performance. In the case of CPV when illuminating a Photovoltaic (PV) panel, the zones with caustics might produce more power, but will get hotter than the rest of the panel, risking low efficiency or even damage. To prevent this, a cooling system could be implemented as it is commonly used, but the anisotropic distribution should still be a considered in these situations.

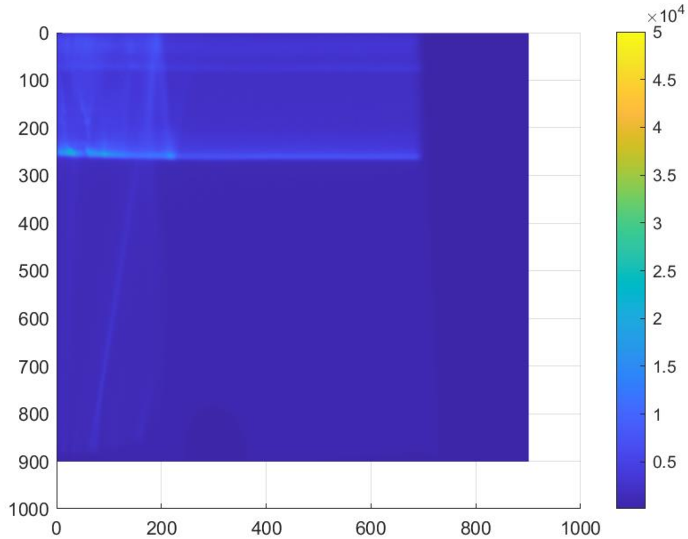

Figure 5.13 - Experimental outlet flux distribution displaying overlapping hotspots.

Starting with the second fall equinox experiment, which uses the summer configuration, some of the first observations to make include the presence of a high concentration region at the top third of the concentrator. A high concentration line at ~0.27 units from the top of the outlet (edge intersecting the parabolic profile) outlines the bottom of the previously mentioned region; this line presents the highest concentration of the whole profile. Even though Figure 5.14a was taken at solar noon, it presents a higher concentration caustic on the leftmost corner of the aforementioned line, signifying that the vector normal to the inlet was not aligned with the Sun vector at this time. This can be attributed to an inaccuracy when orientating the concentrator towards the south, or a mistake in the construction. On the other hand, Figure 5.14b, taken 2 minutes later, has a better distributed flux and presents no significant caustics outside of the high concentration line. This can signify that the previously mentioned issue is likely due to a misorientation when setting up the experiment. Both Figure 5.14a and b, show a slight curvature in the line, whereas the simulated distribution (Figure 5.14c) shows it as perfectly straight. This indicates that there was a slight curve across the width of the concentrator's reflectors, which can be seen in the prototype. That being said, the experimental results match well with the numerical ones, portraying the same high concentration profiles and gradients.

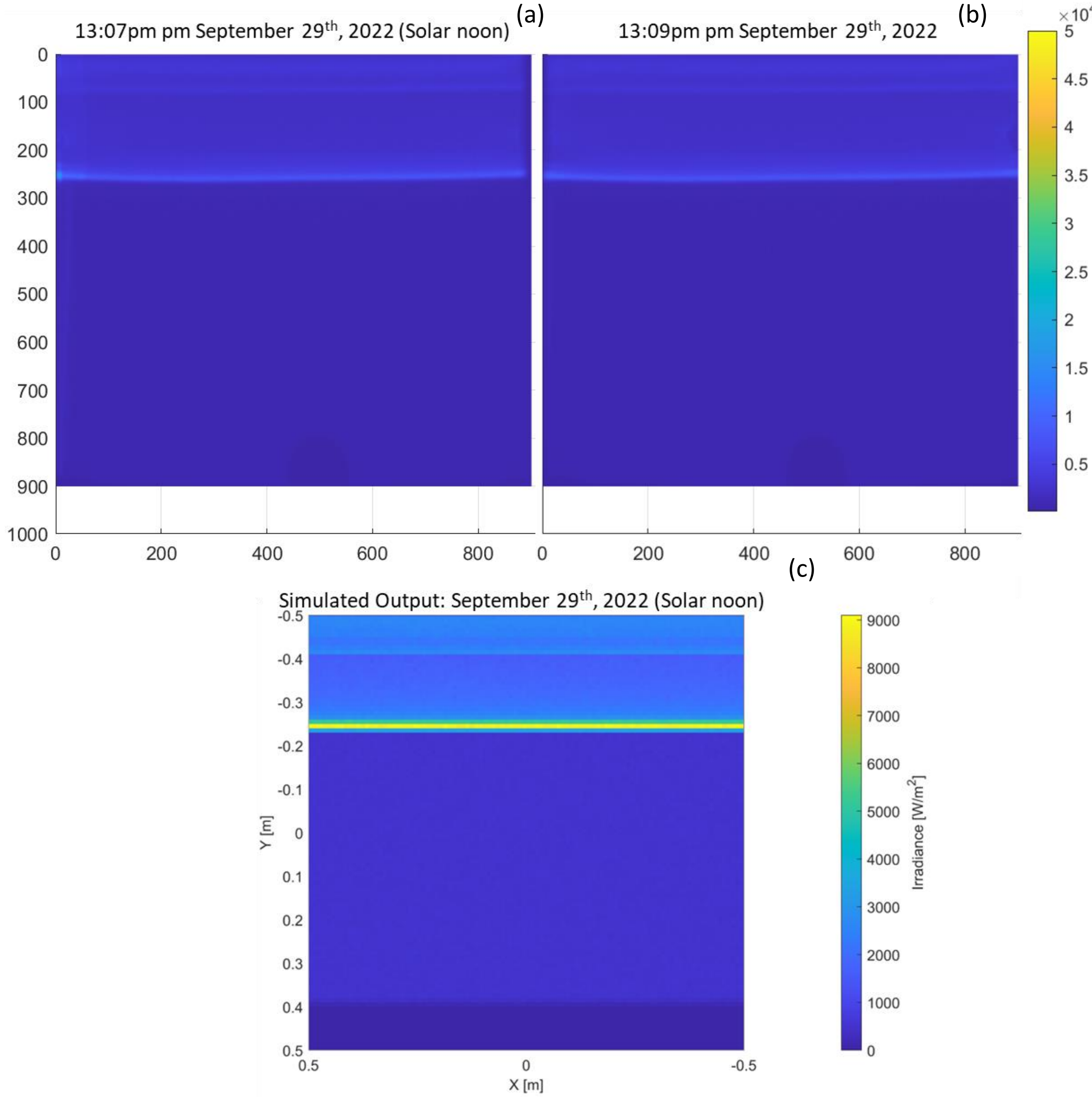

Figure 5.14 - Flux Distribution Plots at Solar Noon on the fall equinox Test performed on September 29th, 2022. Subfigure a) shows the experimental flux distribution at noon, b) shows the experimental flux distribution when the Sun vector was in line with the front of the concentrator, and c) shows the simulated (ideal) flux distribution for at noon of the test date.

Figure 5.15 displays the flux distribution profiles at solar noon, with Figure 5.15b showing the better distributed flux, similar to the previous figure. In this case the high concentration line appears to be straight, matching the simulated profile and indicating that the curvature seen in the fall equinox might have been caused by the front extension wall. That being said, the top edge of the high concentration region in the experimental plot isn't horizontal like its numerical counterpart. This was observed during the experiments, and through practical examination it was possible to determine that one of the side walls was tilted outwards, causing this inaccuracy. Similar to the previous case analyzed, the flux distribution plot taken at noon displays a caustic on the left most edge of the high concentration line, likely due to misalignment with the true south direction. Figure 5.15b, taken 2 minutes later, shows a more distributed flux profile. These plots confirm the spatial similarity between the numerical and experimental results presented above, which indicate a fairly precise replication of the true parabolic shape ideated for this concentrator.

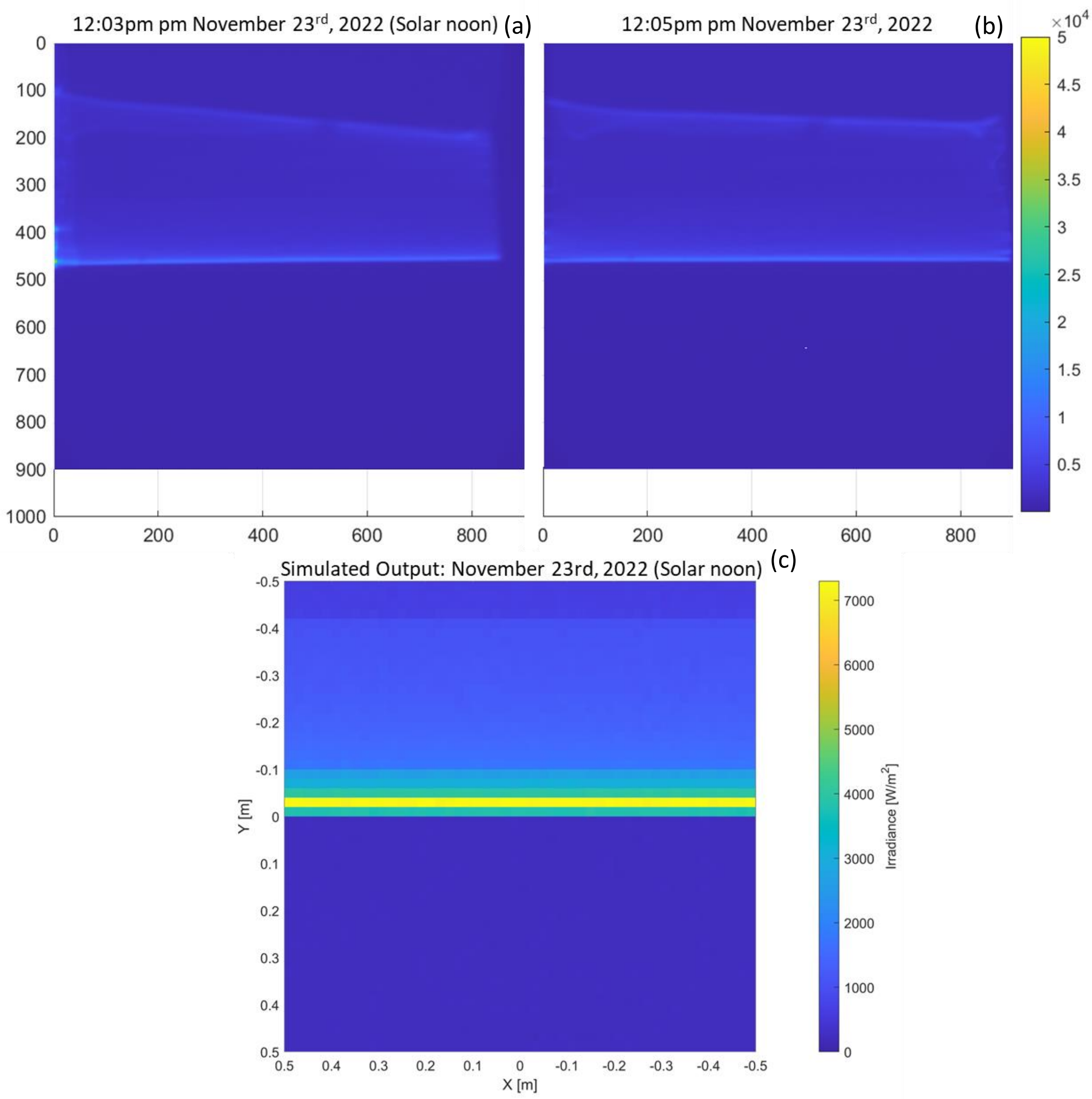

Figure 5.15 - Flux Distribution Plots at Solar Noon on the Winter Test performed on November 23rd, 2022. Subfigure a) shows the experimental flux distribution at noon, b) shows the experimental flux distribution when the Sun vector was in line with the front of the concentrator, and c) shows the simulated (ideal) flux distribution for at noon of the test date.

5.3.4. Optical Efficiency

The optical efficiency (η_{op}) plays a crucial role in the overall performance of a concentrator. As seen in previous sections η_{op} is composed of the acceptance efficiency and the reflectance of the surfaces to the power of the average number of reflections ($\rho^{\langle n_r \rangle}$). Considering this, it would be wise to maximize the first two and minimize the latter, with the objective of increasing optical efficiency. As seen in sections 3.2. and 5.1.1, acceptance efficiency is already the greatest it can be (η_{acc}=1), since the sun path through the year is always within the acceptance range of the concentrator. On the other hand, for a real surface the reflectance is rarely constant for all incidence angles and wavelengths, but to simplify calculations the reflectance of the surfaces in a concentrator are usually assumed to be constant. Lastly, as shown in section 5.1.2, $\langle n_r \rangle$ changes through the day and year as the sun moves through the sky and due to configuration changes in the concentrator. Therefore, rather than a constant value, in a day optical efficiency could be characterized as a range with a peak at solar noon and a minimum value at the end of daily operation, mainly due to $\langle n_r \rangle$. Nevertheless, it also exhibits variation through the year with overall higher optical efficiencies in the winter, as predicted in section 5.1.2.

Equation 5.4 elaborates on the definition of optical efficiency presented in Equation 2.29, by considering the experimentally measured power output and available power incident on the concentrator's inlet, to find the experimental optical efficiency. The incident power is described by the inlet area and the solar radiative flux incident on the concentrator's tilted inlet surface (see Equation 2.9). The diffuse and reflected radiation components are described based on the measured irradiance values and multiplied by the geometric factor ($R_{\beta,d}$ and $R_{\beta,r}$, respectively) seen in Equation 5.1, to obtain the diffuse and reflected radiation for the tilted surface. Using Equation 5.4, it was possible to obtain a generalized optical efficiency to describe the experimental performance of the concentrator, seen in Figure 5.16.

$$\eta_{op} = \frac{A_o \cdot H_o}{A_i \cdot H_\beta} = \frac{A_o \cdot H_o}{A_i\left(H_N * \cos\vartheta + H_d \cdot R_{\beta,d} + \rho_a \cdot H_G \cdot R_{\beta,r}\right)}$$

Equation 5.4 - Generalized experimental optical efficiency.

As expected, the resulting optical efficiency can be observed to have a peak near solar noon, but it is not symmetrical about solar noon, showing a slower decrease between 0 and 4 hours after noon. This is thought to be caused by inaccuracies in the construction of the concentrator, and anisotropy in both hemispherical reflectance of the concentrator surfaces and diffuse irradiance. The optical efficiency can be seen to surpass unity in several instances, which isn't physically possible. Rather, this is caused by sudden changes in direct irradiance (due to cloudy conditions), which become exacerbated by the difference in temporal resolution between the camera and thermopile sensors (see section 5.2.1). Contrary to the prediction made by theory, where the winter configuration portrayed the highest overall optical efficiency, the experimental results from the winter operation depict some of the lowest optical efficiencies. This is likely caused by more significant inaccuracies in the construction of the winter configuration, increased sensitivity to diffuse irradiance (for this configuration) and dust on the reflective surfaces. The inaccuracies in construction can also be seen in Figure 5.15, where the shape of the caustics differ from the ones predicted by the numerical analysis.

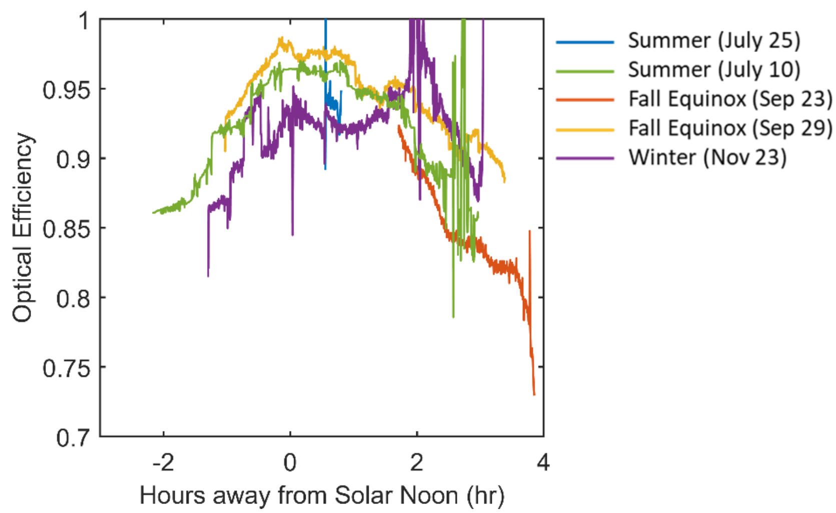

Figure 5.16 - Generalized experimental optical efficiency (η_{op})

Reflectance plays a crucial role in optical efficiency and is a factor that tends to change with time as a concentrator suffers damage on its reflective surfaces. Because of this it's difficult to quantify reflectance during the operation of the concentrator, but by using the experimental optical efficiency and Equation 2.31, it was possible to work backwards to estimate the experimental reflectance. The calculated reflectance was found to be far from constant, which is likely due to measurement noise, inaccuracies in the construction of the concentrator, and anisotropy in both hemispherical reflectance and diffuse irradiance. Because of this variance, an average reflectance was considered for each of the experiments, with results ranging between 0.94 and 0.97. This average reflectance was utilized to calculate a more precise concentrated solar flux estimate, which was used to plot the solid lines in Figure 5.11.

Chapter 6: Practical Implementation of the Seasonally Adaptive ACPC

One of the possible uses of stationary concentrators is to improve the performance of solar desalination devices. Solar desalination is a promising sustainable solution to the global issues of freshwater scarcity and accessibility. Solar desalination systems use solar radiation in the form of heat to evaporate contaminated or salt water, and later condensate it to be used as freshwater. There are a variety of systems that have been ideated to perform this purpose, which generally entails using a solar absorber to then transfers heat into the water, generating vapour. An interesting development made recently involves doing this without the need for direct contact between the absorber and the water, avoiding fouling of the absorber material, which is common in these types of systems. This fouling is caused by concentrated minerals and impurities that stay on the absorber surface as the water is evaporated. This innovative system called contactless solar evaporation structure, or CSES, was ideated by [32], and uses mainly radiation to generate water vapour, leaving behind the impurities at the water basin instead of the absorber.

Further studied by [49], CSES is composed of a water basin located under a solar absorber, with an air gap between the two. The body of the CSES is composed of an insulating foam, which has the purpose of reducing thermal losses and provide structure to the whole system. Ideally the absorber would be composed of a selective coating at the top to reduce emission losses while increasing absorption of solar radiation, and a coating with high IR emittance at the bottom of the absorber (side facing the water basin). All water vapour is generated via radiation, but as water evaporates the vapour continuous to heat up through radiation and convection, as it comes in contact with the absorber, becoming super heated. The generated steam then exits the device via an outlet to be cooled and used as freshwater. This is the system that the concentrator prototype was designed to be implemented with, as stated in Chapter 3: . The work highlighted in this chapter focuses on the implementation of the concentrator with a CSES device under real world conditions and provides insight into their performance.

6.1. Methodology

An experiment was ideated to investigate the performance of the solar desalination device (CSES) under real solar irradiance while using the concentrator prototype developed to increase the solar flux incident on the absorber. The experiment consisted of placing the CSES at the outlet of the concentrator while measuring the absorber, water, and steam temperatures, as well as the mass change and incoming radiation. The set up of the experiments can be seen in Figure 6.1. The temperatures were measured with type-K thermocouples and recorded every second. The location of the absorber thermocouple was the centre of the absorber plate, on its back side, taking the temperature of the emitter side. Similarly, the water thermocouple was placed at the center of the basin, shielded from the absorber plate's IR emissions. Lastly, the steam thermocouple was placed at the steam outlet, measuring the superheated steam released and ensuring no radiation from the absorber plate reached the thermocouple.

The mass change due to evaporation was measured via a mass balance, which recorded the mass of the whole CSES device every 3 seconds. To ensure an accurate water mass change measurement, the mass of the whole system was measured before and after the experiment. The GHI and DNI were measured using a pyranometer and pyrheliometer, respectively, recording data every 2 seconds. The concentrator prototype was placed above the CSES device, with its outlet centered on the CSES' absorber. The CSES device was fitted with a 3.8 cm reflective wall around its inlet, to redirect any radiation escaping. A vertical gap of 1 cm was left between the outlet of the concentrator and the top edge of the CSES, to prevent the concentrator from affecting the mass readings. Lastly, a Lambertian target was placed between the concentrator and CSES to verify the irradiance reaching the absorber using a procedure like the one described in section 4.2.1.

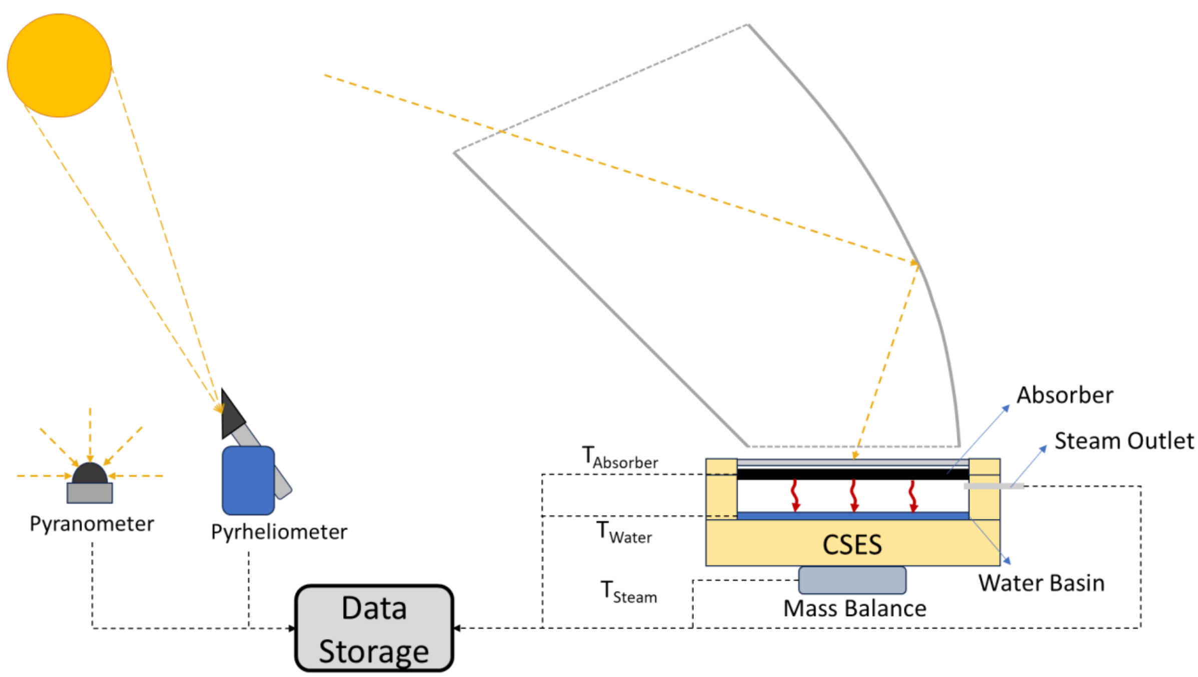

Figure 6.1 - Diagram of the solar desalination experimental setup

6.2. Results

Figure 6.2 shows the results of the solar desalination experiment performed on May 10th, 2023, on this day the maximum theoretical concentration reached 1.481×, which is 99.8% of the maximum summer concentration, set to occur at solar noon (1:13pm on that day). The test was started at 11:15 am, 2 hours before solar noon, and ended at 2:30 pm, after 3.25 hours of operation. Boiling was observed after 45 minutes of operation, for a total of 2 hours of continuous boiling (quasi-steady state operation). A total of 289 ml of water were poured into the CSES's basin, for a total CSES weight of 6444 g, before operation. After the experiment, the weight was measured again, which had reduced to 6322 grams, for a total evaporated mass of 122 ml during the 3.25 hours.

Figure 6.2a shows the behaviour of the temperature of the absorber, steam, and water during the extent of the experiment, as well as the mass change. There are 3 distinct dips in the temperature data from the absorber and steam, which are associated with a decrease in irradiance on the absorber when capturing the images of the Lambertian target to measure the concentrated flux at the outlet of the concentrator. Because of the thermal mass and heat capacity of water, this decrease in irradiance didn't have almost any effect on the water temperature. This, together with the water reaching a maximum quasi-steady temperature of 100°C, confirms that the water thermocouple was not directly impacted by the absorber plate's emissions, as, otherwise, the temperature reading would have decreased rapidly along with the other two temperature readings.

The mass measurements displayed in Figure 6.2a show a significant fluctuation due to wind hitting the experimental assembly. The data shown subtracts the weight of the dry CSES device from the mass measurements and removes non-numeric readings, caused by extreme fluctuations in weight (e.g., the range between 11:40 am and 11:50 am). Figure 6.2b displays the measured GHI and DNI and uses these, together with the model developed in the previous chapter, to plot an estimate of the concentrated solar flux reaching the outlet of the concentrator prototype. The estimate shown assumes a reflectance value of 1, and an albedo of 0.1. It's important to note that the concentrated solar flux reaching the absorber is not evenly distributed, which would create hotspots in different regions, as seen in section 5.3.3.

As seen in Figure 6.2a, the absorber temperature reached a maximum of 140°C at ~12:26 pm, 4 minutes before the water temperature reached 100°C. After this point, the temperature of the absorber decreased almost steadily, even though the concentrated flux reaching the absorber stayed relatively constant for the next hour. More specifically, the maximum concentrated flux was achieved 20 minutes after the absorber reached its maximum temperature. This apparent mismatch in the timeframes could have been caused by an increase in heat transfer because of the steam's contact with the absorber, adding convection to the CSES mode of heat transfer, which cools the absorber's surface. This is supported by the behaviour of the steam temperature, which reached its maximum around the same time as the maximum irradiance observed.

Even though the maximum absorber temperature was measured to be 140°C, due to the anisotropic distribution of radiation on the outlet of the concentrator and the thermal resistance of the absorber, there would be regions of the absorber with higher and lower temperatures than this. The overall relative temperature distribution at the top of the absorber could be described with the irradiance distribution plots obtained from the flux mapping experiment. On the other side of the absorber, the temperature distribution would be more uniform, with its uniformity being directly proportional to the thermal resistance of the absorber.

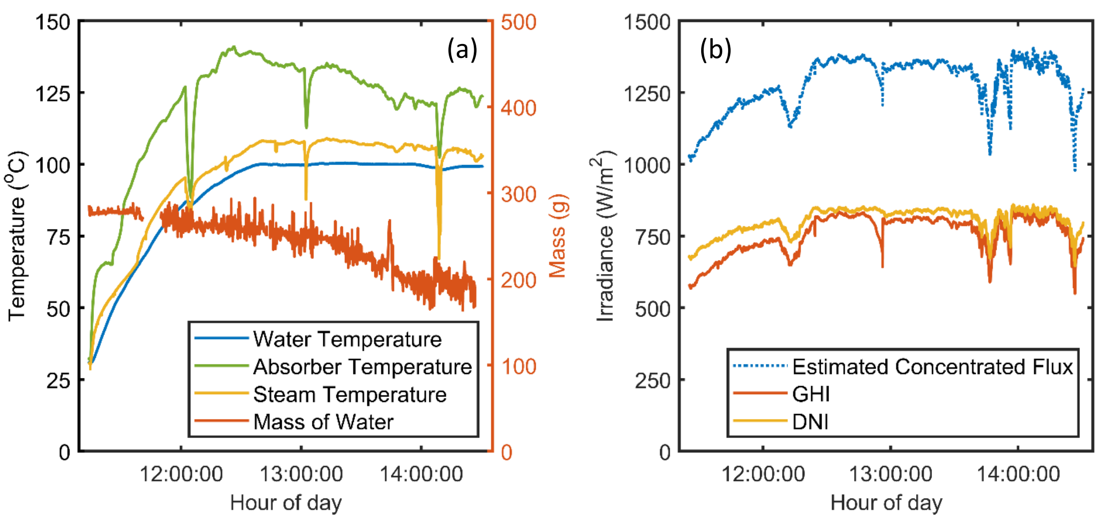

Figure 6.2 - Results of solar desalination experiment performed on May 10th, 2023.

The thermal efficiency of the CSES-concentrator system can be described in a simple manner, using the ratio of useful energy output to energy input. Where the energy the system requires to operate is in the form of solar radiation, which can be expressed by the global horizontal irradiance incident (H_G) on the inlet area of the concentrator over a time interval. Note that since the concentrator inlet is tilted, the H_G is changed for the global horizontal irradiance on a tilted surface (H_β). Similarly, since the objective of the system is to boil water, the formation of steam can be considered the final product of the system. Because of this, the useful energy output of the system can be described by the energy carried by mass of the water that is turned into steam. This can be calculated by the integral change in mass over the quasi-steady state operation, multiplied by the enthalpy of vaporization of water (h_{fg}). To obtain an overall efficiency over the quasi-steady state operation, the total irradiance incident on the concentrator is integrated with respect to time, resulting in the total energy incident on the system over this interval of time. This results in Equation 6.1, which, by only considering the quasi-steady state operation of the experiment and assuming that the pressure inside the CSES is 1 atm, results in a total thermal efficiency of 24%. It's useful to note that this efficiency considers the optical efficiency of the concentrator and thermal efficiency of the CSES itself, along with any losses associated with the CSES-concentrator implementation. On the other hand, this definition neglects reflected radiation and the effect that higher pressure inside the water basin has on the performance of the CSES.

$$\eta_{th} = \frac{\Delta m \cdot h_{fg}}{\int H_\beta dt \cdot A_i} = 24\%$$

Equation 6.1 - Thermal Efficiency of the CSES-concentrator system

The performance demonstrated by the combination of the Seasonally Adaptive ACPC and the CSES is promising for the field of solar desalination and stationary solar concentrators. This type of application is one of the few that takes advantage of the basic design of an ACPC without the need to redirect radiation onto a tubular receiver. Further studies should be performed where the mass of evaporated water is measured from the extracted steam, rather than the weight of the solar desalination device, while effectively guarding the mass balance from fluctuations due to external sources, to obtain more precise measurements of mass evaporation rate. Different absorber coatings can be implemented, in the search for a better balance between solar absorption and IR emission into the water. In a similar sense, the implementation of variations of the θ_{out} modification used here can help improve the absorptance of solar radiation, which needs to be considered in the design of both the concentrator and absorber. Likewise, the anisotropic irradiance and temperature distribution is a factor that must be considered when designing absorbers in future implementations, as thermal expansion due to large temperature differences can cause cracks in various materials. Depending on the location of implementation of the CSES system, a concentrator with higher concentration can be implemented, improving the performance shown here. The possibility of sealing the inlet of the concentrator with a highly transmissive material needs to be studied to determine if it can play a significant role in improving the performance of the CSES-concentrator system. Similarly, minimizing the gap between the absorber and concentrator outlet while ensuring thermal insulation would be ideal, as it has the possibility of improving thermal efficiency.

Chapter 7: Conclusions

This thesis has fulfilled its goal of describing and optimizing the performance of the Seasonally Adaptive ACPC to maximize concentration at high latitudes and describe its optical properties. The studies performed showed that this innovative stationary ACPC design has great potential to be used as a stationary concentrator for a variety of purposes because it pushes the barriers of conventional stationary collectors. This concentrator concept can obtain concentrations as high as 4× for a latitude of 60° (up to 20× at 78°), for both the summer and the winter, without the need for sun tracking. Additionally, through the design of an especially compact case of the Seasonally Adaptive ACPC, it was possible to achieve a maximum concentration of 2× for a concentrator that is tailored for latitudes higher than 31°.

The theoretical developments included in this work entail the thorough description of the three possible asymmetrical cases for a θ_{in}/ θ_{out} concentrator, their design procedures, and geometrical characteristics. Along with this, the methodology of the source – acceptance map matching was described for the design of ACPCs (objective 2), resulting in more tailored designs for various latitudes and hours of operation, and promising concentrations. The behaviour and performance possibilities of the Seasonally Adaptive ACPC were discussed (objective 1) and it was shown to mitigate the issues ACPC designs usually encounter when attempting to concentrate solar energy year-round. This is possible by the pseudo-tracking capabilities of the design which maximizes concentration for the whole year. Along with this, a theoretical model of the optical performance of the concentrator prototype (compact Seasonally Adaptive ACPC) was developed based on the acceptance efficiencies for direct, diffuse and reflected radiation (objective 1).

An innovative method for constructing compound parabolic profiles was developed, which allows for the reconfiguration of the parabolic profile. This is thought to be of special interest and benefit to researchers and product developers, since it allows for quickly iterating between CPC or ACPC designs, without the need for metal forming nor additional costs. This method is entails setting the position and orientation of two control points in the parabola to define the desired shape. A prototype of the compact case of the Seasonally Adaptive ACPC was developed and constructed using this method, which included a θ_{out} modification. Said prototype had a maximum concentration of 1.98× and allowed for studying the experimental performance of this design. This same geometry was used to develop numerical model of the Seasonally Adaptive ACPC and study its optical performance using Monte Carlo ray tracing (objective 3).

To explore the real-world performance of the concentrator and prototype design, an innovative experimental procedure for mapping the flux output was implemented. This technique consisted of imaging a Lambertian target located at the outlet of the concentrator using a grayscale camera while measuring the irradiance reaching the inlet of the concentrator. By calibrating the relative irradiance captured by the camera with images of the Lambertian target without concentration, it was possible to obtain an accurate map of the irradiance and calculate an average irradiance at the concentrator's outlet. This methodology allowed for performing the flux mapping experiments outdoor under real solar radiation. From these procedures, an impressive experimental concentration of ~1.78× was achieved in the winter months, which together with an analysis of the irradiance distribution at the outlet of the concentrator, confirmed the precision of the manufacturing method used for the parabolic profile (objective 4). These experimental results were also utilized to evaluate the theoretical model developed (objective 5).

A practical implementation of the Seasonally Adaptive ACPC was studied, which involved concentrating solar radiation onto a solar-driven desalination device (objective 6). This consisted of subjecting the concentrator to outdoor irradiance, while directing its output onto a contactless solar evaporation structure (CSES), while measuring the available irradiance, the temperatures of the device and the change in mass due to water evaporation. The concentrator was found to perform exceptionally well under the field conditions encountered, reaching quasi-steady state within 45 minutes, and allowing for the evaporation of >42% of the available water within 3.25 hours of operation.

The presence of cloudy conditions during the flux mapping experiments were seen to cause large amounts of variation and noise in the data. The major source of noise was found to be the difference in temporal resolution between the thermopile sensors and camera. With the camera capturing instantaneous changes in irradiance and the sensors having a response time between 7 and 18 seconds. The noise resulting from this issue made it impossible to distinguish the data from the noise. A possible future solution can entail implementing sensors with higher response times, or developing a method to obtain average images over a time frame that matches the response times of the sensors. On the other hand, measurements of GHI and DNI were found to have an uncertainty of up to 10.3%, mainly due to non-stability. The GHI measurements were also found to have up to 15% variance from secondary data, confirming the calculated uncertainty. The uncertainty from irradiance measurements was found to have an almost one-to-one effect on the calculation of concentrated output flux, with camera and calibration uncertainties attributing as little as 1% uncertainty. Surrounding building surfaces most likely cause anisotropy in the illumination, probably decreasing DHI and increasing reflected irradiance. Lastly, imperfections in the mirror surfaces could have caused lower reflectance and deviation from the ideal geometry, ultimately resulting in lower concentrations and irradiance at the outlet.

The flux mapping technique and method of manufacturing parabolic profiles introduced in this work can be an important tool for the study of solar concentrators. Future studies into the Seasonally Adaptive ACPC design can consider developing designs more tailored for specific latitudes, this would result in higher concentrations, at the cost of limiting its widespread use. Research should be mostly focused on studying the practical implementations of the design. An important next step in this direction is modifying the design to concentrate onto a tubular receiver (cylindrical concentrators), this improves the practicality of the design and can allow for even higher concentrations than the ones reported in this work. Designs developed following this concept can be used for solar heating and cooling systems, for residential and commercial use. It would be of interest to study the change in performance of the concentrator, and how the flat mirror extension works with the concept of a cylindrical concentrator. Finally, applications in CPV, radiative cooling and solar desalination can take advantage of the high concentrations achievable by the design presented.

Chapter 8: References

[1] E. F. Camacho and M. Berenguel, "Control of solar energy systems," *IFAC Proceedings Volumes (IFAC-PapersOnline)*, vol. 8, no. PART 1, pp. 848–855, 2012, doi: 10.3182/20120710-4-SG-2026.00181.

[2] "Energy Statistics Data Browser – Data Tools - IEA." https://www.iea.org/data-and-statistics/data-tools/energy-statistics-data-browser?country=WORLD&fuel=Energy%20supply&indicator=TESbySource (accessed Aug. 30, 2022).

[3] N. Karwa, L. Jiang, R. Winston, and G. Rosengarten, "Receiver shape optimization for maximizing medium temperature CPC collector efficiency," *Solar Energy*, vol. 122, pp. 529–546, Dec. 2015, doi: 10.1016/j.solener.2015.08.039.

[4] A. Rabl, "Comparison of solar concentrators," *Solar Energy*, vol. 18, no. 2, pp. 93–111, Jan. 1976, doi: 10.1016/0038-092X(76)90043-8.

[5] M. Tian, Y. Su, H. Zheng, G. Pei, G. Li, and S. Riffat, "A review on the recent research progress in the compound parabolic concentrator (CPC) for solar energy applications," *Renewable and Sustainable Energy Reviews*, vol. 82, pp. 1272–1296, Feb. 2018, doi: 10.1016/J.RSER.2017.09.050.

[6] P. Kurup and C. Turchi, "Initial Investigation into the Potential of CSP Industrial Process Heat for the Southwest United States," Nov. 2015. Accessed: Jul. 08, 2023. [Online]. Available: www.nrel.gov/publications.

[7] "Canada - Countries & Regions - IEA." https://www.iea.org/countries/canada (accessed Aug. 30, 2022).

[8] B. Schmitt, C. Lauterbach, S. J. Rad, and K. Vajen, "FEASIBILITY ASSESSMENT OF SOLAR PROCESS HEAT APPLICATIONS," 2011, Accessed: May 03, 2022. [Online]. Available: www.solar.uni-kassel.de,

[9] A. Hasan, J. Sarwar, and A. H. Shah, "Concentrated photovoltaic: A review of thermal aspects, challenges and opportunities," *Renewable and Sustainable Energy Reviews*, vol. 94, pp. 835–852, Oct. 2018, doi: 10.1016/J.RSER.2018.06.014.

[10] T. Osório, P. Horta, and M. Collares-Pereira, “Method for customized design of a quasi-stationary CPC-type solar collector to minimize the energy cost,” *Renew Energy*, vol. 133, pp. 1086–1098, Apr. 2019, doi: 10.1016/J.RENENE.2018.10.110.

[11] J. Chavez, *Introduction to Nonimaging Optics*. Boca Raton, FL: Taylor & Francis Group, 2008.

[12] D. R. Mills and J. E. Giutronich, “Symmetrical and asymmetrical ideal cylindrical radiation transformers and concentrators,” *JOSA, Vol. 69, Issue 2, pp. 325-328*, vol. 69, no. 2, pp. 325–328, Feb. 1979, doi: 10.1364/JOSA.69.000325.

[13] S. Nordlander, “Maximum concentration for ideal asymmetrical radiation concentrators,” 2005, doi: 10.1016/j.solener.2005.05.005.

[14] M. N. Ricketts, R. Winston, and J. Ferry, “Étendue and angular acceptance of the asymmetric compound parabolic concentrator,” *https://doi.org/10.1117/1.JPE.7.028003*, vol. 7, no. 2, p. 028003, Jun. 2017, doi: 10.1117/1.JPE.7.028003.

[15] J. Ferry and R. Winston, “Design method toward creating a three-dimensional asymmetric compound parabolic concentrator,” *https://doi.org/10.1117/1.JPE.10.037001*, vol. 10, no. 3, p. 037001, Sep. 2020, doi: 10.1117/1.JPE.10.037001.

[16] M. Souliotis, C. S. Garoufalis, A. P. Vouros, and A. Kavga, “Optical study of twin-tanked ICS solar heaters combined with asymmetrical CPC-type reflectors,” 2018, doi: 10.1002/er.4320.

[17] Y. Tripanagnostopoulos and M. Souliotis, “Integrated collector storage solar systems with asymmetric CPC reflectors,” *Renew Energy*, vol. 29, no. 2, pp. 223–248, Feb. 2004, doi: 10.1016/S0960-1481(03)00195-2.

[18] D. N. Korres and C. Tzivanidis, “A novel asymmetric compound parabolic collector under experimental and numerical investigation,” *Renew Energy*, vol. 199, 2022, doi: 10.1016/j.renene.2022.08.030.

[19] X. Zhang, S. Jiang, Z. Lin, Q. Gui, and F. Chen, “Model construction and performance analysis for asymmetric compound parabolic concentrator with circular absorber,” *Energy*, vol. 267, p. 126597, 2023, doi: 10.1016/j.energy.2022.126597.

[20] D. Cabral, “Development and performance comparison of a modified glazed CPC hybrid solar collector coupled with a bifacial PVT receiver,” 2022, doi: 10.1016/j.apenergy.2022.119653.

[21] W. N. A. W. Roshdan, H. Jarimi, A. H. A. Al-Waeli, O. Ramadan, and K. Sopian, “Performance enhancement of double pass photovoltaic/thermal solar collector using asymmetric compound parabolic concentrator (PV/T-ACPC) for façade application in different climates,” 2022, doi: 10.1016/j.csite.2022.101998.

[22] R. Muhumuza, A. Zacharopoulos, D. Mondol, M. Smyth, A. Pugsley, and J. Mcgee, “Simulation and experimental validation of solar radiation distribution on the absorber of a line-axis asymmetric compound parabolic concentrator,” 2020, doi: 10.1016/j.solener.2020.01.033.

[23] P. Nasseriyan *et al.*, “Numerical and Experimental Study of an Asymmetric CPC-PVT Solar Collector,” *Energies 2020, Vol. 13, Page 1669*, vol. 13, no. 7, p. 1669, Apr. 2020, doi: 10.3390/EN13071669.

[24] A. Rabl, “Optical and thermal properties of compound parabolic concentrators,” *Solar Energy*, vol. 18, no. 6, pp. 497–511, Jan. 1976, doi: 10.1016/0038-092X(76)90069-4.

[25] T. Ulavi, T. Hebrink, and J. H. Davidson, “Analysis of a Hybrid Solar Window for Building Integration,” *Energy Procedia*, vol. 57, pp. 1941–1950, 2014, doi: 10.1016/j.egypro.2014.10.058.

[26] A. Zacharopoulos, P. C. Eames, D. McLARNON, and B. Norton, “Linear Dielectric Non-Imaging Concentrating Covers For PV Integrated Building Facades,” vol. 68, no. 5, pp. 439–452, 2000, Accessed: Jul. 08, 2023. [Online]. Available: www.elsevier.com/locate/solener

[27] T. Cooper, G. Ambrosetti, A. Pedretti, and A. Steinfeld, “Theory and design of line-to-point focus solar concentrators with tracking secondary optics,” *Applied Optics, Vol. 52, Issue 35, pp. 8586-8616*, vol. 52, no. 35, pp. 8586–8616, Dec. 2013, doi: 10.1364/AO.52.008586.

[28] R. Winston and W. Zhang, “Pushing concentration of stationary solar concentrators to the limit,” *Optics Express, Vol. 18, Issue S1, pp. A64-A72*, vol. 18, no. 101, pp. A64–A72, Apr. 2010, doi: 10.1364/OE.18.000A64.

[29] T. Cooper, “Design of Non-tracking Solar Concentrators via Source/Acceptance Map Matching,” in *OSA Advanved Photonics Congress*, 2021.

[30] D. N. Korres and C. Tzivanidis, “Numerical investigation and optimization of an experimentally analyzed solar CPC,” *Energy*, vol. 172, pp. 57–67, Apr. 2019, doi: 10.1016/J.ENERGY.2019.01.119.

[31] T. Cooper, F. Dähler, G. Ambrosetti, A. Pedretti, and A. Steinfeld, “Performance of compound parabolic concentrators with polygonal apertures,” *Solar Energy*, vol. 95, pp. 308–318, Sep. 2013, doi: 10.1016/J.SOLENER.2013.06.023.

[32] T. A. Cooper *et al.*, “Contactless steam generation and superheating under one sun illumination,” *Nature Communications 2018 9:1*, vol. 9, no. 1, pp. 1–10, Dec. 2018, doi: 10.1038/s41467-018-07494-2.

[33] H. K. Seidlitz, S. Thiel, A. Krins, and H. Mayer, “Solar radiation at the Earth’s surface,” *Comprehensive Series in Photosciences*, vol. 3, no. C, pp. 705–738, Jan. 2001, doi: 10.1016/S1568-461X(01)80071-5.

[34] A. B. Sproul, “Derivation of the solar geometric relationships using vector analysis,” *Renew Energy*, vol. 32, no. 7, pp. 1187–1205, Jun. 2007, doi: 10.1016/j.renene.2006.05.001.

[35] N. Janotte, S. Wilbert, F. Sallaberry, M. Schroedter-Homscheidt, and L. Ramirez, “Principles of CSP performance assessment,” *The Performance of Concentrated Solar Power (CSP) Systems: Analysis, Measurement and Assessment*, pp. 31–64, Jan. 2017, doi: 10.1016/B978-0-08-100447-0.00002-X.

[36] E. A. Carter, “RADIATION MEASUREMENTS,” pp. 7–22, Jan. 1981, doi: 10.1016/B978-0-08-025388-6.50012-X.

[37] S. A. M. Maleki, H. Hizam, and C. Gomes, “Estimation of Hourly, Daily and Monthly Global Solar Radiation on Inclined Surfaces: Models Re-Visited,” *Energies 2017, Vol. 10, Page 134*, vol. 10, no. 1, p. 134, Jan. 2017, doi: 10.3390/EN10010134.

[38] M. Danandeh and S. G. Mousavi, “Solar irradiance estimation models and optimum tilt angle approaches: A comparative study,” 2018, doi: 10.1016/j.rser.2018.05.004.

[39] T. A. Cooper, “High-concentration solar trough collectors and their application to concentrating photovoltaics,” ETH Zurich, Zurich, 2014. doi: 10.3929/ethz-a-010216611.

[40] R. Winston, J. C. Miñano, and P. Benítez, *Nonimaging Optics*, 1st ed. Elsevier Academic Press, 2005.

[41] M. J. Carvalho, M. Collares-Pereira, J. M. Gordon, and A. Rabl, “Truncation of CPC solar collectors and its effect on energy collection,” *Solar Energy*, vol. 35, no. 5, pp. 393–399, 1985, doi: 10.1016/0038-092X(85)90127-6.

[42] A. Rabl and R. Winston, “Ideal concentrators for finite sources and restricted exit angles,” *Applied Optics, Vol. 15, Issue 11, pp. 2880-2883*, vol. 15, no. 11, pp. 2880–2883, Nov. 1976, doi: 10.1364/AO.15.002880.

[43] A. Rabl, “Radiation transfer through specular passages—a simple approximation,” *Int J Heat Mass Transf*, vol. 20, no. 4, pp. 323–330, Apr. 1977, doi: 10.1016/0017-9310(77)90153-3.

[44] Y. Yu, N. Liu, G. Li, and R. Tang, “Performance comparison of CPCs with and without exit angle restriction for concentrating radiation on solar cells,” *Appl Energy*, vol. 155, pp. 284–293, Oct. 2015, doi: 10.1016/J.APENERGY.2015.06.012.

[45] P. Planas Alzaman, “Accuracy of Monte Carlo Ray-Tracing Thermal Radiation Calculations: A Practical Discussion,” in *European Symposium on Space Environmental Control Systems*, Noordwijk, The Netherlands, 1997, pp. 579–591.

[46] A. K. Roy Choudhury, *Principles of colour and appearance measurement*. Woodhead, 2014. doi: 10.1533/9780857099242.

[47] M. F. Modest, *Radiative Heat Transfer*. Elsevier, 2013. [Online]. Available: https://app.knovel.com/hotlink/khtml/id:kt00BIVP42/radiative-heat-transfer/radiative-properties

[48] J. Mahal, P. Good, G. Ambrosetti, and T. A. Cooper, “Contactless thermal mapping of high-temperature solar receivers via narrow-band near-infrared thermography,” *Solar Energy*, vol. 246, pp. 331–342, Nov. 2022, doi: 10.1016/J.SOLENER.2022.10.004.

[49] T. Islam, “High-efficiency solar desalination and superheated steam generation using contactless infrared heating,” York University, Toronto, 2022.